Accurate continuum theories for condensed matter systems

by Johannes Lischner

ACCURATE CONTINUUM THEORIES FOR CONDENSED MATTER SYSTEMS

A Dissertation

Presented to the Faculty of the Graduate School

of Cornell University

in Partial Fulfillment of the Requirements for the Degree of

Doctor of Philosophy

by

Johannes Lischner

August 2010

ACCURATE CONTINUUM THEORIES FOR CONDENSED MATTER SYSTEMS

Johannes Lischner, Ph.D.

Cornell University 2010

This dissertation presents the construction and application of novel accurate continuum theories to various many-body problems in condensed matter systems.

We begin with the construction of a new "classical" density-functional theory for general molecular liquids which is based on an exact evaluation of the free energy of a noninteracting molecular gas. By adding terms which capture intermolecular interactions, we arrive at a theory which reproduces both the linear and nonlinear dielectric response of the liquid, the experimental correlation functions of the uniform phase and various thermodynamic properties, such as the surface tension or liquid-vapor coexistence.

We then apply our "classical" density-functional theory to the liquid of greatest importance, water. We introduce new computational techniques for efficient evaluation of the free energy of noninteracting water molecules and apply the resulting theory to the study of liquid water at solid surfaces. In strong electric fields, we observe dielectric saturation in good agreement with previously published molecular dynamics calculations.

Next, we introduce a new, *joint* time-dependent density-functional theory for the description of dissolved electronic systems in time-dependent external potentials. Starting from the exact action functional for electrons and nuclei of both the solute and the solvent, we systematically eliminate solvent degrees of freedom and finally arrive at a coarse-grained action functional which retains the detailed

ab initio description only for the solute electrons while treating the solvent with an approximate continuum theory. We apply this theory to study electronic excitations of formaldehyde in aqueous solution and find good agreement between our predictions and experimental findings.

Finally, we examine phonon-phonon interactions in carbon nanotubes using an elastic continuum theory with elastic constants obtained from *ab initio* calculations. The resulting theory allows us to predict intrinsic quality factors of the fundamental flexural mode for tubes of different lengths and radii, but also for different temperatures and strains. We find that the intrinsic quality factor at room temperature is about one order of magnitude higher than current experimental findings, indicating that there remains room for improvement in current devices. We also explore the possibility of carbon nanotube mass sensors with single yoctogram precision.

BIOGRAPHICAL SKETCH

The author was born in Stuttgart, Germany in 1981. After attending the Ernst-Sigle Gymnasium in Kornwestheim, Germany for nine years and a year of military service, he began studying physics at the Ruprecht-Karls Universität in Heidelberg, Germany. After three years in Heidelberg, he came to Cornell University on a one-year exchange fellowship in 2005. He joined the group of Professor Tomás Arias and decided to stay at Cornell University to obtain a PhD degree.

To Anna-Sophia

ACKNOWLEDGEMENTS

I thank my advisor Professor Tomás Arias for his guidance during the past five years. I greatly enjoyed working with him — not only because of his awe-inspiring intellectual capacities, but also because of his sense of humor and his interest in topics other than physics.

I also thank Professor Paul McEuen and Professor Neil Ashcroft for serving on my committee and for interesting discussions about physics. I had the priviledge of collaborating with Professor Garnet Chan and thank him for introducing me to the secrets of quantum chemistry.

I thank Dr. Peter Drehmann who was my physics teacher in high school. His passionate love for physics convinced me to become a physicist myself.

During the past five years I was lucky to have many great office mates. I thank JeeHye Lee, Kendra Letchworth-Weaver, Peijun Zhou, Daniel Freedman, Sahak Petrosyan, David Roundy, Ivan Daykov and Ravishankar Sundararaman for many interesting discussions about a wide range of topics and for helping me whenever the computers did not do what I wanted.

I was fortunate to have a group of fantastic friends in Ithaca. In particular, Tchefor Ndukum, Praveen Gowtham and Sumiran Pujari have become more brothers than friends to me. I also enjoyed spending time with Meisha Morelli, Sudeep Mandal, Duane Loh, Pantelis Tziveloglou, Joanna and Vlad Pribiag and Darryl Ngai. I also thank my friends back in Germany, in particular, Alex Krauch, Daniel Cremers and Sandra Seibert.

Of course, I owe much gratitude to my mother Benedicta Günther and my father Hans-Jörg Lischner who always supported me, but also to their spouses Harnet Mana and Uli Günther who have become part of my family. I also thank my sister Ulla and my grandmothers, Oma Emmy and Oma Käthe.

Finally, I thank Anna-Sophia Stamm, the love of my life.

TABLE OF CONTENTS

LIST OF FIGURES

LIST OF TABLES

CHAPTER 1

INTRODUCTION

The desire to understand the world around us is rooted deeply in the human nature. During the past one hundred years, the mathematical theory of condensed matter physics has provided explanations for many puzzling observations, ranging from the fact that certain materials conduct electric currents better than others to strange phenomena occurring in two-dimensional electron gases in strong magnetic fields at very low temperatures. However, apart from satisfying our craving for insight and exposing the vast complexity of each grain of sand, the theory of condensed matter systems has made possible many technological innovations enabling the human race not only to understand but also *control* its environment: for example, solar cells enabled us to exploit the power of the sun and the computer, based on the invention of the transistor, has changed virtually every aspect of human life.

Due to the broad range of time and length scales occurring in condensed matter systems, numerous mathematical approaches have been developed to describe these systems theoretically. Of course, the fundamental constituents of all condensed matter systems, atoms and molecules, obey the laws of quantum statistical mechanics, but exact solutions of the Schroedinger equation exist only for the simplest physical systems, such as the hydrogen atom. To gain insight into larger and more complicated systems two approaches have been developed: the analytical approach replaces the original system of interest by a much simpler model system, which shares certain physical properties with the original system and can be analyzed analytically. Contrary to the analytical approach, the *ab initio* approach aims at describing the original system of interest in as much detail as possible.

Both approaches have enjoyed great success over the past decades. The understanding of effective theories from Wilson's renormalization group approach [1] and the emergence of the notion of universality [2] provided a firm foundation for the analytical approach. On the other hand, the success of electron density-functional theory [3, 4] and the great increase of computer power allowed for the application of the *ab initio* approach to a great variety of systems, ranging from localized systems, such as molecules or clusters, to extended systems, such as periodic solids [5].

However, despite the great increase in computer power and the development of efficient algorithms, the *ab initio* approach can only be applied to systems containing less than a few hundred atoms. To describe larger systems theoretically, more coarse grained approaches are necessary. In these approaches, one typically eliminates the electronic degrees of freedom using the Born-Oppenheimer approximation [6], for example by fitting "classical" interatomic potentials to *ab initio* calculations [7], and employs a theoretical description in terms of the nuclear degrees of freedom only. These coarse grained theories are often atomistic in that they deal with a set of nuclear coordinates, such as in the molecular dynamics or in the Monte Carlo method [8]. However, calculating finite temperature properties is often computationally challenging even within coarse grained atomistic theories. Also, the fitting of selected physical quantities to *ab initio* calculations typically does not guarantee the ability of the coarse grained approach to reliably describe a broad range of physical properties of the system under consideration.

In this thesis, we explore an alternative approach: we develop novel *continuum theories* which reliably describe large condensed matter systems in a computationally tractable way. In the succeeding chapters, we demonstrate the applicability

of the continuum approach to a wide variety of systems and circumstances: we apply the approach to both liquids and crystalline structures, we study confined three-dimensional systems and quasi one-dimensional systems, equilibrium states and non-equilibrium states and both linear and nonlinear response properties.

1.1 The meaning of *ab initio* in this thesis

So as not to confuse the reader, we comment here that the term "*ab initio*" has slightly different meanings to different communities. Whenever the term "*ab initio*" appears in this thesis, we mean it in the following sense. From the Latin, "*ab initio*" literally means "from the beginning". In physics, this is taken in sense of "from first principles," meaning that one begins from the known fundamental laws and constants and otherwise employs no empirical or experimental input, other than the knowledge of such laws and the values of such constants. In the community to which this thesis is primarily directly, the term does not mean "without approximation". Indeed, no numerical physics calculation is ever free of approximations, whether it be the finite precision of computations, the use of the Born-Oppheimer approximation, truncation of a configuration-interaction calculation to a finite number of Slater determinants in otherwise exact quantum chemistry methods, the truncation of the expansion of continuous functions to a finite basis or representation of continuous functions on a grid of finite spacing, or the use of the local density approximation in density functional theory. It is true that the latter of these approximations is not systematically improveable in the senses in which are the former. As a result, some communities do not view density-functional theory calculations as "*ab initio*," whereas others do. Other communities adopt the point of view that the meaning of "*ab initio*" is simply "from the beginning" or "from first principles," which does not imply lack of ap-

proximation. Throughout this thesis, we adopt this later point of view and so regard density-functional theory calculations carried out within the local-density approximation as "*ab initio*".

1.2 Overview

1.2.1 Classical density-functional theory of liquids

In the first two chapters, we introduce a new "classical" density-functional theory for molecular liquids. Molecular liquids, above all water, play an important role as solvents in biophysics or electro-chemistry. However, contrary to the theory of solids or gases the theory of liquids contains no small parameter making perturbative approaches inapplicable. Most insight into the structure of liquids was gained by computer simulations using the molecular dynamics or Monte Carlo methods [9]. As described above, calculating finite temperature properties within these methods is computationally demanding.

In contrast, "classical" density-functional theory [10] obtained by starting out with the full free energy of the liquid in terms of both nuclear and electronic degrees of freedom and subsequently "integrating out" the electrons grants us direct access to finite temperature properties via a simple minimization of the coarse grained free energy functional. The key problem of "classical" density-functional theory is finding reliable approximations for this functional.

In the case of mono-atomic liquids considerable success has been achieved by starting from the analytically known free energy of the ideal gas and subsequently

adding terms that describe hard sphere repulsion and attractive interactions, such as the van der Waals interactions [11–13]. Unfortunately, a hard sphere reference system is a poor starting point for the description of water because of the strong anisotropic short-range interactions arising from the molecular structure, including effects such as hydrogen bonding. We therefore develop a "classical" density-functional theory, which takes full account of the molecular structure *from the outset* by starting from the free energy of a noninteracting *molecular gas* and subsequently adding terms which capture inter-molecular interactions, such as hard sphere repulsion or electrostatic interactions due to the dipole moment of the water molecule. The result is the first "classical" density-functional theory for water which is capable of capturing the microscopic linear and *nonlinear* dielectric response, but also reproduces the experimental site-site correlation functions, the surface tension, the bulk modulus of the liquid and the variation of this modulus with pressure, the density of the liquid and the vapor phase and liquid-vapor coexistence.

1.2.2 Joint time-dependent density-functional theory

In the fourth chapter of this thesis, we introduce a joint time-dependent density-functional theory, which describes the evolution of an electronic system in contact with a complex environment under the influence of a time-dependent external potential. A typical example of such a system is a molecule dissolved in a liquid exposed to an electromagnetic wave. It is well-known that the presence of the liquid environment effects changes of the excited states of the molecule [14, 15]. In particular, solvato-chromic shifts, shifts of the excitation energies with respect to their gas phase values, are experimentally measurable for many solute/solvent

combinations [15].

Theoretical modelling of such a solute/solvent system is challenging because the solvent comprises a large number of molecules. We therefore develop a theoretical approach which employs the highly accurate, but computationally demanding *ab initio* description only for the solute and utilizes a coarse grained continuum theory for the solvent. The result is the first rigorous framework for carrying out time-dependent density-functional theory response calculations without the need for explicit treatment of the environment.

1.2.3 Elastic continuum theory of carbon nanotubes

In the last chapter of this thesis, we employ an elastic continuum theory to study phonon-phonon interactions in carbon nanotubes. In contrast to the aforementioned continuum theories for liquids, where densities or effective potentials are used as degrees of freedoms, we now follow the standard elasticity theory of solids [16] and attempt to construct a free energy functional in terms of the strain tensor, which in solids is generally a small quantity due to the strong interatomic bonding.

However, because of the reduced dimensionality of nanostructures, such as graphene sheets or carbon nanotubes, certain elastic deformations, such as the bending of a flat nanoribbon into a tubular shape, are not captured by the strain tensor. We therefore introduce an additional degree of freedom, the curvature tensor, which allows us to describe such bending deformations and study interactions between acoustic and optical phonons. This approach allows us to provide the first correct treatment of the temperature, strain, radius and length dependence of the intrinsic quality factors of carbon nanotube oscillators.

1.3 Theoretical methods

The chapters of this thesis are meant to be relatively self-contained. In each, we generalize upon and build outward from well established general methods, "classical" density-functional theory [10], time-dependent density-functional theory [17, 18], and the general theory of elasticity [16]. As, particularly, the former two of these may not be familiar to all readers, we here give a very brief review of the underlying fundamentals. As the theory of elasticity has been very well established for quite some time now, for background on this material we refer the reader to the beautiful and simple text by Landau and Lifshitz[16].

1.3.1 Classical density-functional theory

The fundamental theorem of density-functional theory was derived by Hohenberg and Kohn [3] for ground state fermion systems and subsequently generalized to finite temperatures by Mermin [19]. Fundamentally, a liquid consists of electrons and nuclei of various species, which are described by the Hamiltonian

$$\hat{H} = \hat{T}_{el} + \hat{T}_{nuc} + \sum_{i<j} \frac{1}{|\hat{\boldsymbol{r}}_i - \hat{\boldsymbol{r}}_j|} + \sum_{I<J} \frac{Z_I Z_J}{|\hat{\boldsymbol{R}}_I - \hat{\boldsymbol{R}}_J|} - \sum_{i,J} \frac{Z_J}{|\hat{\boldsymbol{r}}_i - \hat{\boldsymbol{R}}_J|}, \tag{1.1}$$

where i, j range over all electrons in the system and I, J range over all nuclei, $\hat{T}_{el} = \sum_i -\frac{1}{2}{\nabla_i}^2$ and $\hat{T}_{nuc} = \sum_I -\frac{1}{2M_I}{\nabla_I}^2$ denote the kinetic energy operators of electrons and nuclei, respectively, and Z_I, M_I denote the respective atomic number and mass of the I-th nucleus. Also, $\hat{\boldsymbol{r}}_i$ denotes the position operator of the i-th electrons and $\hat{\boldsymbol{R}}_J$ denotes the analogous quantity for the J-th nucleus. Finally, we work here in atomic units where the electron mass, Planck's constant, and the fundamental charge all have values of unity. The resulting system of units

has as its measure of distance 1 bohr≈0.5291 angstrom and its measure of energy 1 hartree≈27.21 eV.

For such a multicomponent system at finite temperature, Mermin's theorem states that the equilibrium densities of electrons [denoted $n(\boldsymbol{r})$] and nuclei [denoted $N(\boldsymbol{r})$] minimize the grand free energy functional

$$\Omega[n,N] = F[n,N] + \int_W d\boldsymbol{r} n(\boldsymbol{r}) v(\boldsymbol{r}) + \int_W d\boldsymbol{r} N(\boldsymbol{r}) V(\boldsymbol{r}), \tag{1.2}$$

where $v(\boldsymbol{r})$ and $V(\boldsymbol{r})$ denote the external potentials acting on electrons and nuclei, respectively. Also, W denotes an open value as required when working in the grand canonical ensemble. The universal functional $F[n,N]$, which is independent of the external potentials, is defined via the Levy-Lieb search procedure [20, 21] according to

$$F[n,N] = \min_{\hat{\rho}\to[n(\boldsymbol{r}),N(\boldsymbol{r})]} \mathrm{Tr}\hat{\rho}\left(\hat{H} - \mu_{\mathrm{el}}\hat{N}_{\mathrm{el}} - \mu_{\mathrm{nuc}}\hat{N}_{\mathrm{nuc}} + k_B T \log\hat{\rho}\right), \tag{1.3}$$

where $\hat{\rho}$ denotes the full quantum-mechanical density matrix for electrons and nuclei, $\hat{H}$ is the Hamiltonian *without* the contribution from the external potentials and $k_B T$ denotes the thermal energy. Also, μ_{el} and $\hat{N}_{\mathrm{el}}$ denote the chemical potential and particle number operator of the electrons, while μ_{nuc} and $\hat{N}_{\mathrm{nuc}}$ denote the analogous quantities for the nuclei.

We note that the proper definition of the various thermodynamic functions, such as the species-dependent chemical potentials, requires great care. For neutral Coulomb systems, Lebowitz and Lieb [22, 23] showed that the thermodynamic limit exists in the grand canonical ensemble and that only *neutral* fluctations contribute to the grand free energy in this limit. The constraint of charge neutrality, however, imposes an important relation between the species-specific chemical potentials and one must be careful in actual calculations involving charged species to always

maintain charge neutrality in the thermodynamic limit. Finally, we note that in the thermodynamic limit the electron chemical potential is given by $\mu_{\rm el} = (\partial f/\partial n)_T$, where f denotes the Helmholtz free energy per unit volume. Similarly, we find $\mu_{\rm nuc} = (\partial f/\partial N)_T$.

A "classical" grand free energy functional in terms of the nuclear density only can then be obtained by minimizing $\Omega[n, N]$ with respect to the electron density for fixed nuclear densities. The resulting "classical" free energy functional is given by

$$\Omega_{cl}[N] = F_{cl}[N] + \int_W d\boldsymbol{r} N(\boldsymbol{r}) V(\boldsymbol{r}), \tag{1.4}$$

with $F_{cl}[N] = \min_{n(\boldsymbol{r})}\{F[n, N] + \int_W d\boldsymbol{r} n(\boldsymbol{r}) v(\boldsymbol{r})\}$.

Thus, one may obtain the full free energy of the system in any external potential, *without the need for any explicit thermodynamic sampling*, simply by minimizing $\Omega_{cl}[N]$ over all possible densities which obey $N(\boldsymbol{r}) \leq 0$ and integrate to the total number of particles. While it is clear that such a universal (i.e., V-independent) functional $\Omega_{cl}[N]$ exists for each fluid, the question remains as to what the functional actually is. Generally, this is an unsolved problem, and so one seeks useful, accurate approximations to $\Omega_{cl}[N]$. The work in this thesis focuses on developing such a functional for small polar molecules in general, and water in particular.

1.3.2 Time-dependent density-functional theory

Time-dependent density-functional theory describes condensed matter systems which are exposed to time-dependent external potentials [17, 18]. Contrary to the equilibrium case described above, where the system under consideration is

described by a free energy functional, in the time-dependent case the action functional plays the central role [17, 24]. However, the proper definition of an action functional, which meets the requirement of causality, is challenging and requires techniques of non-equilibrium Green's function theory. In the following, we take the approach of van Leeuwen [24] and define the relevant physical quantities, such as densities or external potentials, on the Keldysh contour, which goes from 0 to ∞ and back on the real time axis and then from zero to $-i\beta$ on the imaginary time axis.

We now briefly review the time-dependent density-functional theory of a system of electrons, following the standard development which may be found in the literature[24] but taking care to maintain charge neutrality in the thermodynamic limit. The treatment describes the electrons with a Hamiltonian

$$\hat{H} = \hat{T} + \hat{U} + \int_W d\boldsymbol{r}\hat{n}(\boldsymbol{r})u(\boldsymbol{r},\tau) + U_E.$$

In this Hamiltonian, $u(\boldsymbol{r},\tau)$ is the external potential at the Keldysh time τ, and $\hat{T}$ denotes the kinetic energy operator. To ensure charge neutrality in the thermodynamic limit for the various terms we shall separate later, $\hat{U}$ represents the electron-electron interactions in the presence of a uniform positive background of density n_0 chosen to guarantee charge neutrality, and the potential $u(\boldsymbol{r},\tau)$ in the third term is understood to contain the electrostatic potential from the nuclei in a negative neutralizing charge background of density $-n_0$ as well as any externally applied time-dependent potentials, and U_E is the Ewald energy representing the nuclear-nuclear interactions in the presense of the neutralizing background of density $-n_0$. We start the time-dependent analysis out by defining the functional

$$\tilde{A}[u] = i\log \mathrm{Tr}\left\{e^{\beta\mu\hat{N}}\hat{V}(-i\beta;0)\right\}, \tag{1.5}$$

where $\beta = 1/(k_B T)$ is the inverse thermal energy, μ denotes the chemical potential

and $\hat{N}$ is the particle number operator. Also, $\hat{V}$ denotes the quantum-mechanical evolution operator from Keldysh time τ_i to τ_f and explicitly is given by

$$\hat{V}(\tau_i;\tau_f) = T_C \exp\left\{-i\int_{\tau_i}^{\tau_f} d\tau t'(\tau)\hat{H}(\tau)\right\}, \tag{1.6}$$

where T_C denotes the contour ordering operator and $t'(\tau)$ denotes the derivative of the physical time with respect to the Keldysh time. Note that because of the double-parametrization of the physical time by the Keldysh time $u(\boldsymbol{r},\tau)$ may have two different values at a particular physical time. The set of external potentials which are single-valued as functions of the physical time are referred to as physical potentials.

$\tilde{A}$ has the property

$$\frac{\delta\tilde{A}}{\delta u(\boldsymbol{r},\tau)} = n(\boldsymbol{r},\tau), \tag{1.7}$$

where $n(\boldsymbol{r},\tau)$ denotes the quantum-mechanically and thermally averaged electron density corresponding to $u(\boldsymbol{r},\tau)$.

For a particular external potential of interest $v(\boldsymbol{r},\tau)$, we then define the action functional $S[n]$, which is made stationary by the electron density corresponding to $v(\boldsymbol{r},\tau)$, via

$$S[n] = A[n] - \int_W d\boldsymbol{r}\int_C d\tau n(\boldsymbol{r},\tau)v(\boldsymbol{r},\tau), \tag{1.8}$$

where $A[n] = -\tilde{A}[u] + \int_W d\boldsymbol{r}\int_C d\tau n(\boldsymbol{r},\tau)u(\boldsymbol{r},\tau)$ denotes the intrinsic action, defined as the Legendre transform of $\tilde{A}$. In the above, W as usual denotes an open volume and C denotes the Keldysh contour.

To develop a time-dependent Kohn-Sham theory [24, 25], we partition the intrinsic action A into certain well-known contribution and an unknown remainder according to

$$A[n] = A_s[n] - A_{xc}[n] - \frac{1}{2}\int_W d\boldsymbol{r}\int_W d\boldsymbol{r}'\int_C d\tau\frac{(n(\boldsymbol{r},\tau)-n_0)\,(n(\boldsymbol{r}',\tau)-n_0)}{|\boldsymbol{r}-\boldsymbol{r}'|}, \tag{1.9}$$

where A_s denotes the intrinsic action of a set of noninteracting electrons and A_{xc} denotes the unknown exchange-correlation part.

Using $\delta A/\delta n = u$ and (1.9) we find

$$u(\boldsymbol{r},\tau) = u_s(\boldsymbol{r},\tau) - u_{xc}(\boldsymbol{r},\tau) - \int_W d\boldsymbol{r}' \frac{(n(\boldsymbol{r}',\tau) - n_0)}{|\boldsymbol{r}-\boldsymbol{r}'|}, \tag{1.10}$$

where u_s denotes the "effective" external potential which when acting on a system of noninteracting electrons gives rise to the same time-dependent density $n(\boldsymbol{r},\tau)$ as the potential u when acting on a system of interacting electrons. Above, we also defined $u_{xc} = \delta A_{xc}/\delta n$.

Practical calculations within time-dependent density-functional theory are usually carried out using linear response theory [24, 26], which maps the problem of finding the stationary density of the action onto a generalized eigenvalue equation similar to the Bethe-Salpeter equation of many-body perturbation theory [27, 28].

According to (1.10), a small perturbing external potential δu gives rise to the effective potential change

$$\delta u_s(\boldsymbol{r},\tau) = \delta u(\boldsymbol{r},\tau) + \int_W d\boldsymbol{r}' \int_C d\tau' \frac{\delta u_{xc}(\boldsymbol{r},\tau')}{\delta n(\boldsymbol{r}',\tau')} \delta n(\boldsymbol{r}',\tau) + \int_W d\boldsymbol{r}' \frac{\delta n(\boldsymbol{r}',\tau)}{|\boldsymbol{r}-\boldsymbol{r}'|}, \tag{1.11}$$

where the density change δn can be computed either by considering the response of interacting electrons to δu or by considering the response of noninteracting electrons to δu_s. For interacting electrons we find

$$\delta n(\boldsymbol{r},\tau) = \int_W d\boldsymbol{r}' \int_C d\tau' \chi(\boldsymbol{r},\boldsymbol{r}'|\tau-\tau') \delta u(\boldsymbol{r}',\tau'), \tag{1.12}$$

where χ denotes the density response function. For non-interacting electrons we find

$$\delta n(\boldsymbol{r},\tau) = \int_W d\boldsymbol{r}' \int_C d\tau' \chi_{KS}(\boldsymbol{r},\boldsymbol{r}'|\tau-\tau') \delta u_s(\boldsymbol{r}',\tau), \tag{1.13}$$

where χ_{KS} denotes the analytically known response function of non-interacting electrons. Combining (1.11), (1.12) and (1.13), we find the following self-consistent Dyson equation for χ, whose poles correspond to excitation energies of the interacting system,

$$\begin{aligned}\chi(\boldsymbol{r}_1,\boldsymbol{r}_2|\omega) &= \chi_{KS}(\boldsymbol{r}_1,\boldsymbol{r}_2|\omega)+\int_W d\boldsymbol{r}_3\int_W d\boldsymbol{r}_4\chi_{KS}(\boldsymbol{r}_1,\boldsymbol{r}_3|\omega)\\ &\times \left(\frac{1}{|\boldsymbol{r}_3-\boldsymbol{r}_4|}+f_{xc}(\boldsymbol{r}_3,\boldsymbol{r}_4|\omega)\right)\chi(\boldsymbol{r}_4,\boldsymbol{r}_2|\omega),\end{aligned} \tag{1.14}$$

with $f_{xc}=\delta u_{xc}/\delta n$.

This equation can be recast as a generalized eigenvalue equation

$$\sum_\nu \left(\delta_{\kappa\nu}\Delta\epsilon_\nu + M_{\kappa\nu}(\Omega)\right)F_\nu = \Omega F_\kappa, \tag{1.15}$$

where Ω denotes the energy of the excited state and we have introduced the transition-space notation [26], where the fused index $\kappa=(j,k)$ denotes a single-particle transition between Kohn-Sham orbitals $\phi_j(\boldsymbol{r})$ and $\phi_k(\boldsymbol{r})$. Also, $\Delta\epsilon_\kappa = \epsilon_j-\epsilon_k$ denotes a difference of Kohn-Sham energies and the coupling matrix M is given by

$$M_{\kappa\nu}(\Omega)=\alpha_\nu\int_W d\boldsymbol{r}\int_W d\boldsymbol{r}'\Phi^*_\kappa(\boldsymbol{r})\left[\frac{1}{|\boldsymbol{r}-\boldsymbol{r}'|}+f_{xc}(\boldsymbol{r},\boldsymbol{r}'|\Omega)\right]\Phi_\nu(\boldsymbol{r}'), \tag{1.16}$$

with $\Phi_\kappa(\boldsymbol{r})=\phi^*_k(\boldsymbol{r})\phi_j(\boldsymbol{r})$ and $\alpha_\kappa=f_k-f_j$, where $f_k=0$ or 2 denotes the number of electrons occupying the orbital $\phi_k(\boldsymbol{r})$.

Just like the density-functional theory for equilibrium systems, it is straightforward to generalize time-dependent density-functional theory to multicomponent systems, such as a solute/solvent system. In the joint time-dependent density-functional theory presented in chapter four we will start out from such a multicomponent theory and systematically eliminate environment degrees of freedom, while retaining the full *ab initio* description for the solute.

BIBLIOGRAPHY

[1] K. G. Wilson. *Phys. Rev. Mod.*, 47:773, 1975. 2

[2] M. E. Fisher. *Phys. Rev. Mod.*, 70:653, 1998. 2

[3] P. Hohenberg and W. Kohn. *Phys. Rev.*, 136:B864, 1964. 2, 7

[4] W. Kohn. *Phys. Rev. Mod.*, 71:1253, 1999. 2

[5] M. C. Payne, M. P. Teter, D. C. Allan, T. A. Arias, and J. D. Joannopoulos. *Phys. Rev. Mod.*, 64:1045, 1992. 2

[6] M. Born and R. Oppenheimer. *Ann. Phys. (Paris)*, 84:457, 1927. 2

[7] J. Tersoff. *Phys. Rev. B*, 39:5566, 1989. 2

[8] D. Frenkel and B. Smit. *Understanding Molecular Simulation: from algorithms to applications*. Academic Press, San Diego, California, 2002. 2

[9] M. P. Allen and D. J. Tildesley. *Computer Simulation of Liquids*. Clarendon Press, Oxford, 1987. 4

[10] N.W. Ashcroft. *Aust. J. Phys.*, 49:3, 1996. 4, 7

[11] C. Ebner, W.F. Saam, and D. Stroud. *Phys. Rev. A*, 14:2264, 1976. 5

[12] J.D. Weeks, K. Katsov, and K. Vollmayr. *Phys. Rev. Lett.*, 81:4400, 1998.

[13] W.A. Curtin and N.W. Ashcroft. *Phys. Rev. Lett.*, 56:2775, 1986. 5

[14] M. Cossi and V. Barone. *J. Chem. Phys.*, 115:4708, 2001. 5

[15] J. Kongsted, A. Osted, K. V. Mikkelsen, P.-O. Astrand, and O. Christiansen. *J. Chem. Phys.*, 121:8435, 2004. 5, 6

[16] L. D. Landau and E. M. Lifshitz. *Theory of Elasticity.* Pergamon Press, New York, 1986. 6, 7

[17] E. Runge and E. K. U. Gross. *Phys. Rev. Lett.*, 52:997, 1984. 7, 9, 10

[18] G. K.-L. Chan and R. Finken. *Phys. Rev. Lett.*, 94:183001, 2005. 7, 9

[19] N. D. Mermin. *Phys. Rev.*, 137:A1441, 1965. 7

[20] M. Levy. *Proc. Nat. Acad. Sci.*, 76:6062, 1979. 8

[21] E. Lieb. *Int. J. Quant. Chem.*, 24:243, 1983. 8

[22] J. L. Lebowitz and E. H. Lieb. *Phys. Rev. Lett.*, 22:631, 1969. 8

[23] E. H. Lieb and J. L. Lebowitz. *Adv. Math.*, 9:316, 1972. 8

[24] R. van Leeuwen. *Phys. Rev. Lett.*, 80:1280, 1998. 10, 11, 12

[25] W. Kohn and L. J. Sham. *Phys. Rev.*, 140:A1133, 1965. 11

[26] M. Petersilka, U. J. Grossmann, and E. K. U. Gross. *Phys. Rev. Lett.*, 76: 1212, 1995. 12, 13

[27] M. E. Casida. *Recent Developments and Applications of Modern Density Functional Theory, Theoretical and Computational Chemistry.* Elsevier Science, Amsterdam, 1996. 12

[28] M. Rohlfing and S. G. Louie. *Phys. Rev. Lett.*, 81:2312, 1998. 12

CHAPTER 2

KOHN-SHAM APPROACH TO THE CLASSICAL DENSITY-FUNCTIONAL THEORY OF MOLECULAR LIQUIDS

The Gordian knot of density-functional theories for classical molecular liquids remains finding an accurate free-energy functional in terms of the densities of the atomic sites of the molecules. Following Kohn and Sham, we show how to solve this problem by considering noninteracting molecules in a set of effective potentials. This shift in perspective leads to an accurate and computationally tractable description in terms of simple three-dimensional functions. We also treat both the linear- and saturation- dielectric responses of polar systems, presenting liquid hydrogen chloride as a case study.

2.1 Introduction

The importance of inhomogeneous polar molecular liquids, above all water, in the physical sciences can hardly be overstated: as solvents they are ubiquitous in soft condensed matter physics, biophysics, nanophysics, and chemical physics. The associated phenomena include hydrophobic interactions [1, 2], protein folding [3, 4], the behavior of colloidal suspensions [5], and phase transitions of confined liquids [6, 7]. Due to the complex interplay of hydrogen bonding, long-range polar interactions, and short-range excluded volume effects, developing a tractable physical theory to describe the solvent in these systems remains a challenge [8].

Despite the importance, inherent interest, and extensive experimental study of molecular liquids, most existing theories of the inhomogeneous phase of molecular liquids either lack the accuracy to describe the above phenomena in a quantitatively

satisfying way or become computationally prohibitive. The latter is particularly true for applications to complex systems, such as dissolved biomolecules or electrochemical interfaces. Simple dielectric continuum theories [9, 10] capture the dielectric response of the solvent at long length scales, but fail to describe more subtle effects at interfaces, such as the reorganization of the hydrogen-bond network or the binding of water molecules to solutes. Atomistic theories, on the other hand, describe such local effects quite well, but require the explicit treatment of many solvent molecules and also demand long simulation times to calculate statistically reliable thermodynamic averages. Since the fully-fledged *ab initio* molecular dynamics description of the solvent is only feasible for the smallest solutes, generally additional approximations become necessary in practice: Bernholc and coworkers, for example, have introduced a clever scheme which employs the full *ab initio* description only for a few solvent molecules adjacent to the solute and use rigid geometries and frozen electron densities for the remaining molecules [11]. In other studies, combination of *ab initio* methods for the solute with classical force field approaches [12–14] for the solvent yields additional simplifications. Despite the simplifications which such hybrid approaches allow, the need to compute many configurations to sample phase-space properly ultimately limits the size of systems which can be studied and thus the applicability of such approaches.

Ideally, one would have a rigorous description of the solvent which is able to combine the advantages of continuum theories (large system sizes and *implicit* thermodynamic averaging) with an explicit geometric description of the solvent molecule. Here, we make use of the fact that just such a theory can be developed by starting with the quantum mechanical free-energy functional for both the electrons and nuclei which comprise the liquid and, by "integrating out" the electrons, proceeding to construct a density functional in terms of atomic site densities alone.

This procedure is justified, of course, by the adiabatic separation of time scales of the electronic and nuclear degrees of freedom.

Such "classical" density-functional theories, which are founded on a number of exact theorems [15, 16], have been applied successfully to the study of simple liquids in the past [17, 18]. Historically, application of this method begins with a hard sphere reference system that is usually augmented by terms that capture weak long-range attractive forces [19]. Unfortunately, a hard sphere reference system is a poor starting point for the description of water because of the strong anisotropic short-range interactions arising from the molecular structure, including effects such as hydrogen bonding.

To remedy this, Chandler and coworkers [20, 21] introduced a density-functional theory for general molecular liquids in terms of a set of densities, one for each "interaction site" on the molecule (typically atomic centers). This theory was applied successfully to the freezing of diatomic liquids [22], the ordering of diblock copolymers [23], the crystallization of polyethylene [24] or the study of inhomogeneous polymer melts near a solid interface [25]. Woodward and coworkers developed a similar theory to study nonuniform melts and solutions of both flexible and semiflexible polymers [26–29].

However, the construction of accurate free-energy functionals for water and other molecular liquids within the theory of Chandler and coworkers proved difficult due to the "inversion problem", the difficulty of using *only* atomic site densities to express the entropy associated with the geometric structure of the molecules. Below, we show how this inversion problem can be overcome by a Kohn-Sham like change of variables from site densities to effective potentials and how the resulting functionals are both computationally tractable and can capture the basic

underlying physics of molecular liquids, including dielectric screening effects.

2.2 Kohn-Sham approach

The grand free energy $\Omega^{(ni)}$ of a noninteracting gas of neutral molecules is well-known as a functional of the *relative potentials* $\psi_\alpha(\mathbf{r}) \equiv \phi_\alpha(\mathbf{r}) - \mu_\alpha$, where $\phi_\alpha(\mathbf{r})$ is the species-dependent external potential, acting only on atomic constituents of type α, and μ_α is a species-specific chemical potential,

$$\Omega^{(ni)} = -k_B T n_r \int_V d^{3M} r \; s(\{\mathbf{r}_\alpha\}) e^{-\beta \sum_{\alpha=1}^{M} \psi_\alpha(\mathbf{r}_\alpha)}. \tag{2.1}$$

Here, $n_r = \langle N/V \rangle$ is the reference density at vanishing chemical potentials, M is the number of interaction sites on the molecule, and V denotes an open volume as required in the grand canonical ensemble. The intra-molecular distribution function $s(\{\mathbf{r}_\alpha\})$, which describes the geometry of the molecule, is given by

$$n_r s(\{\boldsymbol{r}_\alpha\}) = \langle N \delta(\boldsymbol{r}_1 - \boldsymbol{r}_1^{(1)}) \delta(\boldsymbol{r}_2 - \boldsymbol{r}_2^{(1)}) ... \delta(\boldsymbol{r}_M - \boldsymbol{r}_M^{(1)}) \rangle, \tag{2.2}$$

where $\boldsymbol{r}_j^{(i)}$ denotes the position of the j-th interaction site on the i-th molecule. $\Omega^{(ni)}$ is a key part of the interacting functional directly analogous to the noninteracting kinetic energy functional $T_s[n]$ of Kohn and Sham [30]. Unfortunately, (2.1) only gives $\Omega^{(ni)}$ as a functional of the ψ_α. To express $\Omega^{(ni)}$ in terms of site densities requires solution of $n_\alpha^{(ni)}(\mathbf{r}) = \delta\Omega^{(ni)}/\delta\psi_\alpha(\mathbf{r})$ as a set of M coupled integral equations for the $\psi_\alpha(\mathbf{r})$ in terms of the $n_\alpha^{(ni)}(\mathbf{r})$. This constitutes the "inversion problem" described above.

Chandler and coworkers have solved this inversion problem analytically in terms of an infinite continued fraction of convolutions for the *di*atomic case *only* [21]. The unwieldiness of this formal solution and its limitation to diatomics, however, has

led actual calculations to be performed in the *united-atom approximation*, where, for the noninteracting part of the functional, all of the sites of a molecule are assumed to coincide at a single point [31]. Despite its crudeness, the resulting theory predicts quite well the correct stable ice structure at nearly the correct density [31]. However, by uniting the sites, this approximation cannot capture the dielectric response of an ideal gas of polar molecules and so provides a poor starting point for the study of dielectric effects.

The key observation which allows us to overcome the inversion problem is that the free energy of a noninteracting molecular system, being a very complicated functional of the site densities, is a very simple functional of the relative potentials. This parallels the situation in electronic density-functional theory, where there is no known accurate functional for $T_s[n]$, the noninteracting (kinetic) energy, in terms of the density, but where this energy is easily written *exactly* in terms of single-particle orbitals. It was the transition from fully interacting electrons to a corresponding set of fictitious noninteracting particles, as proposed by Kohn and Sham [30], which allowed for the construction of accurate density functionals for the interacting electron gas. In the present case, the simplicity of evaluation of the grand free energy of noninteracting molecules as a functional of the relative potentials suggests an analogous change of variables, now from the site densities to a set of effective relative potentials in which fictitious noninteracting molecules move.

Mathematically, a pair of Legendre transformations achieves this change of variables. Thermodynamically, the Legendre transform $\Omega^{(ni)} - \sum \int_V dr\, \psi_\alpha n_\alpha$ equals the intrinsic Helmholtz free energy of the noninteracting system. Adding the internal energy U due to inter-molecular interactions and the contribution of the *physical*

external potentials ϕ_α yields the full Helmholtz free energy of the *interacting* system. Finally, the second Legendre transformation subtracts $\sum \int_V dr\, n_\alpha \mu_\alpha$ to form the full *interacting* grand free energy Ω as a functional of the *effective* potentials Ψ_α,

$$\Omega = \Omega^{(ni)} - \sum_{\alpha=1}^{M} \int_V d\boldsymbol{r}\, (\Psi_\alpha(\mathbf{r}) - \phi_\alpha(\mathbf{r}) + \mu_\alpha)\, n_\alpha(\mathbf{r}) + U[\mathbf{n}], \tag{2.3}$$

where $\boldsymbol{n} = \{n_1(\boldsymbol{r}), ..., n_M(\boldsymbol{r})\}$, the set of densities, is explicitly a functional of the effective relative potentials $\boldsymbol{\Psi} = \{\Psi_1(\boldsymbol{r}), ..., \Psi_M(\boldsymbol{r})\}$ via $n_\alpha(\mathbf{r}) = n_\alpha^{(ni)}[\boldsymbol{\Psi}](\mathbf{r}) \equiv \delta\Omega^{(ni)}/\delta\psi_\alpha(\mathbf{r})[\boldsymbol{\Psi}]$. Note that, in the above equation, only the *sum* of the chemical potentials bears physical meaning because the atomic sites are rigidly bonded and form *neutral* molecules. The effective relative potentials that minimize $\Omega[\boldsymbol{\Psi}]$ then determine the equilibrium site densities and allow for the calculation of the various equilibrium properties of the liquid. We mention that minimization with respect to the effective potential is known in the electron structure context as the optimized potential method [32].

We note that, contrary to Chandler and coworkers [21], who describe Ω as a functional of both site densities *and* effective potentials, $\Omega = \Omega[\boldsymbol{\Psi}, \boldsymbol{\rho}]$, we prefer the perspective of regarding Ω as a functional of the effective potentials *only*. As described above, this viewpoint is generally adopted in the context of electronic structure density-functional theory, where the total energy is expressed as a functional of Kohn-Sham orbitals only. It can easily be shown that both viewpoints are equivalent by using the stationarity of Chandler's free energy with respect to the effective potentials (Equation (4.8b) of reference 21) to express the densities in Ω in terms of Ψ's, $\Omega = \Omega[\boldsymbol{\Psi}, \boldsymbol{\rho}^{(ni)}(\boldsymbol{\Psi})]$. Both viewpoints therefore lead to the same field equations for the effective potentials.

We have a personal preference for the present formulation because having a

minimum principle allows us to employ efficient numerical techniques with which we are already familiar (such as the conjugate gradient method), with whatever advantages or disadvantages they bring in this new context. We note that one potential advantage of using a minimization technique is that each step of the solution yields an upper bound to the free energy. Also, the present formulation allows for a simple coupling of our theory to a quantum density-functional description of a solute: by combining the variational descriptions of the inhomogeneous solvent and the solute electrons into a single minimization procedure, we hope in the future to achieve a simple but accurate description of solvation processes, the ultimate goal of our work in this field.

2.3 Construction of approximate functionals

As usual with density-functional theories, the construction of the internal energy U is difficult. Again, we follow the lead of Kohn and Sham and construct a free-energy functional that reproduces established results for the homogeneous phase in the limit of vanishing external fields. The Ornstein-Zernike (OZ) equation gives information about the analytic structure of U, in particular it gives $\partial^2 U$, the Hessian of U with respect to the densities, as the difference between the inverses of the full and noninteracting correlation function matrices [33]. In the special case of the homogeneous phase, translational invariance then turns the OZ equation into a simple matrix equation in Fourier space, with one component for each field.

From now on, we will limit the discussion to a special class of liquids, which includes all diatomics and the liquid of most interest, water. The liquids in this class have the property that the lowest-order term in the long-wavelength expansion

of the Hessian of $U[\mathbf{n}]$ has the form

$$K_{\alpha\gamma}(\mathbf{k}) = \left(\frac{\epsilon}{\epsilon - 1} - \frac{\epsilon^{(ni)}}{\epsilon^{(ni)} - 1} \right) \frac{4\pi}{\mathbf{k}^2} q_\alpha q_\gamma, \tag{2.4}$$

where q_α are the partial site charges which obey $\sum_\alpha q_\alpha = 0$ because of the neutrality of the molecules, ϵ is the macroscopic dielectric constant and $\epsilon^{(ni)}$ is the dielectric constant of a system with intra-molecular correlations only. This result may be derived (the explicit proof is given in the final section of this chapter) by expanding the interacting and noninteracting correlation functions as $E + Fk^2 + \ldots$, where there are no linear terms in k by rotational invariance, and E and F are matrices of coefficients, with one combination of coefficients from F giving the dielectric constant. In the cases of molecules described either by two sites or by three sites with a mirror plane symmetry, one can show that the *only* combination of the coefficients in F which enters the leading-order term in the OZ equation corresponds *exactly* to the bulk dielectric constant. All liquids composed of such molecules thus have the property that the long-wavelength dielectric response can be built into the free-energy functional without *any* knowledge of the long-wavelength limit of the experimental correlation functions (other than ϵ).

We note that in (2.4) the handling of the $\boldsymbol{k} = 0$ term requires great care because of the singularity as $\boldsymbol{k} \to 0$. Because we always deal with neutral systems, the densities to which the operator K is applied also vanish as $\boldsymbol{k} \to 0$ and so there is no divergence in the integrand for the final functional. However, if the liquid in the system possesses a finite electric dipole $\boldsymbol{p}$, the densities will only vanish as $\boldsymbol{k} \cdot \boldsymbol{p}$ and the integrand at $\boldsymbol{k} = 0$ will behave like $(\boldsymbol{k} \cdot \boldsymbol{p})^2/\boldsymbol{k}^2$, which depends on the direction of approach to the origin. In the calculations presented below, we have made sure that the periodic unit cells never contain a net charge or a net dipole moment, so that the integrand is always well-defined.

In general, we may view the internal energy U as expanded in a power series in the density deviation from the uniform liquid, with all terms, except the quadratic part (whose Hessian is given by (2.4) in the long-wavelength limit) gathered into an excess part, F^{ex}, which plays exactly the same role as the exchange-correlation functional of Kohn-Sham theory: it ensures proper bulk thermodynamic behavior and will ultimately be treated in some approximate way. We note that the constant term in the power series expansion of U determines the bulk thermodynamics (which we include in F^{ex}) and the linear term vanishes in the uniform equilibrium state of the system. Putting this all together gives

$$U[\mathbf{n}] = \frac{1}{2}\sum_{\alpha,\gamma=1}^{M}\int_V d\boldsymbol{r}\int_V d\boldsymbol{r}'\; n_\alpha(\mathbf{r})\,\{K_{\alpha\gamma}(\mathbf{r},\mathbf{r}')+ C_{\alpha\gamma}(\mathbf{r},\mathbf{r}')\}\,n_\gamma(\mathbf{r}') + F^{ex}[\mathbf{n}], \tag{2.5}$$

where $C_{\alpha\gamma}$ describes those parts of the Hessian $\partial^2 U$ which K fails to capture.

To approximate F^{ex}, we first note that, in the case of zero external fields, all average densities are equal and the first quadratic term (K) in (2.5) vanishes because of charge neutrality. Anticipating that the matrix function C will be constructed to vanish in the long-wavelength limit, F^{ex} then captures all the internal energy of the uniform phase and can be expressed as $F^{ex} = V f^{ex}(n)$, with V being the volume and n the average molecular density. Due to the presence of multiple density fields, generalizing this expression to the inhomogeneous case is more difficult than for the analogous exchange-correlation energy in electronic structure theory. Also, because of the strong correlations induced by excluded volume effects, *purely local* excess functionals fail to describe the liquid state [34]. We therefore approximate F^{ex} with a simplified *ansatz* in the spirit of weighted density-functional theory [34], but generalized to multiple species by allowing different weights b_γ^i for the various

densities,

$$F^{ex}[\boldsymbol{n}] = \int_V d\boldsymbol{r} \sum_i p_i f^{ex} \left(\sum_{\gamma=1}^{M} b_\gamma^i \overline{n}_\gamma(\mathbf{r}) \right), \tag{2.6}$$

where we introduce the weighted densities

$$\overline{n}_\gamma(\mathbf{r}) = \int_V d\boldsymbol{r}' (\pi r_0^2)^{-3/2} \exp(-|\mathbf{r} - \mathbf{r}'|/r_0^2) n_\gamma(\mathbf{r}'), \tag{2.7}$$

with r_0 being a parameter ultimately fit to the experimental surface tension. To reduce to the correct form in the uniform case p_i and b_γ^i must fulfill $\sum_i p_i = 1$ and $\sum_{\gamma=1}^{M} b_\gamma^i = 1$. In the above equation, we employ a very simple gaussian weighting function. Such a weighting function was used in previous work on liquid water with encouraging results [35]. Also, successful density-functional theories for hard-sphere liquids, such as the fundamental measure approach [36], employ short-ranged weighting functions which average the density over roughly the volume of a hard sphere.

To capture the behavior of the scalar function $f^{ex}(n)$, we use a polynomial fit to various bulk thermodynamic conditions. The condition that C vanishes in the long-wavelength limit subsequently fixes p_i and b_γ^i and ensures that C will be bandwidth limited and thus amenable to numerical approximation. For a given r_0, this then completely specifies our approximation to F^{ex}. Next, relating $K + C + \partial^2 F^{ex}$ to the density-density correlation functions through the OZ relation then gives the matrix function C for a given r_0. Finally, we can determine r_0 by adjustment until calculations of the liquid-vapor interface give the correct surface tension.

2.4 Application to liquid hydrogen chloride

We choose liquid hydrogen chloride as a model physical system exhibiting hydrogen bonding and for which detailed experimental data are available, including site-site

correlation functions[37, 38]. At ambient pressure, the melting point of hydrogen chloride is at 159 K and the boiling point at 188 K [39].

Assuming rigid intra-molecular bonds, the distribution function becomes

$$s(\boldsymbol{r}_1, \boldsymbol{r}_2) = \delta(|\boldsymbol{r}_1 - \boldsymbol{r}_2| - B)/4\pi B^2, \tag{2.8}$$

with the gas phase bond length $B = 1.275$ Å taken from experiment [38] and 1 and 2 referring to hydrogen and chlorine, respectively. We then select the partial charges to yield the experimental gas phase dipole moment [40], resulting in $q_1 = -q_2 = 0.171\,e$ with e being the fundamental charge. Then, we approximate the simple bulk function $f^{ex}(n)$ by a fourth-order polynomial with coefficients adjusted to (a) reproduce the bulk modulus of the liquid phase and (b) to allow for coexistence of stable liquid and vapor phases at the appropriate densities, where the latter is treated as an ideal gas. Next, for the excess free-energy *functional*, the requirement that the matrix C vanishes in the long-wavelength limit fixes the integrand in (2.6) to be $[3f^{ex}(\overline{n}_1(\mathbf{r})) + 4f^{ex}\left((\overline{n}_1(\mathbf{r}) + \overline{n}_2(\mathbf{r}))/2\right) + 3f^{ex}(\overline{n}_2(\mathbf{r}))]/10$, under the assumption that the constant term (in an expansion in powers of k^2) of the inverse correlation function is proportional to that of the noninteracting case. Then, we determine C as described above using the partial structure factor data for the uniform liquid [37] and the macroscopic dielectric constant ($\epsilon = 11.3$, while the optical dielectric constant is $\epsilon_{opt} = 1.73$ and the mean molecular polarizability is given by $\bar{\alpha} = 17.41$ bohr^3 [38]) [41] as experimental inputs. Adjusting the smoothing parameter to give the experimental surface tension [42] yields $r_0 = 4.55$ Å.

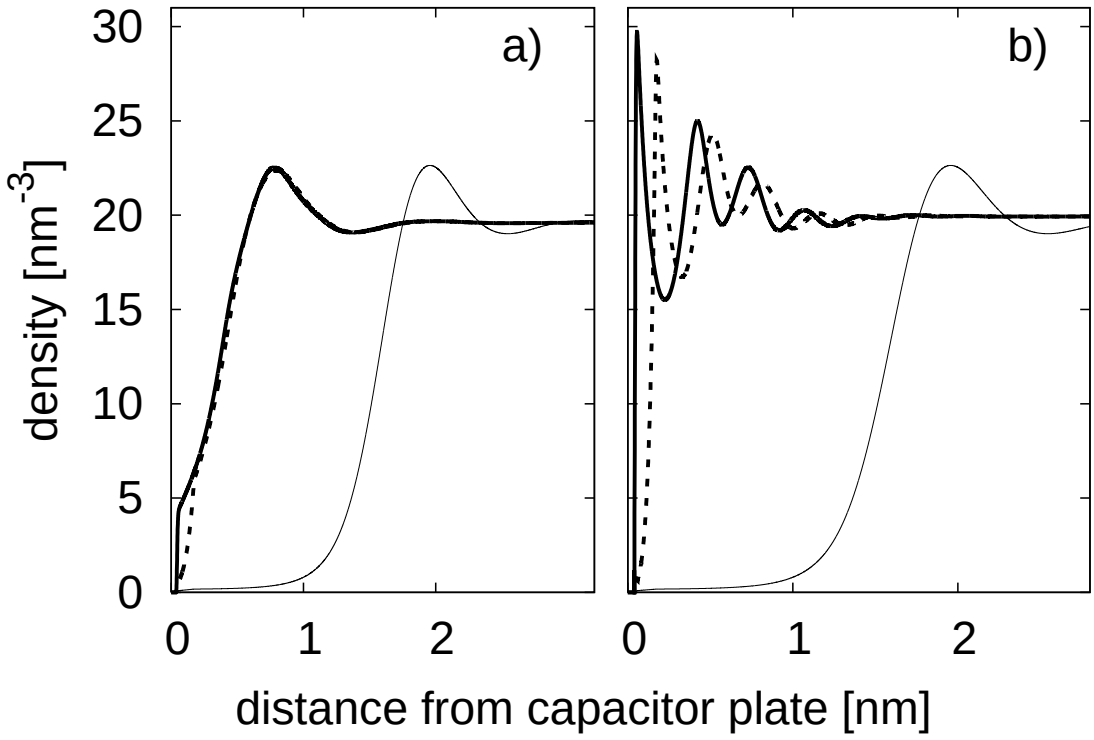

Figure 2.1: Hydrogen- (thick dotted curves) and chlorine- (thick solid curves) site density versus distance from hard wall in (a) moderate and (b) high applied field. Reference results for zero field given in both panels (thin solid curves).

2.5 Results

As a test case, we study the behavior of liquid hydrogen chloride at T=194 K, P=4.5 bar (chosen due to availability of experimental correlation functions [37]), which is in the liquid part of the phase diagram somewhere near the triple point. The experimental particle number density at this temperature and pressure is $n_r = 0.0196$ molecules/Å^3 [37].

For our calculations, we employ a periodic boundary conditions and a unit cell which contains *two* parallel plate capacitors with *opposing* dipole moments. This construction ensures that the total dipole moment of the unit cells vanishes and that the free energy per cell is well defined.

Figures 2.1(a,b) show the equilibrium density profiles which our theory predicts in a parallel plate capacitor (described as an infinite square-well potential for both species) in both moderate and strong applied fields, respectively. For comparison, the figure also shows the zero-field density profiles.

The zero-field profiles exhibit an extended gas phase region up to a distance of $\sim$ 1 nm from the plates. This "lingering" gas phase region exists because molecules can minimize the influence of the repulsive walls by leaving the system and entering the reservoir at very little free-energy cost. As soon as a relatively weak external electric displacement D is applied, however, it becomes favorable for the dipolar molecules to enter the capacitor, largely destroying the gas phase region and resulting in an almost rigid shift of the density profiles towards the capacitor walls for a large range of fields until the non-linear dielectric response regime is reached. Figure 2.1(a) shows an example of this behavior for a relatively large field but where the dielectric response is still fairly linear ($\alpha \equiv \beta pD = 2.68$,

where p is the molecular dipole moment). A dramatic qualitative change occurs in the strong field case. Figure 2.1(b), computed at $\alpha = 7.38$, shows the typical behavior in the high-field case. At large fields, the profile for each species exhibits a sharp peak followed by strong oscillations, where the peaks and oscillations are separated by one molecular bond length (~ 0.12 nm) indicating that they are the result of strong orientational ordering of the molecular dipoles. The oscillations of the site densities suggest an induced layering of molecules close to the surface, which results from the reorganization of the hydrogen-bond network in response to the increasing dipolar alignment of the molecules. The wavelength of the observed oscillations is about ~ 0.3 nm, corresponding to the length of the hydrogen bond [8].

The equilibrium site densities determine the induced polarization. Figure 2.2 compares the polarization, computed from our density-functional theory, to the result of self-consistently screened nonlinear electrostatics, computed by solving for the polarization P such that $P = P^{(ni)}(D - a_\epsilon 4\pi P)$, where $P^{(ni)}(E)$ is the response of a gas of noninteracting dipoles in a local field E and $a_\epsilon \equiv \epsilon/(\epsilon-1) - \epsilon^{(ni)}/(\epsilon^{(ni)}-1)$ ensures that for small D the correct linear response is recovered. Figure 2.2 shows that our density-functional theory not only reproduces the linear regime but also captures saturation effects.

In conclusion, we have shown how a Kohn-Sham-like change of variables yields a numerically efficient and accurate density-functional theory for molecular liquids. The resulting theory has the computational cost of the problem of a noninteracting gas of molecules in a self-consistent external potential. We have shown how to construct a functional in this approach which captures the coexistence of liquid and vapor phases, the surface tension between these phases, and, for the liquid, the bulk

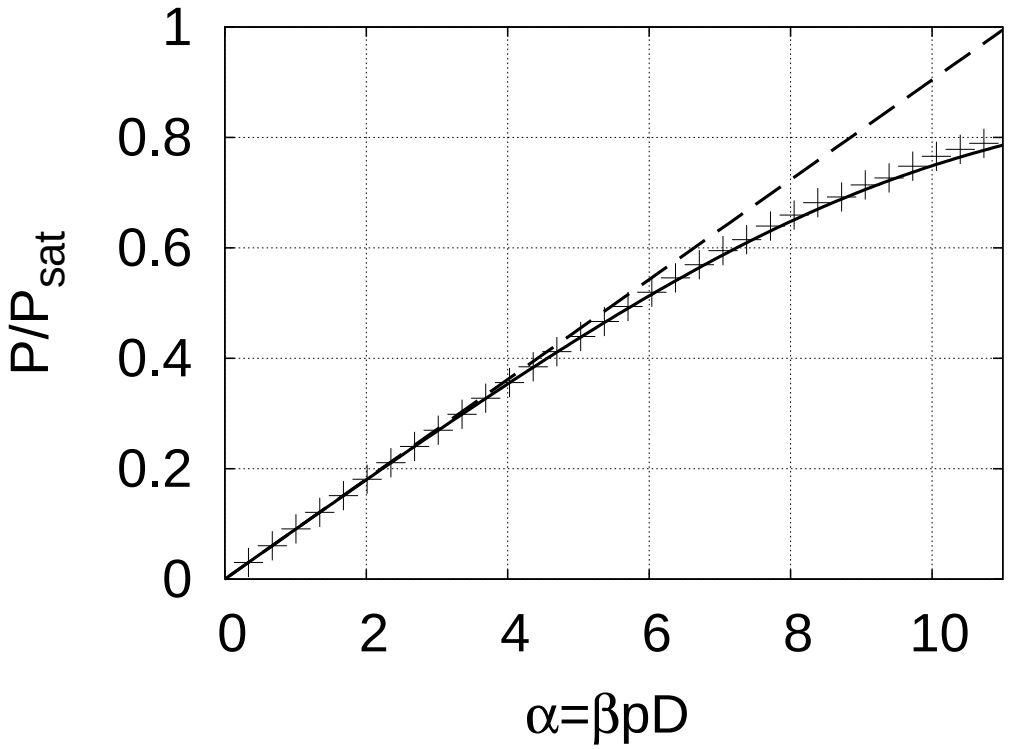

Figure 2.2: Dielectric saturation fraction (P/P_{sat}) versus applied electric displacement (D): density-functional results (crosses), non-linear electrostatics (solid line), linear response (dashed line).

mechanical properties, site-site correlation functions, linear dielectric response, and self-consistent dielectric saturation effects. Without modification, the current approach is ready to be developed for the liquid of greatest scientific interest: water.

2.6 Long-wavelength analysis of the Ornstein-Zernike equation

In this section, we demonstrate in two steps that $K_{\alpha\gamma}$, given in (2.4), indeed constitutes the leading order term in the long-wavelength expansion of the Hessian of U: first, we show that for a certain class of molecular liquids comprising all diatomic liquids and also water $K_{\alpha\gamma}(\boldsymbol{k})$ is proportional to the Coulomb interaction between interaction sites, given by $4\pi q_\alpha q_\gamma/\boldsymbol{k}^2$ with α and γ ranging from 1 to M, the total number of atoms comprising the molecule. Then, we demonstrate that the constant of proportionality indeed is $\epsilon/(\epsilon-1) - \epsilon^{(ni)}/(\epsilon^{(ni)}-1)$.

It is important to recall that we express the free energy as a functional of M density fields, one for each atomic constituent of the molecule. Traditionally, the Ornstein-Zernike equation has been employed in the study of mono-atomic liquids, where only one density field is needed. In this special case, the Ornstein-Zernike equation is typically written in the form

$$h(\boldsymbol{r}_1,\boldsymbol{r}_2) = c^{(2)}(\boldsymbol{r}_1,\boldsymbol{r}_2) + \int_V d\boldsymbol{r}_3 h(\boldsymbol{r}_1,\boldsymbol{r}_3) n(\boldsymbol{r}_3) c^{(2)}(\boldsymbol{r}_3,\boldsymbol{r}_2), \tag{2.9}$$

where $h(\boldsymbol{r}_1,\boldsymbol{r}_2)$ denotes the total correlation function, which is closely related to the experimentally observable structure factor, and $c^{(2)}$ denotes the two-body direct correlation function which is proportional to the second functional derivative of

the excess free energy, which for mono-atomic liquids is typically defined as the difference of the total free energy and the ideal gas contribution. For a thorough introduction into the theory of mono-atomic liquid, we recommend the book by Henderson [33].

In our classical density-functional theory for molecular liquids, the Ornstein-Zernike equation becomes a matrix equation. Just as in the mono-atomic case, it relates second functional derivatives of U, the difference of the total internal free energy and the molecular gas contribution, to experimentally observable correlation functions.

Before we prove the above statements, we introduce some useful nomenclature for symmetric $M \times M$ matrices. In particular, we write a general symmetric matrix A as

$$A = \begin{bmatrix} a & \boldsymbol{a}^T \\ \boldsymbol{a} & \tilde{A} \end{bmatrix}, \tag{2.10}$$

where $a = A_{1,1}$ denotes the head of the A, the $(M-1)$-component column vector $\boldsymbol{a}$ the wing and the symmetric $(M-1) \times (M-1)$ matrix $\tilde{A}$ the body of A.

To prove our first claim, namely that $K_{\alpha\gamma}(\boldsymbol{k}) \propto 4\pi q_\alpha q_\gamma / \boldsymbol{k}^2$, we examine the Hessian of U, $[\partial^2 U]_{\alpha\gamma}(\boldsymbol{r}, \boldsymbol{r}') \equiv \delta^2 U / \delta n_\alpha(\boldsymbol{r}) \delta n_\gamma(\boldsymbol{r}')$, which is related to experimentally accessible correlation functions via the Ornstein-Zernike equation,

$$\partial^2 U(\boldsymbol{r}, \boldsymbol{r}') = \beta^{-1} \left(G^{-1}(\boldsymbol{r}, \boldsymbol{r}') - G^{-1}_{(ni)}(\boldsymbol{r}, \boldsymbol{r}') \right), \tag{2.11}$$

where $G_{\alpha\gamma}(\boldsymbol{r}, \boldsymbol{r}') = \langle n_\alpha(\boldsymbol{r}) n_\gamma(\boldsymbol{r}') \rangle - \langle n_\alpha(\boldsymbol{r}) \rangle \langle n_\gamma(\boldsymbol{r}') \rangle$ denotes the matrix of site-specific density-density correlation functions of the fully interacting liquid and $G_{(ni)}$ denotes the analogous quantity in a system without intermolecular interactions. We express G as the sum of $G_{(ni)}$ and a remainder due to intermolecular

interactions,

$$G = G_{(ni)} + n_r S, \tag{2.12}$$

where S denotes the matrix of partial structure factors.

In a uniform system, translational and rotational invariance determine the behavior of the correlations functions at small wavevectors. For the correlation function of the interacting system we find

$$G_{\alpha\gamma}(\boldsymbol{k}) = G^{(0)} + G^{(2)}_{\alpha\gamma}\boldsymbol{k}^2 + \mathcal{O}(\boldsymbol{k}^4), \tag{2.13}$$

where the constant $G^{(0)}$, which is related to the compressibility of the liquid via a thermodynamic sum rule [8], is *independent* of α and γ. Of course, a similar long wavelength expansion exists for $G_{(ni)}$. Rewriting (2.13) as a matrix expression, we find

$$G(\boldsymbol{k}) = G^{(0)}\boldsymbol{v}\boldsymbol{v}^T + G^{(2)}\boldsymbol{k}^2 + \mathcal{O}(\boldsymbol{k}^4), \tag{2.14}$$

where $\boldsymbol{v}$ denotes the column vector with all M components equal to one. This explicit form of the correlation function matrices motivates us to change the basis of the M-dimensional vector space from the original interaction site basis to a new basis whose first unit vector is parallel to $\boldsymbol{v}$. We choose the second basis vector parallel to $\boldsymbol{q}$, the vector of partial charges, which because of the neutrality of the molecules is orthogonal to $\boldsymbol{v}$.

In the new basis, the $G(\boldsymbol{k})$ is given by

$$G(\boldsymbol{k}) = \begin{bmatrix} G^{(0)} & \mathbf{0}^T \\ \mathbf{0} & \tilde{0} \end{bmatrix} + G^{(2)}\boldsymbol{k}^2 + \mathcal{O}(\boldsymbol{k}^4), \tag{2.15}$$

where $\mathbf{0}$ denotes a $(M-1)$-component column vector with all components equal to zero and $\tilde{0}$ denotes an analogous $(M-1)\times(M-1)$ matrix.

Next, to evaluate (2.11), we need the inverses of G and $G_{(ni)}$. In the long-wavelength limit, $G^{-1}(\boldsymbol{k})$ is given by

$$G^{-1}(\boldsymbol{k}) = \frac{1}{\boldsymbol{k}^2} \begin{bmatrix} 0 & \mathbf{0}^T \\ \mathbf{0} & [\tilde{G}^{(2)}]^{-1} \end{bmatrix} + \mathcal{O}(1). \tag{2.16}$$

This finding can easily be verified by multiplying $G^{-1}(\boldsymbol{k})$ by $G(\boldsymbol{k})$ in (2.15). Again, an analogous expression for $G_{(ni)}$ can be derived. Inserting these results into the Ornstein-Zernike equation, we find

$$\begin{aligned} \partial^2 U(\boldsymbol{k}) &= \beta^{-1} \left(G^{-1}(\boldsymbol{k}) - G^{-1}_{(ni)}(\boldsymbol{k}) \right) \\ &= \frac{1}{\beta \boldsymbol{k}^2} \left(\begin{bmatrix} 0 & \mathbf{0}^T \\ \mathbf{0} & [\tilde{G}^{(2)}]^{-1} \end{bmatrix} - \begin{bmatrix} 0 & \mathbf{0}^T \\ \mathbf{0} & [\tilde{G}^{(2)}_{(ni)}]^{-1} \end{bmatrix} \right) + \mathcal{O}(1). \end{aligned} \tag{2.17}$$

In the case of diatomic liquids, $\tilde{G}^{(2)}$ is simply a number and we immediately find the desired result that $\partial^2 U$ is proportional to the Coulomb interaction $4\pi q_\alpha q_\gamma / \boldsymbol{k}^2$ (recall that the second basis vector is chosen parallel to the vector of partial charges).

In the case of water, we choose the third basis vector along $(0, 1, -1)$. The identity of the two hydrogens of the water molecule dictates that in the original interaction site basis all components of $\tilde{S}^{(2)}$ are equal and that $\tilde{G}^{(2)}_{(ni)}$ is symmetric with its diagonal elements being equal. In the new basis, we then find the following expression for $\tilde{G}^{(2)}$,

$$\tilde{G}^{(2)} = \tilde{G}^{(2)}_{(ni)} + n_r \tilde{S}^{(2)} = \begin{bmatrix} \tilde{G}^{(2)}_{(ni)1,1} & 0 \\ 0 & \tilde{G}^{(2)}_{(ni)2,2} \end{bmatrix} + n_r \begin{bmatrix} \tilde{S}^{(2)}_{1,1} & 0 \\ 0 & 0 \end{bmatrix}. \tag{2.18}$$

Inserting this result into (2.17), we again find that the Hessian of U is proportional to the Coulomb interaction, as we had claimed.

Having established that $\partial^2 U = \xi 4\pi \boldsymbol{q}\boldsymbol{q}^T / \boldsymbol{k}^2$ for all diatomic liquids and also for water, we now prove that the constant of proportionality ξ is given by $\epsilon/(\epsilon - 1) - \epsilon^{(ni)}/(\epsilon^{(ni)} - 1)$.

We first recall the general connection between correlation functions and response functions provided by statistical mechanics. In particular, for a liquid whose dielectric response is dominated by the reorientation of permanent dipoles the wavevector-dependent dielectric function $\epsilon(\boldsymbol{k})$ is related to the correlation function of the uniform interacting liquid via [43]

$$\frac{\epsilon(\boldsymbol{k})-1}{\epsilon(\boldsymbol{k})} = \frac{4\pi\beta}{\boldsymbol{k}^2}\boldsymbol{q}^T G \boldsymbol{q}. \tag{2.19}$$

We note that our theory of liquid water contains no explicit electronic degrees of freedom and therefore the above equation contains no contribution from the molecular polarizabilities.

As $\boldsymbol{k}$ approaches zero, this equation becomes

$$\frac{\epsilon}{\epsilon-1} = 4\pi\beta\boldsymbol{q}^2\tilde{G}^{(2)}_{1,1}, \tag{2.20}$$

where $\epsilon \equiv \epsilon(\boldsymbol{k}=0)$ and we expressed the correlation function in the new basis described above. To relate ξ to the correlation function, we again use the Ornstein-Zernike equation. In the long-wavelength limit, we find

$$G^{-1}(\boldsymbol{k}) = G^{-1}_{(ni)}(\boldsymbol{k}) + \xi\frac{4\pi\beta}{\boldsymbol{k}^2}\boldsymbol{q}\boldsymbol{q}^T. \tag{2.21}$$

To relate ξ to the macroscopic dielectric response, we have to invert G^{-1} to obtain $\tilde{G}^{(2)}_{1,1}$ in terms of ξ. According to (2.16), it is sufficient to invert

$$[\tilde{G}^{(2)}]^{-1} = [\tilde{G}^{(2)}_{(ni)}]^{-1} + \xi 4\pi\beta\tilde{\boldsymbol{q}}\tilde{\boldsymbol{q}}^T \equiv D(\xi), \tag{2.22}$$

where $\tilde{\boldsymbol{q}}$ denotes the $(M-1)$-component column vector obtained by eliminating the first element of $\boldsymbol{q}$ and we have introduced the matrix $D(\alpha)$ with $D(0) = [\tilde{G}^{(2)}_{(ni)}]^{-1}$ and $D(\xi) = [\tilde{G}^{(2)}]^{-1}$. Because $D(0)$ and $D(\xi)$ only differ in the element located in the first column of the first row, the cofactors $C_{1,1}$ appearing in the expressions for

$[D(0)]^{-1}_{1,1}$ and $[D(\xi)]^{-1}_{1,1}$ are equal according to Cramer's rule,

$$[D(0)]^{-1}_{1,1} = \frac{C_{1,1}}{\det D(0)}, \tag{2.23}$$

$$(D(\xi))^{-1}_{1,1} = \frac{C_{1,1}}{\det D(\xi)} = \frac{C_{1,1}}{\det D(0) + \xi 4\pi\beta \boldsymbol{q}^2 C_{1,1}}, \tag{2.24}$$

where, again, the relation between the determinants, $\det D(\xi) = \det D(0) + \xi 4\pi\beta\boldsymbol{q}^2 C_{1,1}$, is a consequence of the special structure of (2.22).

Using the first of the above equations to eliminate $C_{1,1}$ and substituting back the explicit correlation function matrices, we find the following relation between $\tilde{G}^{(2)}_{(ni)1,1}$, $\tilde{G}^{(2)}_{1,1}$ and ξ,

$$\tilde{G}^{(2)}_{1,1} = \frac{\tilde{G}^{(2)}_{(ni)1,1}}{1 + \xi 4\pi\beta\boldsymbol{q}^2 \tilde{G}^{(2)}_{(ni)1,1}}. \tag{2.25}$$

Finally, we solve for ξ and use (2.19) in both the interacting and noninteracting case to find

$$\xi 4\pi\beta\boldsymbol{q}^2 = \frac{1}{\tilde{G}^{(2)}_{(1,1)}} - \frac{1}{\tilde{G}^{(2)}_{(ni)(1,1)}} = 4\pi\beta\boldsymbol{q}^2 \left\{ \frac{\epsilon}{\epsilon - 1} - \frac{\epsilon^{(ni)}}{\epsilon^{(ni)} - 1} \right\}. \tag{2.26}$$

This completes the proof.

BIBLIOGRAPHY

[1] D. Chandler. *Nature*, 437:640, 2005. 16

[2] H.S. Ashbaugh and L.R. Pratt. *Rev. Mod. Phys.*, 78:159, 2006. 16

[3] P. Liu, X. Huang, R. Zhou, and B.J. Berne. *Nature*, 437:159, 2005. 16

[4] M. Tarek and D.J. Tobias. *Phys. Rev. Lett.*, 88:138101, 2002. 16

[5] J. Israelachvili and H. Wennerstroem. *Nature*, 379:219, 1996. 16

[6] G. Hummer, J.C. Rasaiah, and J.P. Noworyta. *Nature*, 414:188, 2001. 16

[7] Y. Leng and P.T. Cummings. *Phys. Rev. Lett.*, 94:026101, 2005. 16

[8] J.-P. Hansen and I.R. McDonald. *Theory of Simple Liquids*. Academic Press, London, 2006. 16, 29, 33

[9] S. Miertus, E. Scrocco, and J. Tomasi. *Chem. Phys.*, 55:117, 1981. 17

[10] R. Cammi and J. Tomasi. *J. Comput. Chem.*, 16:1449, 1995. 17

[11] M. Hodac, W. Lu, and J. Bernholc. *J. Chem. Phys.*, 128:014101, 2008. 17

[12] A. Warshel and M. Levitt. *J. Mol. Biol.*, 102:227, 1976. 17

[13] U.C. Singh and P.A. Kollmann. *J. Comput. Chem.*, 7:718, 1986.

[14] M.J. Field, P.A. Bash, and M. Karplus. *J. Comput. Chem.*, 11:700, 1990. 17

[15] N.D. Mermin. *Phys. Rev.*, 137:A1441, 1965. 18

[16] N.W. Ashcroft. *Aust. J. Phys.*, 49:3, 1996. 18

[17] C. Ebner, W.F. Saam, and D. Stroud. *Phys. Rev. A*, 14:2264, 1976. 18

[18] W.A. Curtin and N.W. Ashcroft. *Phys. Rev. Lett.*, 56:2775, 1986. 18

[19] J.D. Weeks, K. Katsov, and K. Vollmayr. *Phys. Rev. Lett.*, 81:4400, 1998. 18

[20] D. Chandler, J.D. McCoy, and S.J. Singer. *J. Chem. Phys.*, 85:5971, 1986. 18

[21] D. Chandler, J.D. McCoy, and S.J. Singer. *J. Chem. Phys.*, 85:5978, 1986. 18, 19, 21

[22] J.D. McCoy, S.J. Singer, and D. Chandler. *J. Chem. Phys.*, 87:4853, 1987. 18

[23] S.K. Nath, J.D. McCoy, J.G. Curro, and R.S. Saunders. *J. Chem. Phys.*, 106: 1950, 1997. 18

[24] J.D. McCoy, K.G. Honnell, K.S. Schweizer, and J.G. Curro. *J. Chem. Phys.*, 95:9348, 1991. 18

[25] S. Sen, J.M. Cohen, J.D. McCoy, and J.G. Curro. *J. Chem. Phys.*, 101:9010, 1994. 18

[26] C.E. Woodward. *J. Chem. Phys.*, 94:3183, 1990. 18

[27] A. Yethiraj and C.E. Woodward. *J. Chem. Phys.*, 102:5499, 1995.

[28] C.E. Woodward and A. Yethiraj. *J. Chem. Phys.*, 100:3181, 1994.

[29] J. Forsman and C.E. Woodward. *Macromol.*, 39:1261, 2006. 18

[30] W. Kohn and L.J. Sham. *Phys. Rev.*, 140:A1133, 1965. 19, 20

[31] K. Ding, D. Chandler, S.J. Smithline, and A.D.J. Haymet. *Phys. Rev. Lett.*, 59:1698, 1987. 20

[32] J.D. Talman and W.F. Shadwick. *Phys. Rev. A*, 14:36, 1976. 21

[33] R. Evans. *Fundamentals of Inhomogeneous Fluids*, page 85. Dekker, New York, 1992. 22, 32

[34] W.A. Curtin and N.W. Ashcroft. *Phys. Rev. A*, 32:2909, 1985. 24

[35] S. A. Petrosyan, D. Roundy, J.-F. Briere, and T. A. Arias. *arXiv: 1001.2350 [cond-mat]*, 2010. 25

[36] Yaakov Rosenfeld. Free-energy model for the inhomogeneous hard-sphere fluid mixture and density-functional theory of freezing. *Phys. Rev. Lett.*, 63(9):980–983, Aug 1989. doi: 10.1103/PhysRevLett.63.980. 25

[37] C. Andreani, M.A. Ricci, M. Nardone, F.P. Ricci, and A.K. Soper. *J. Chem. Phys.*, 107:214, 1997. 26, 28

[38] V. Dubois and A. Pasquarello. *J. Chem. Phys.*, 122:114512, 2005. 26

[39] D.R. Lide, editor. *Handbook of Chemistry and Physics.* CRC Press, Inc., 1995. 26

[40] F. H. DeLeeuw and A. Dymanus. *J. Mol. Spectrosc.*, 48:427, 1973. 26

[41] R.W. Swenson and R.H. Cole. *J. Chem. Phys.*, 22:284, 1954. 26

[42] L.S. Adler and C.L. Yaws. *Solid State Technol.*, 19:35, 1976. 26

[43] D. Chandler. *J. Chem. Phys.*, 67:1113, 1977. 35

CHAPTER 3

A NEW CLASSICAL DENSITY-FUNCTIONAL THEORY OF INHOMOGENEOUS WATER

We present an accurate free-energy functional for liquid water written in terms of a set of effective potential fields in which fictitious noninteracting water molecules move. The functional contains an *exact* expression of the entropy of noninteracting molecules and thus provides an ideal starting point for the inclusion of complex inter-molecular interactions which depend on the *orientation* of the interacting molecules. We show how an excess free-energy functional can be constructed to reproduce the following properties of water: the dielectric response; the experimental site-site correlation functions; the surface tension; the bulk modulus of the liquid and the variation of this modulus with pressure; the density of the liquid and the vapor phase; and liquid-vapor coexistence. As a demonstration, we present results for the application of this theory to the behavior of liquid water in a parallel plate capacitor. In particular, we make predictions for the dielectric response of water in the nonlinear regime, finding excellent agreement with known data.

3.1 Introduction

Water is the most important liquid on earth. Although its uniform phase already exhibits many fascinating properties and is currently an area of intensive research, the importance of the *inhomogeneous* phase in the chemical and biological sciences is even greater: as a solvent, water is ubiquitous in physical chemistry, biochemistry and electrochemistry. The associated phenomena include hydrophobic interactions [1, 2], protein folding [3, 4], the electrochemical interface [5], and phase transitions of confined liquids [6, 7]. Due to the complex interplay of hydrogen bonding, long-

range polar interactions, and short-range excluded volume effects, developing a tractable theory to describe the solvent in the aforementioned systems remains a challenge [8].

The density-functional theory of molecular liquids introduced in the previous chapter combines computational efficiency with an accurate theoretical foundation. However, because of the more complicated bonding geometry of the triatomic water molecule, evaluation of the free energy of a molecular gas proves more difficult than in the case of the diatomic hydrogen chloride liquid.

Previous applications of molecular density-functional theory to the specific case of water dealt with this problem in two ways: either a simplified treatment of the bonding constraints was employed [9] or explicit atomistic simulations were used to treat the bonding constraints exactly [10].

Ding and coworkers [9] employ a simplified free energy functional to study the freezing of water. The free energy is divided into an entropic part and an enthalpic part. The entropic part is treated in a numerically convenient approximation which employs the *average* atomic density only and contains no information about the bonding constraints, such as bond lengths or bond angles. These constraints are then imposed during the minimization procedure. In order to describe crystalline ice, Ding and coworkers impose the bonding constraints by placing trial densities at the correct atomic positions. From the resulting free energies, they successfully predict the correct, hydrogen-bonded structure of ice. This treatment of molecular bonding, however, is not well suited for full variational exploration of the equilibrium densities of an inhomogeneous molecular liquid, particularly in an external electric field, because of the difficulty of constraining the minimization to enforce the correct molecular structure. In particular, without such additional constraints,

Ding *et al.*'s theory does not prohibit separation of the molecular sites to arbitrary distances from each other and exhibits only *linear* dielectric response in a capacitor geometry. To capture properly *nonlinear* dielectric effects, which play an important role in the solvation of biomolecules and ions [11], a more accurate evaluation of the entropic part of the free energy is necessary. Below, we describe a numerically convenient method which not only imposes the bonding constraints but also, unlike the approach of Ding and coworkers, makes no approximation with regard to the entropic part.

To capture explicitly effects of the molecular geometry in the liquid phase, which are important to the nonlinear dielectric response, Reddy and coworkers [10] combine Chandler's density-functional theory with explicit atomistic simulations: in each cycle of their self-consistency loop they employ a Monte Carlo calculation to compute the behavior of non-interacting water molecules in a set of effective potentials. The theory yields partial radial distribution functions in good agreement with molecular dynamics calculations of SPC water at high temperatures. However, the need for an explicit Monte Carlo calculation in each cycle makes the theory much more numerically demanding than Chandler's water functional written in terms of site densities only.

In this chapter, we apply the classical density-functional theory of molecular liquids, introduced in the previous chapter, to the specific case of liquid water. In particular, we construct a free energy functional for water, which takes molecular bonding constraints *fully* into account without having to carry out time-consuming explicit atomistic calculations. This free energy functional is written in terms of effective potentials *only* and can be minimized directly via the conjugate gradient method, making it ideal for large system sizes such as those needed to study the

solvation of biomolecules. It reproduces the equation of state of water, the surface tension, the experimental site-site correlation functions, and the macroscopic dielectric response. We note that previous works on different physical systems also treated the bonding constraints exactly without having to carry out explicit simulations: McCoy and coworkers study the freezing of a diatomic liquid [12], where for each molecule there is only a single bond, and Woodward and coworkers investigate the behavior of flexible and semi-flexible polymers [13, 14], but employ different techniques to deal with the bonding constraint than we present below.

3.2 Brief review of key results from the previous chapter

As we learned in the previous chapter, computationally efficient and accurate functionals with firm theoretical foundations for small, polar liquids can be constructed in the following form

$$\Omega = \Omega^{(ni)} - \sum_{\alpha=1}^{M} \int_V d\boldsymbol{r}\, (\Psi_\alpha(\mathbf{r}) - \phi_\alpha(\mathbf{r}) + \mu_\alpha)\, n_\alpha(\mathbf{r}) + U[\mathbf{n}], \tag{3.1}$$

where $\Omega^{(ni)} = -k_B T n_r \int_V d^{3M}r\ s(\{\mathbf{r}_\alpha\}) \exp\{-\beta \sum_{\alpha=1}^{M} \psi_\alpha(\mathbf{r}_\alpha)\}$ denotes the grand-free energy of the molecular gas with s being the molecular distribution function. Also, ϕ_α, Ψ_α and μ_α are the species-specific external, effective and chemical potentials, while n_α denote the site densities. The contribution to the grand free energy due to intermolecular interactions is

$$U = \frac{1}{2} \sum_{\alpha,\gamma} \int_V d\boldsymbol{r} \int_V d\boldsymbol{r}'\ n_\alpha(\mathbf{r}) \{K_{\alpha\gamma}(\mathbf{r},\mathbf{r}') + C_{\alpha\gamma}(\mathbf{r},\mathbf{r}')\} n_\gamma(\mathbf{r}') + F^{ex}[\mathbf{n}], \tag{3.2}$$

where $K_{\alpha\gamma}$ is analytically known and ensures the correct linear dielectric response of the liquid; $C_{\alpha\gamma}$ is obtained by solving the Ornstein-Zernike equation with experimentally measured correlation functions as input and captures the structure

of the liquid. In the future, when accurate correlation function data from *ab initio* calculations are available, one could envision the use of such an *ab initio* input instead of using experimental data.

Finally, the remainder F^{ex} incorporates important thermodynamic properties of the liquid, such as liquid-vapor coexistence or the experimental bulk modulus, and is given by

$$F^{ex}[\boldsymbol{n}] = \int_V d\boldsymbol{r} \sum_i p_i f^{ex} \left(\sum_{\gamma=1}^{M} b_\gamma^i \overline{n}_\gamma(\mathbf{r}) \right), \tag{3.3}$$

where f^{ex} denotes the excess free energy per unit volume of a homogeneous liquid, b_γ^i and p_i are parameters determined below and we introduce the weighted densities $\overline{n}_\gamma(\mathbf{r}) = \int_V d\boldsymbol{r}'(\pi r_0^2)^{-3/2} \exp(-|\mathbf{r} - \mathbf{r}'|/r_0^2) n_\gamma(\mathbf{r}')$, with r_0 being a parameter ultimately fit to the experimental surface tension.

To apply this theory to water, we need to find a numerically efficient method for evaluation of $\Omega^{(ni)}$, which is much more challenging for triatomic molecules because of the complicated structure of the molecular distribution function. Fortunately, $K_{\alpha\gamma}$ is still known known analytically, and $C_{\alpha\gamma}$, which captures the physics of hydrogen bonding, can again be extracted from experimental data, as we do below. Finally, F^{ex} once again requires knowledge of the thermodynamic properties of water, to which we have access, and which we again will fit with a polynomial.

3.3 Intramolecular free energy

In this section, we show how to evaluate $\Omega^{(ni)}$, defined in (2.1) in the previous chapter, for the specific case of liquid water *without* the additional simplifications or explicit atomistic simulations that other authors have employed, as described above.

Assuming rigid bonds of fixed length (and thus rigid angles as well) the intramolecular distribution function of a water molecule (normalized to integrate to the volume of the system) is

$$s(\mathbf{r}_0, \mathbf{r}_1, \mathbf{r}_2) = \frac{\delta(|\mathbf{r}_{10}| - B)}{4\pi B^2} \frac{\delta(|\mathbf{r}_{20}| - B)}{4\pi B^2} \times 2\delta(\hat{\mathbf{r}}_{10} \cdot \hat{\mathbf{r}}_{20} - \cos\theta_B), \tag{3.4}$$

where $B = 1$ Å is the oxygen-hydrogen bond length taken from the SPC/E [15] model of water, θ_B is the bond angle between the hydrogens and taken to be the tetrahedral angle like in the SPC/E model. Also, the label 0 refers to the oxygen atom and the labels 1 and 2 to the two hydrogens, and we define $\mathbf{r}_{ij} \equiv \mathbf{r}_i - \mathbf{r}_j$. Contrary to the case of diatomic molecules, where the assumption of rigid bonds turns $\Omega^{(ni)}$ into a convolution, numerical evaluation of (2.1) proves more challenging in the triatomic case because of the complex, nine-dimensional form of s. We note that real water molecules are, of course, not rigidly bonded. Deviations from rigidity, for example due to the zero-point motion of the hydrogens, can be captured by a more realistic model for s. However, the success of rigid models for the water molecule, such as the standard SPC model, suggest that those contributions are of minor importance.

We also note that the assumption of rigid bonding imposes an infinite energy cost for the ionization of a water molecule. In the current theory, the presence of ions is neglected. This is often a reasonable approximation because the Debye screening length of pure water (corresponding to a pH of approximately 7) is large compared to molecular length scales. To model pH, one would have to introduce explicit ionic species corresponding to hydronium and hydroxyl ions.

To address this, we observe here that $\Omega^{(ni)}$ for water can *also* be brought into a "convolution form" by making use of the following mathematical identity, which

is readily derived using the addition theorem for spherical harmonics,

$$\delta(\hat{\mathbf{v}}\cdot\hat{\mathbf{w}}-\cos\zeta)=\sum_{lm}2\pi P_l(\cos\zeta)Y^*_{lm}(\hat{\mathbf{v}})Y_{lm}(\hat{\mathbf{w}}), \tag{3.5}$$

where $\hat{\mathbf{v}}$ and $\hat{\mathbf{w}}$ are unit vectors, ζ is an arbitrary angle, P_l is a Legendre polynomial and the Y_{lm}'s denote the spherical harmonics. (To prove (3.5), first expand the delta function as a sum of pairs of Legendre polynomials on the interval $[-1;1]$ and then use the spherical-harmonic "addition theorem" to express $P_l(\hat{\mathbf{v}}\cdot\hat{\mathbf{w}})$ as a sum of pairs of spherical harmonics.)

Substituting (3.5) and (3.4) into (2.1) results in a computationally efficient form for the non-interacting free energy $\Omega^{(ni)}$,

$$\begin{aligned}\Omega^{(ni)} &= -k_BTn_l\int_V d\boldsymbol{r}_0 e^{-\beta\Psi_0(\mathbf{r}_0)}\\ &\times\sum_{lm}4\pi P_l(\cos\theta_B)f^{(1)}_{lm}(\mathbf{r}_0)f^{(2)}_{lm}(\mathbf{r}_0),\end{aligned} \tag{3.6}$$

where $f^{(1)}_{lm}$ and $f^{(2)}_{lm}$, given by

$$\begin{aligned}f^{(1)}_{lm}(\mathbf{r}_0) &= \int_V d\boldsymbol{r}_1\frac{\delta(|\mathbf{r}_1-\mathbf{r}_0|-B)}{4\pi B^2}Y^*_{lm}(\hat{\mathbf{r}}_{10})e^{-\beta\Psi_1(\mathbf{r}_1)}\\ f^{(2)}_{lm}(\mathbf{r}_0) &= \int_V d\boldsymbol{r}_2\frac{\delta(|\mathbf{r}_2-\mathbf{r}_0|-B)}{4\pi B^2}Y_{lm}(\hat{\mathbf{r}}_{20})e^{-\beta\Psi_2(\mathbf{r}_2)},\end{aligned} \tag{3.7}$$

are now convolutions and can be efficiently evaluated with fast-Fourier-transform techniques. Transformation to Fourier space greatly simplifies the above convolutions,

$$\begin{aligned}f^{(1)}_{lm}(\mathbf{k}) &= (-i)^l j_l(|\mathbf{k}|B)Y^*_{lm}(\hat{\mathbf{k}})\mathcal{F}[e^{-\beta\Psi_1(\mathbf{r})}]\\ f^{(2)}_{lm}(\mathbf{k}) &= (-i)^l j_l(|\mathbf{k}|B)Y_{lm}(\hat{\mathbf{k}})\mathcal{F}[e^{-\beta\Psi_2(\mathbf{r})}],\end{aligned} \tag{3.8}$$

where j_l denotes the spherical Bessel functions of the first kind and $\mathcal{F}[\exp(-\beta\Psi_1(\mathbf{r}))]$ denotes the Fourier transform of $\exp(-\beta\Psi_1(\mathbf{r}))$.

To evaluate (3.6) numerically, we first choose a maximum value of l, l_{max}, after which we truncate the infinite sum. In general, the choice of l_{max} depends on the density profile that has to be represented. We find in the capacitor calculation presented below that the interaction site densities for water adjacent to the capacitor wall are fairly smooth in the linear response regime and can be sufficiently resolved with $l_{max} = 10$. If strong external fields are applied, sharp features in the density profile develop and we use $l_{max} = 40$ to be absolutely sure of a highly converged description.

3.4 Intermolecular free energy

In this section, we determine the various contributions to the internal energy functional U, defined in (3.2).

First, we determine the excess free energy functional F^{ex}. For this purpose, we approximate the excess free energy per unit volume $f^{ex}(n)$ of the homogeneous phase as a sixth-order polynomial,

$$f^{ex}(n) = \sum_{p=0}^{6} f_p n^p, \tag{3.9}$$

and adjust its coefficients to reproduce the seven conditions represented by (a) the thermodynamic stability of liquid and vapor phases, (b) their coexistence, (c) the experimental liquid and vapor densities, (d) the experimental bulk modulus of the liquid (B_l) and (e) the derivative of the bulk modulus with respect to the pressure P at standard temperature and pressure ($T = 25$ °C and $P = 101.325$ kPa $\equiv 1$ atm). Table 3.1 summarizes the experimental input used to determine the coefficients f_p, and Table 3.2 gives the actual numerical values of the coefficients used in our calculations below. (Clearly, not all of the digits given in the table are significant,

we give them only to make our results numerically reproducible.) The values in the table are given in atomic units (1 hartree $\approx$ 27.21 eV) as this is the system which our software employs.

Next, we can determine the coefficients in the integrand in (2.6) from knowledge of the constant term in the long-wavelength expansion of the Hessian $\partial^2_{\mathbf{n}} U$. The entries in this term (which is a matrix) are related to various material response properties such as as the bulk modulus, but unfortunately, we do not have access to data for all of the material properties. In the absence of data, we take this matrix to be proportional to its value for the non-interacting case with a proportionality constant set to ensure the correct bulk modulus. This then fixes the integrand in (2.6) and allows it to be written entirely in terms of rational numbers in the form,

$$-\frac{19}{20} f^{ex}(\overline{n}_0) + \frac{3}{10} f^{ex}(\overline{n}_1) + \frac{3}{10} f^{ex}(\overline{n}_2) + \frac{27}{20} f^{ex}\left(\frac{\overline{n}_0 + \overline{n}_1 + \overline{n}_2}{3}\right). \tag{3.10}$$

Next, to construct the matrix K, which as described in Section 3.2, captures the long wavelength correlation functions entirely in terms of the dielectric constant of water, we use the partial charges of the SPC/E water model [15], i.e. $q_1 = q_2 = -q_0/2 = 0.4238\, e$ (e being the proton charge) and the fact that the dielectric constant of the liquid with intra-molecular correlations *only* is $\epsilon^{(ni)} = (1 - 4\pi\beta n_l p^2/3)^{-1}$, where p is the dipole moment of an SPC/E water molecule. Also, we employ the experimental value [16], $\epsilon = 78.4$, for the macroscopic dielectric function of liquid water at standard conditions described above.

The use of K as leading order term is only justified for *long-wavelength* (small $\mathbf{k}$) properties of the liquid: we therefore cut off its slowly decaying, large $\mathbf{k}$ tail by

Table 3.1: Experimental inputs[16, 17] to construction of f^{ex}: liquid density (ρ_l), vapor density (ρ_v), liquid bulk modulus (B_l) and derivative of modulus with respect to pressure ($\partial B_l/\partial P$). We also impose the thermodynamic stability of liquid and vapor phases and their coexistence.

ρ_l [kg/m^3]	ρ_v [kg/m^3]	B_l [GPa]	$\partial B_l/\partial P$ (dimensionless)
997.1	0.023	2.187	5.8

Table 3.2: Coefficients of polynomial parametrization of f^{ex} given to all digits used in our software in order to ensure numerical reproducibility of our results. Any individual coefficient contains at most two or three significant figures.

f_0	[hartree $\times$ bohr^{-3}]	$3.8392\ 9979\ 1272\ 76 \times 10^{-18}$
f_1	[hartree]	$-1.0112\ 4264\ 5511\ 99 \times 10^{-10}$
f_2	[hartree $\times$ bohr^{3}]	$8.8785\ 7550\ 4400\ 45 \times 10^{-4}$
f_3	[hartree $\times$ bohr^{6}]	$-2.5985\ 6289\ 5737\ 31 \times 10^{3}$
f_4	[hartree $\times$ bohr^{9}]	$9.1718\ 3837\ 1076\ 96 \times 10^{5}$
f_5	[hartree $\times$ bohr^{12}]	$-1.2707\ 9357\ 3856\ 54 \times 10^{8}$
f_6	[hartree $\times$ bohr^{15}]	$6.5872\ 0860\ 4647\ 96 \times 10^{9}$

multiplying it in Fourier space with a crossover function λ_{cr} given by

$$\lambda_{cr}(\mathbf{k}) = \frac{1}{(1 + |\mathbf{k}|/k_c)^4}, \tag{3.11}$$

with $k_c = 0.33$ bohr, chosen to keep the C functions as band-width limited as possible. The functional form for λ_{cr} was chosen purely for numerical convenience and allowed for an accurate fitting of the experimental correlation function data.

Then we determine C, which as described in Section 3.2 captures the hydrogen-bonded structure of the liquid, using the partial structure factor data for the uniform liquid as measured by Soper[18] (Figure 1 in that reference). The best, explicit partial structure factor data which we have found are measured at standard pressure, but at a temperature $T = 20 \pm 3$ °C, which differs slightly from the standard temperature ($T = 25$ °C) employed in this work. Comparing experimental radial distribution functions at various temperatures [19], we find that the differences remain smaller than 10% over a temperature range of 30 Kelvin. We therefore expect an overall error of no more than one or two percent due to this difference in temperatures. Next, adjusting the smoothing parameter in (3.3) to give the experimental surface tension of 71.98×10^{-5} N/m[16], measured at standard conditions, yields $r_0 = 4.2027$ bohr (to all the digits used in our software). Interestingly, we find r_0 to be comparable to the size of the water molecule, a microscopic quantity, although it was obtained by fitting to the surface tension, a macroscopic quantity. Thus, our choice of weighting procedure is very similar to the approach of Yethiraj and coworkers[20], who employ a Heaviside step function, which averages over a spherical region with a radius equal to the atomic diameter. Finally, to provide a computationally transferable representation of C, we parametrize each component $C_{\alpha\gamma}$ by a sum of Gaussians in Fourier space

$$C_{\alpha\gamma}(\mathbf{k}) = \sum_{i=1}^{N_{\alpha\gamma}} A_{\alpha\gamma}^{(i)} \exp\left\{-B_{\alpha\gamma}^{(i)} \left(|\mathbf{k}| - C_{\alpha\gamma}^{(i)}\right)^2\right\}. \tag{3.12}$$

Table 3.3 summarizes the resulting fitting coefficients (to all decimal places used in our software). To reproduce the full matrix, note that C is symmetric and that the identity of the hydrogens imposes $C_{11} = C_{22}$. Figure 3.1 compares our extracted C functions to the resulting numerical fits, the latter of which are used in all of the calculations presented below.

3.5 Recipe for evaluating the free energy functional for water

In sum, to compute the free-energy functional for a given set of effective potentials $\Psi_\alpha(\mathbf{r})$ (which, for example, could come from an *ab initio* calculation of a solute), one first evaluates the intra-molecular contribution via (3.6)) and (3.8). Next, one determines the site densities, which allows one to evaluate the second term in (2.3) trivially. Finally, one evaluates the last term in (2.3) according to (2.5), with K given by (2.4), C parameterized by the coefficients in Table 3.3, and F^{ex} computed according to (2.6), (3.9), (3.10).

3.6 Water in a parallel plate capacitor

To demonstrate the ability of our density-functional theory to describe water in an inhomogeneous environment and to capture the dielectric response of the liquid, we study the behavior of the liquid in a parallel plate capacitor. We carry out our study at the standard temperature and pressure described above, taking the system to be homogeneous in the two dimensions parallel to the capacitor plates. Along the perpendicular direction, we impose periodic boundary condi-

Table 3.3: Coefficients of Gaussian parametrized C functions. Note that, by symmetry, $C_{\alpha\gamma} = C_{\gamma\alpha}$ and $C_{11} = C_{22}$. (C_{12} and C_{11} turned out to be numerically indistinguishable.) Coefficients are given to all digits used in our software to ensure numerical reproducibility of our results. The index 0 refers to the oxygen site, the indices 1 and 2 refer to the two hydrogen sites.

	i	$A^{(i)}_{\alpha\gamma}$ [hartree]	$B^{(i)}_{\alpha\gamma}$ [bohr^2]	$C^{(i)}_{\alpha\gamma}$ [bohr^{-1}]
C_{00}	1	−0.0271 1530	1.0569 0000	0.0204 8180
	2	−0.0795 5700	1.6385 3000	0.1295 1300
	3	0.0966 4800	1.8781 5000	0.0736 7760
	4	−0.0291 5170	2.4678 7000	0.0563 6360
	5	0.0227 0520	3.1004 7000	0.0844 1320
	6	−0.0109 0780	3.7162 0000	0.0452 0230
C_{01}	1	−0.0080 1259	1.1985 9000	0.0280 2800
	2	0.0379 8360	1.7289 7000	0.1175 3400
	3	−0.0380 7370	2.1583 9000	0.2133 3600
	4	0.0254 5760	2.7211 2000	0.1541 5700
	5	−0.0029 1329	3.2989 4000	0.0265 2820
	6	0.0010 9967	3.7659 0000	0.0315 5180
C_{11}	1	−0.0139 5900	1.8869 7000	0.1041 8600
	2	0.0295 7760	2.5316 4000	0.0869 8480
C_{12}	1	−0.0139 5900	1.8869 7000	0.1041 8600
	2	0.0295 7760	2.5316 4000	0.0869 8480

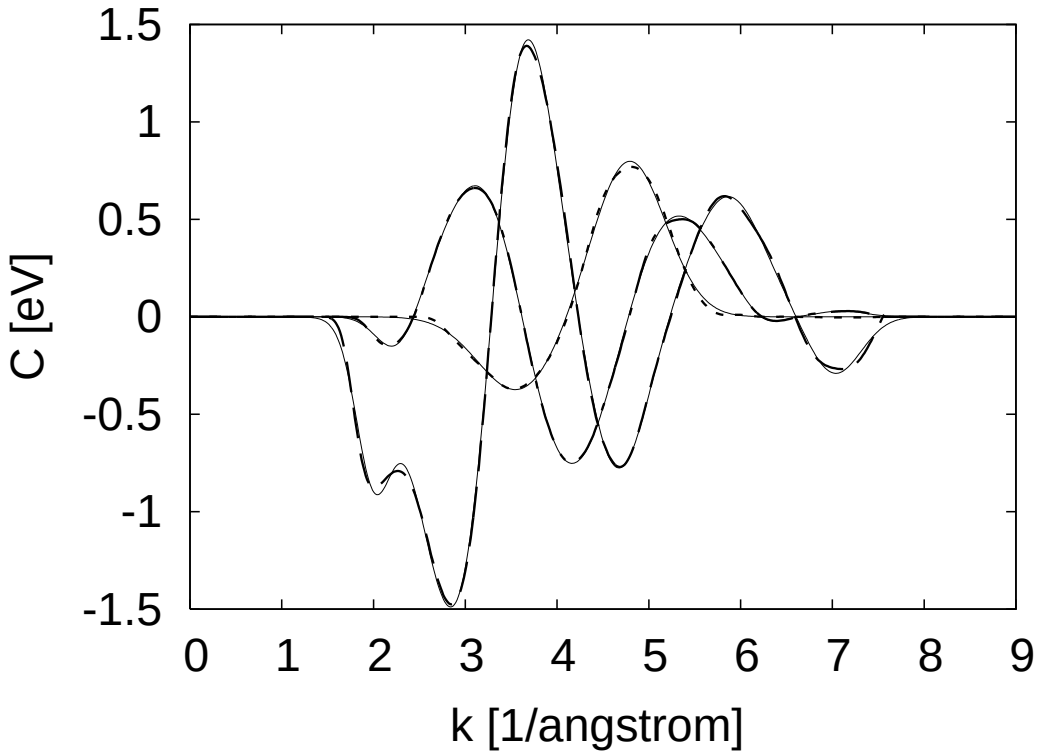

Figure 3.1: Comparison of C_{00} (thick dashed curve), C_{01} (thick dash-dotted curve) and C_{11} (thick dotted curve) and the corresponding parametrized forms (thin solid curves) given by (3.12) and Table 3.3. Note that C_{12} is not shown, since it would be visually indistinguishable from C_{11}.

tions, defining a unit cell containing *two* parallel plate capacitors with opposing externally applied electric fields. This arrangement makes the electrostatic potential a periodic function and eliminates undesired electrostatic interactions between the capacitors. Each capacitor has a plate separation of 200 bohr and the total length of the cell is 800 bohr.

In our study we consider both purely repulsive, "hard-wall" plates as well as "attractive" plates with a region of attraction near the plates. For the hard-wall case, the plates are essentially infinite potential hard walls acting on both the oxygen and hydrogen sites of the water molecules. As a practical numerical matter, to reduce aliasing effects in the use of the numerical Fourier transform we approximate such walls by purely repulsive Gaussian potentials of sufficiently narrow width and large amplitude so that the results below are insensitive to the width and amplitude of the Gaussian employed. In particular, we use

$$\phi_{hw}(z) = A \exp\left(-\frac{z^2}{2a^2}\right), \tag{3.13}$$

with $A = 150\ k_B T$ and $a = 0.5$ Å. For the attractive case, we employ a "9-3" (planarly integrated Lennard-Jones) potential acting on the oxygens *only*, specifically,

$$\phi_{at}(z) = C\left[\left(\frac{D}{z + z_{\text{shift}}}\right)^9 - \left(\frac{D}{z + z_{\text{shift}}}\right)^3\right] \tag{3.14}$$

with $C = 9 \times 0.15/(2\sqrt{3})$ eV, $D = \frac{5}{3^{1/6}}$ Å and $z_{\text{shift}} = 3.78$ Å. This potential has its minimum at a distance of 3 Å from the wall at a depth 0.15 eV. We choose this depth as typical of the interaction between metallic surfaces and their aqueous environment. For instance, Berkowitz and co-workers [21] employ a corrugated potential with an average depth of about 0.40 eV, which is also in the range of a couple of tenths of an electron Volt, to describe the interaction of water with a platinum surface. We note that the attractive term of the "9-3" potential describes

the van der Waals attraction between water molecules and the particles comprising the wall.

To determine the thermodynamic state of the system we then expand the density fields on a real space grid with 8192 sampling points ($\sim$ 20 points/Å), and minimize the grand free energy (2.3) using standard numerical conjugate gradient techniques without any preconditioning.

3.7 Results

3.7.1 Hard-wall plates

We begin with a brief discussion of our results for the hard wall case as an idealized reference for comparison. Figure 3.2 shows our results for oxygen and hydrogen equilibrium density profiles in the absence of an externally applied electrostatic displacement ($D = 0$) and compares them to the density profiles of hydrogen and oxygen sites in a relatively weak external field ($\alpha \equiv \beta p D/\epsilon \approx 0.009$). The zero-field profiles exhibit an extended gas phase region up to a distance of ~ 10 Å from the plates. This "lingering" gas phase region exists because molecules can, at very little free-energy cost, minimize the influence of the repulsive plates by leaving the system. (Recall that (2.3) is written in the grand canonical ensemble, so that the system can exchange particles with an external reservoir.) As soon as a relatively weak external electric displacement is applied, however, it becomes favorable for the dipolar molecules to enter the system because they can lower their energy by partially aligning with the field within the capacitor. For even quite small fields, this effect causes the capacitor to fill with liquid, thereby eliminating most of the

gas phase region. The result of this is then an almost rigid shift of the density profiles toward the capacitor plates, with an appearance and general shape which remains nearly fixed over a large range of fields. Figure 3.2 shows that the liquid approaches the wall up to a distance of approximately 1.7 Å corresponding to the distance where the ϕ_{hw} is smaller than 5 $k_B T$.

We note that the observed layering of the liquid adjacent to a solid interface has also been found for hard sphere liquids [22].

Considering the fine details of the density profiles, we note that, contrary to our previous results for diatomic liquids, a relatively small (barely noticeable in the figure) asymmetry exists at zero external field between the oxygen and hydrogen site densities so that there is a non-vanishing electrostatic charge density in the vicinity of the capacitor plates — even in the absence of an externally applied electric field. (Note: because the oxygen site carries a charge which is double in magnitude compared to the hydrogen site and because there are two independent but identical hydrogen sites, the magnitude of the charges carried by the oxygen and hydrogen density fields are directly proportional to the curves in the figure, *with the same constant of proportionality* for each.) By symmetry, the net charge which the plates induce must integrate to zero; however, a finite surface dipole remains with a corresponding potential jump which we find in the zero-field hard-wall case to be +0.041 V across the solid-liquid interface, with the potential being higher in the solid.

Figure 3.3 shows the equilibrium density profiles in a relatively strong ($\alpha = \beta p D/\epsilon \approx 0.25$) external field directed from left to right in the figure. The relative abundance of oxygen sites close to the left plate (which carries a positive external charge to generate the field) and of hydrogen sites next to the right plate (which

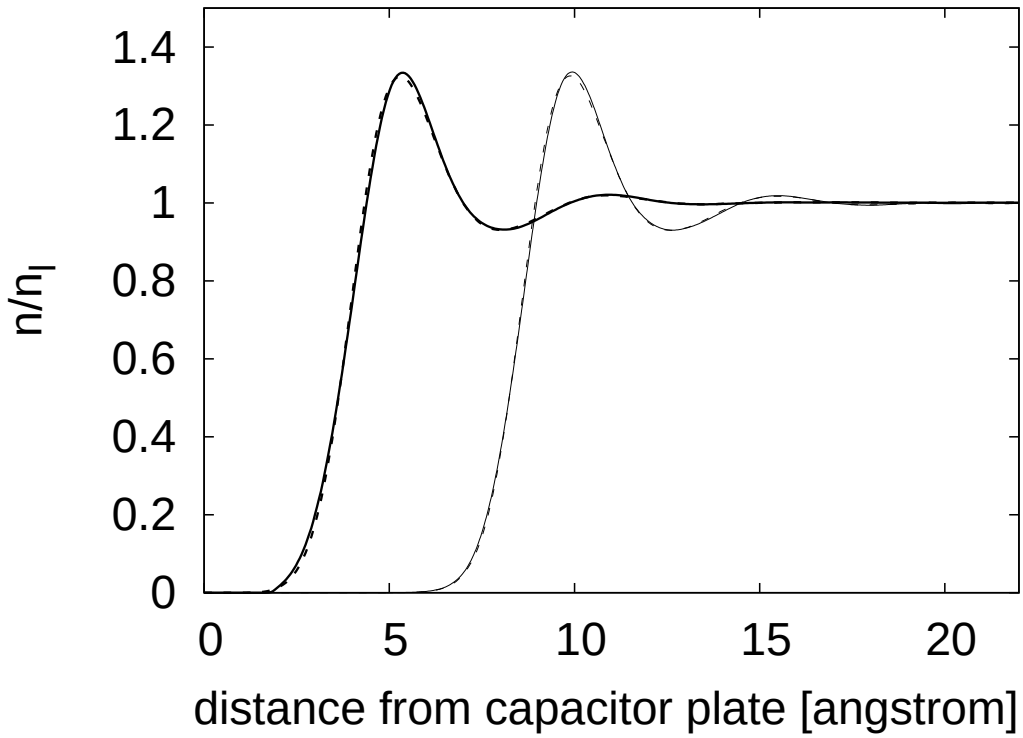

Figure 3.2: Hydrogen- (thick dotted curve) and oxygen- (thick solid curve) site density in weak field and zero field (thin curves) versus distance from hard-wall plate. Note that the hydrogen and oxygen densities are nearly visually indistinguishable. We point out that following the practice in the literature we only plot the density of *one* of the two hydrogen sites. Of course, to obtain the total hydrogen density one has to scale the given density profile by a factor of 2.

carries a negative external charge) indicates that the water molecules exhibit a strong tendency to align their dipoles with the applied field. Interestingly, this leads to quite different density profiles on the opposite sides of the capacitor. On the left (positive) plate, the first peak in the oxygen density is followed by a peak in the hydrogen density of similar shape, width and height. This we interpret to be a direct consequence of alignment of the molecules with the field and the rigid intra-molecular bonding between hydrogen and oxygen atoms, an effect quite similar to what was observed in our previous study of liquid hydrogen chloride[23]. The distance between these peaks, 0.65 Å, is within about 10% of 0.58 Å, what one expects from the basic geometry of the water molecule assuming that the molecules fully align with the field.

On the right (negative) plate, we again find a well-defined peak in the oxygen density, though the peak is somewhat stronger than on the left. We find also that the hydrogen density, rather than being also sharply peaked, is now spread significantly around the oxygen peak. This case is different, because the hydrogen sites, now pointing away from the liquid region, cannot form hydrogen bonds if the molecules align fully with the field.

3.7.2 Attractive plates

Figure 3.4 compares the zero-field results for the hard-wall plates with those of the attractive plates. There is no longer a "lingering" gas phase region because the minimum in the interaction potential (acting only on the oxygen sites in this case) with the plates sets the location of the main peak in the oxygen density. This minimum, as described above, occurs at a distance of about 3 Å from the attractive walls and corresponds well with the peaks in the oxygen and hydrogen

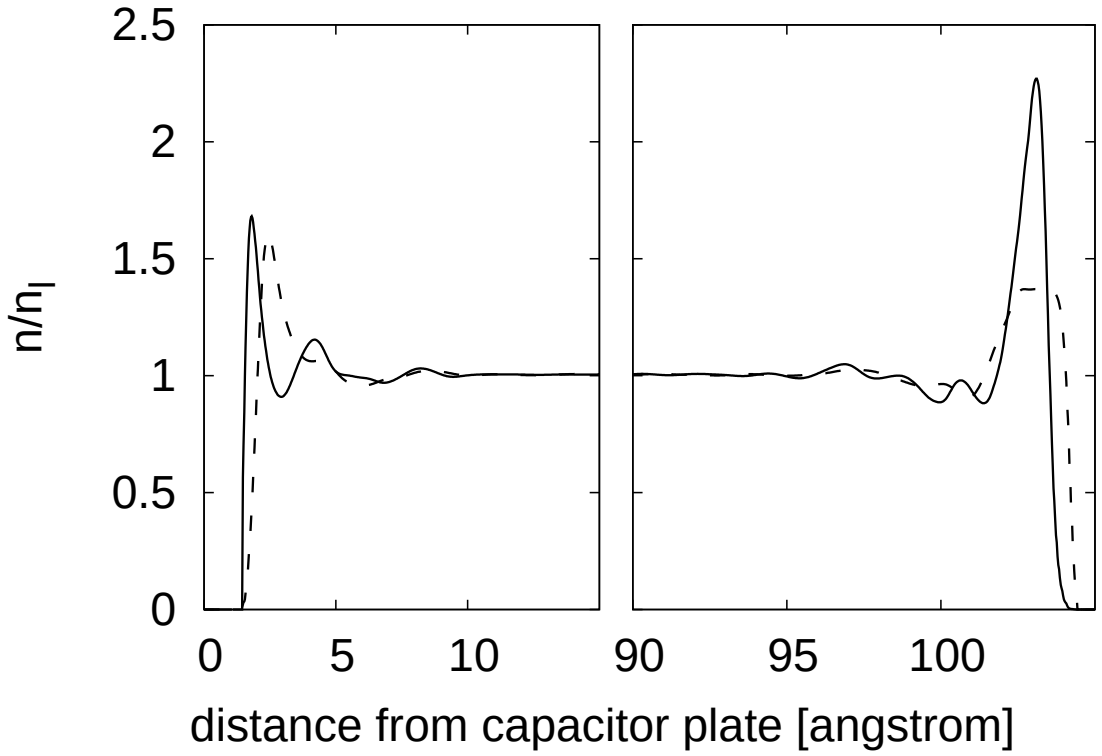

Figure 3.3: Hydrogen- (dashed curve) and oxygen- (solid curve) site density in strong field versus distance from hard-wall plate.

density profiles. The height of the oxygen peak is larger than the density in the bulk by a factor of ~ 4.7, which is similar to the results of molecular dynamics calculations of water adjacent to platinum surfaces [21], which neglected image effects at the metallic surface, and experimental findings [24]. Finally, there is also a net dipole layer in our attractive case leading now to a significantly stronger potential jump at the liquid-solid interface of +0.220 V, with the potential in the solid again being higher. This value is typical of realistic systems: from molecular dynamics data of water adjacent to a platinum surface[25], we extract a potential jump of $\sim +0.5$ V with the potential being higher in the solid.

When a strong field (again, $\alpha \approx 0.25$) is applied to the capacitor with attractive walls (Figure 3.5), we find a rearrangement of the liquid structure which exhibits various quantitative differences compared to the hard-wall case: the oxygen peaks are now significantly more pronounced (reaching values near 4 and 5 times the equilibrium liquid density, as opposed to the previous peak values near 1.5 and 2.2) as the oxygen atoms settle into the attractive potential wells near the walls. Also, the peak near the positive plate is also now notably broader (with a width of 1.6 Å at the value of the equilibrium, as opposed to the previous value of 1.0 Å). Finally, the hydrogen peak is significantly less pronounced relative to the oxygen peak and the peak position is now less displaced (0.4 Å) from the oxygen peak position. Despite these quantitative differences, however, the qualitative features at strong fields are quite similar in the attractive and the hard-wall cases. Namely, on the left (positive) plate we find a well-defined peak in the oxygen density followed by a corresponding peak in the hydrogen density, and on the right (negative) plate there is a well-defined oxygen peak which is surrounded by a more diffuse peak in the hydrogen density. Also, as with the hard wall case, we find that the hydrogen peak is off-center from the oxygen peak and displaced toward

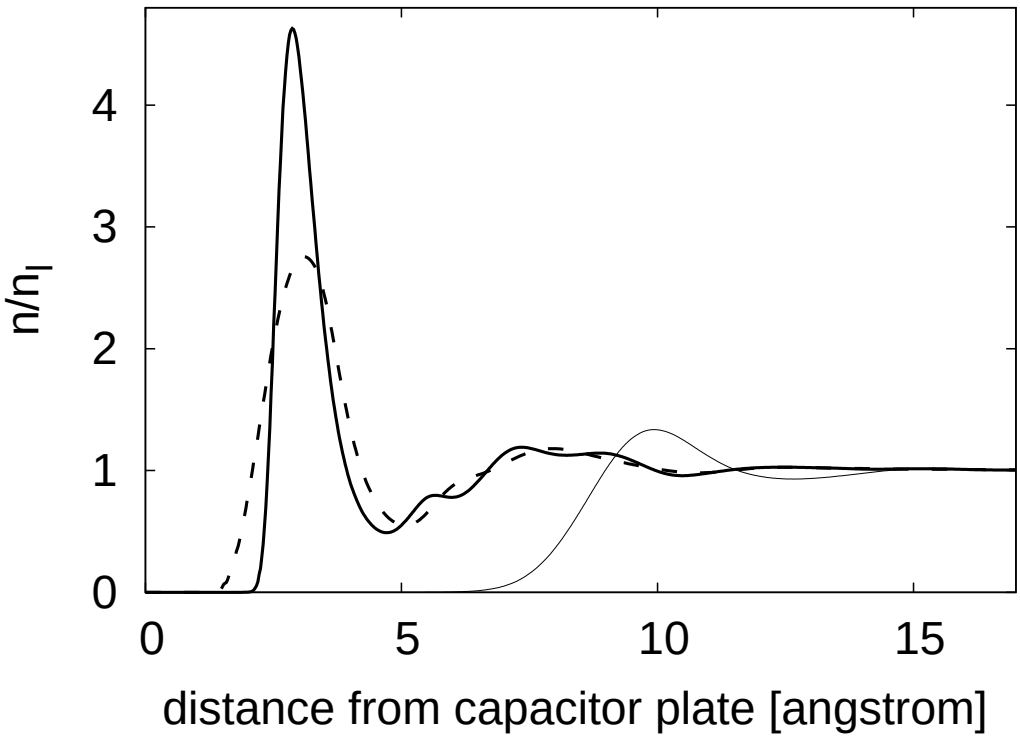

Figure 3.4: Hydrogen- (thick dashed curve) and oxygen- (thick solid curve) site density in strong field versus distance from attractive wall. Reference result for the zero field oxygen density at repulsive wall (thin solid curve).

the negative plate to which it is attracted.

This suggests that, at these large field strengths, general features are independent of the exact form of the liquid-solid interaction. In fact, we note that this sort of asymmetry between positive and negative plates is also evident in molecular dynamics calculations which, at fields near $\alpha = 0.25$, also tend to show that, near the positive plate, the oxygen density exhibits peaks which are followed by peaks of similar appearance in the hydrogen density, whereas, near the negative plate, there is a well-defined peak in the oxygen density but the hydrogen density exhibits either a broader peak or multiple sub-peaks in the vicinity of the main oxygen peak[25, 26].

3.7.3 Nonlinear dielectric response

The equilibrium site densities also determine the dielectric function of water $\epsilon(D) = D/E(D)$ with E being the total electric field given by the sum of the electric displacement and the induced electric field. Although E has a complicated form close to the walls, it rapidly approaches the constant value $E = D - 4\pi P$ as the distance from the walls increases, where P is the induced polarization. In the present one-dimensional geometry, P is proportional to the induced surface charge which appears in the equilibrium density profiles.

Figure 3.6 shows our calculated results for ϵ plotted as a function of E in units of MV/m (equivalent to 1 mV/nm or 0.1 mV/Å) to simplify comparison with the results of previous studies. The figure shows that the results from our density-functional theory are well-described by self-consistently screened nonlinear electrostatics (solid curve), which gives the polarization P as the self-consistent

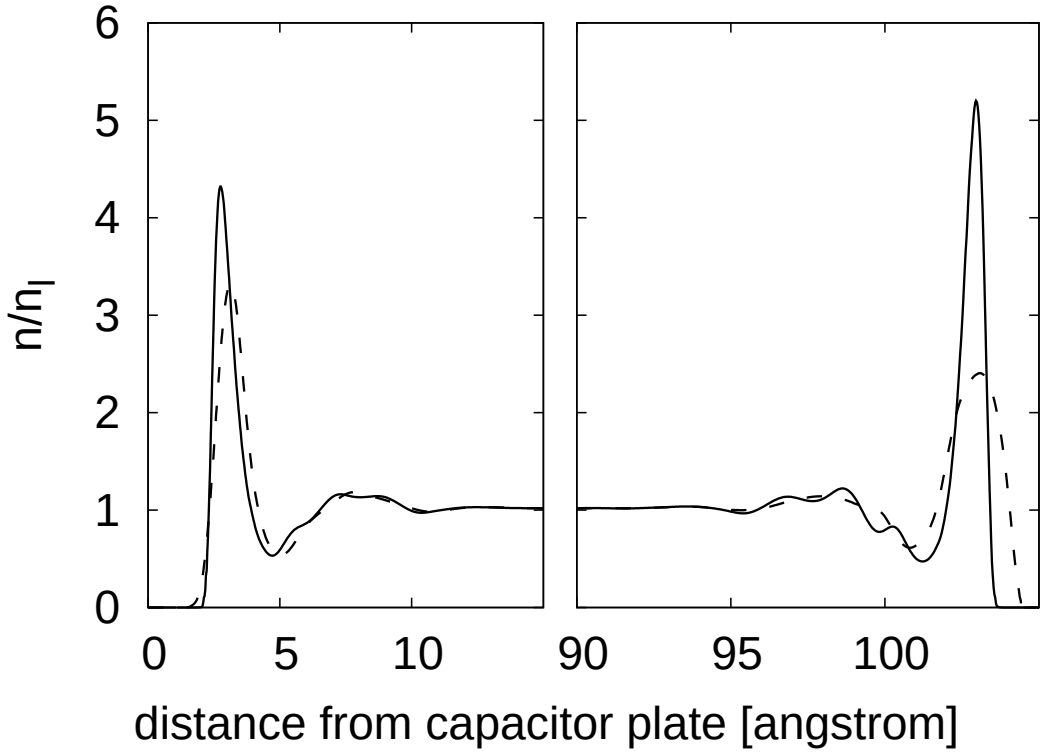

Figure 3.5: Hydrogen- (dashed curve) and oxygen- (solid curve) site density in strong field versus distance from attractive wall.

solution to the equation $P = P^{(ni)}(D - a_\epsilon 4\pi P)$, where $P^{(ni)}(E)$ is the response of a gas of noninteracting dipoles in a local field E and $a_\epsilon \equiv \epsilon/(\epsilon-1) - \epsilon^{(ni)}/(\epsilon^{(ni)}-1)$ ensures that the correct linear response is recovered when D is weak. The solid curve reproduces our data well and so represents a convenient analytic guide to the eye for our results.

Figure 3.6 compares our results to Booth's analytical result for the nonlinear dielectric response of water [27]. This result (dashed curve in the figure) was obtained by extending Onsager's and Kirkwood's theories of polar dielectrics to high field strengths [27] and also reproduces quite well explicit molecular dynamics results for high fields. It fails, however, at small fields, eventually giving an incorrect linear dielectric constant of about ~ 65. We find very good agreement with this established result for fields larger than 300 MV/m. We also compare our results to various molecular dynamics calculations [25, 28, 29] and find very good agreement, except at zero field, where the results of the molecular dynamics calculations often show a wide range of results, some differing significantly from the experimental dielectric constant of ~ 80 depending on the model potentials and numerical methods employed[30]. The zero-field dielectric constant, we, of course, reproduce exactly by construction. Our results, therefore, appear to be reliable over a broad range of applied fields.

3.8 Summary and conclusions

This work demonstrates how to apply the general multi-site density-functional theory of molecular liquids to what is arguably the liquid of greatest scientific interest, water. The resulting theory has the quite tractable computational cost

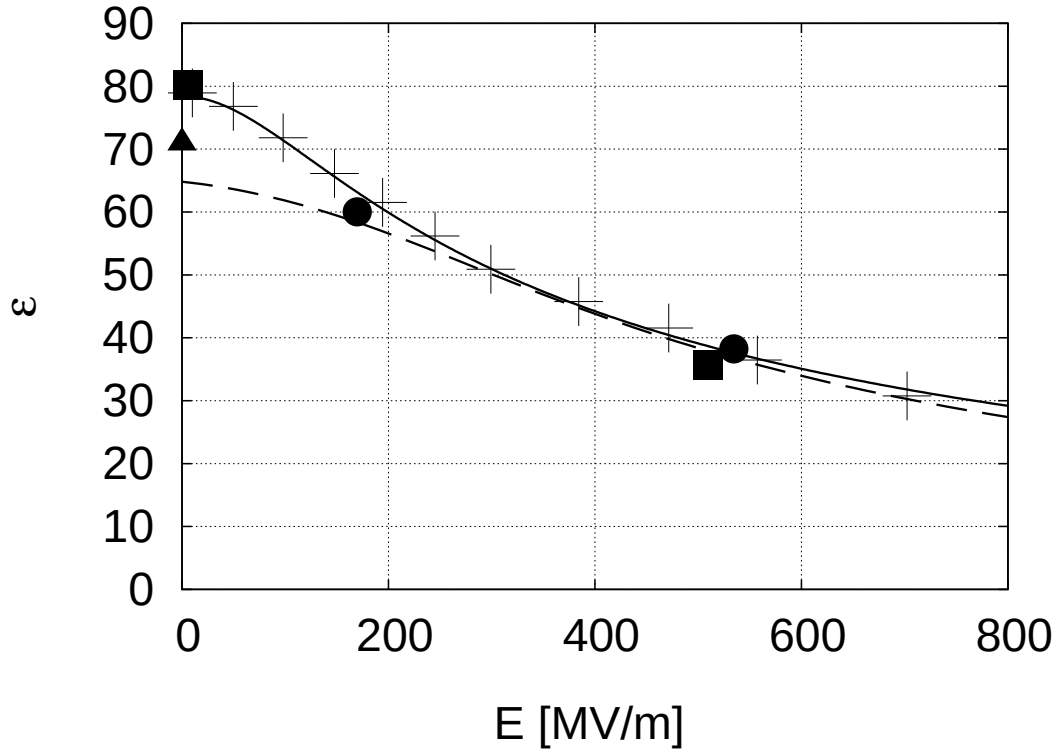

Figure 3.6: Dielectric function versus total field: density-functional results (crosses), non-linear electrostatics (solid curve), analytical result of Booth[27](dashed line), molecular dynamics results of Yeh and Berkowitz[25](circles), Sutmann[28](squares) and Svishchev and Kusalik[29](triangles).

of the problem of a noninteracting gas of molecules in a self-consistent external potential and gives an exact account of the dielectric properties of liquid water.

After constructing the functional and giving a complete numerical parameterization of all quantities so that our results are numerically reproducible, we demonstrate the tractability of the approach by applying it to the behavior of water in parallel plate capacitors, with either hard-wall or attractive plates, over a range of applied fields through which the dielectric constant ϵ of water varies by over a factor of two. We provide results for the distribution of oxygen and hydrogen atoms near the capacitor plates and find an asymmetry between the response at negatively and positively charged plates in general qualitative agreement with molecular dynamics results. From the resulting charge distributions, we extract predictions of the dielectric constant of water over a wide range of field strengths (0 to 800 MV/m) and find results in very good agreement with both previous analytical calculations using the Onsager theory and molecular dynamics calculations. The aforementioned exact treatment of the entropy cost of aligning the molecules with the field is critical in producing this accurate treatment of dielectric saturation effects.

With a successful framework in place, there is now a firm basis for future improvements. Given that we now have a good treatment of the internal structure of the water molecule and the dielectric response of the liquid, the primary area remaining for improvement is our choice to employ for this first work a somewhat simplistic weighted-density functional form in (2.6). The direct route to improve upon this is to leverage much of the existent work in simple fluids, both in traditional weighted density-functional theories[31] and in fundamental measure theory[32]. Another clear area in which to build would be the inclusion of addi-

tional, ionic species into the functional to allow for screening by electrolytes, which should be relatively straightforward.

Another area for possible improvement is the dependence on experimental input in the construction of the free energy functional. To study the variation of physical quantities with temperature, one currently needs to construct a new functional for each temperature using experimental correlation function data taken at that particular temperature. A possible solution would be to employ correlation function data from *ab initio* molecular dynamics calculations of homogeneous systems. This would allow us to study the specific heat of water, the temperature dependence of the density profiles at solid interfaces or the freezing of water.

In sum, we present a computationally tractable continuum description of water which captures, within a unified approach with a firm theoretical foundation, molecular-scale correlations, entropic effects, microscopic dielectric screening, surface tension, bulk thermodynamic properties, and dielectric saturation. This description thus includes *a priori* all of the various effects which are generally added *a posteriori* to continuum models of water. Although less detailed than current explicit molecular treatments of the solvent, freed from the need for computing thermodynamic averages, a sufficiently accurate continuum approach such as we present has the potential to open up much larger and complex systems to theoretical study. As such, the presented framework is an ideal starting point for a variety of new investigations into a wide class of subjects, which include protein folding, molecular motors, membrane physics, drug design, the electrochemical interface, liquid-phase catalysis and fuel cells.

BIBLIOGRAPHY

[1] D. Chandler. *Nature*, 437:640, 2005. 40

[2] H.S. Ashbaugh and L.R. Pratt. *Rev. Mod. Phys.*, 78:159, 2006. 40

[3] P. Liu, X. Huang, R. Zhou, and B.J. Berne. *Nature*, 437:159, 2005. 40

[4] M. Tarek and D.J. Tobias. *Phys. Rev. Lett.*, 88:138101, 2002. 40

[5] T.Tansel and O.M. Magnussen. *Phys. Rev. Lett.*, 96:026101, 2006. 40

[6] G. Hummer, J.C. Rasaiah, and J.P. Noworyta. *Nature*, 414:188, 2001. 40

[7] Y. Leng and P.T. Cummings. *Phys. Rev. Lett.*, 94:026101, 2005. 40

[8] J.-P. Hansen and I.R. McDonald. *Theory of Simple Liquids*. Academic Press, London, 2006. 41

[9] K. Ding, D. Chandler, S.J. Smithline, and A.D.J. Haymet. *Phys. Rev. Lett.*, 59:1698, 1987. 41

[10] G. Reddy, C.P. Lawrence, J.L. Skinner, and A. Yethiraj. *J. Chem. Phys.*, 119: 13012, 2003. 41, 42

[11] J.-K. Hyun and T. Ichiye. *J. Chem. Phys.*, 109:1074, 1998. 42

[12] J.D. McCoy, S.J. Singer, and D. Chandler. *J. Chem. Phys.*, 87:4853, 1987. 43

[13] C.E. Woodward. *J. Chem. Phys.*, 94:3183, 1990. 43

[14] J. Forsman and C.E. Woodward. *Macromol.*, 39:1261, 2006. 43

[15] H.J.C. Berendsen, J.R. Grigera, and T.P. Straatsma. *J. Phys. Chem.*, 91: 6269, 1987. 45, 48

[16] D.R. Lide, editor. *Handbook of Chemistry and Physics*. CRC Press, Inc., 1995. 48, 49, 51

[17] E. Wilhelm. *J. Chem. Phys.*, 63:3379, 1975. 49

[18] A.K. Soper. *J. Chem. Phys.*, 101:6888, 1994. 51

[19] A.K. Soper. *Chem. Phys.*, 258:121, 2000. 51

[20] A. Yethiraj, H. Fynewever, and C.-Y. Shew. *J. Chem. Phys.*, 114:4323, 2001. 51

[21] K. Raghavan, K. Foster, K. Motakabbir, and M. Berkowitz. *J. Chem. Phys.*, 94:2110, 1991. 55, 61

[22] Y.-X. Yu and J. Wu. *J. Chem. Phys.*, 117:10156, 2002. 57

[23] J. Lischner and T.A. Arias. *Phys. Rev. Lett.*, 101:216401, 2008. 59

[24] M.F. Toney, J.N. Howard, J. Richer, G.L. Borges, J.G. Gordon, O.R Melroy, D.G. Wiesler, D. Yee, and L.B. Sorensen. *Nature*, 368:444, 1994. 61

[25] I.-C.Yeh and M.L. Berkowitz. *J. Chem. Phys.*, 110:7935, 1999. 61, 63, 65, 66

[26] X. Xia and M.L. Berkowitz. *Phys. Rev. Lett.*, 74:3193–3196, 1995. 63

[27] F. Booth. *J. Chem. Phys.*, 19:391, 1951. 65, 66

[28] G. Sutmann. *J. Electroanal. Chem.*, 450:289, 1998. 65, 66

[29] I.M. Svishchev and P.G. Kusalik. *J. Phys. Chem.*, 98:728, 1994. 65, 66

[30] P.G. Kusalik and I.M. Svishchev. *Science*, 265:1219, 1994. 65

[31] W.A. Curtin and N.W. Ashcroft. *Phys. Rev. A*, 32:2909, 1985. 67

[32] Y. Rosenfeld. *Phys. Rev. Lett.*, 63:980–983, 1989. 67

CHAPTER 4

A JOINT TIME-DEPENDENT DENSITY-FUNCTIONAL THEORY FOR EXCITED STATES OF SOLVATED MOLECULES

In this chapter, we present a novel joint time-dependent density-functional theory for the description of solute-solvent systems in time-dependent external potentials. Starting out with the exact quantum-mechanical action functional including both electrons and nuclei, we eliminate solvent degrees of freedom and thus arrive at coarse grained action functionals, which retain the highly accurate *ab initio* description for the solute electrons while treating the solvent with an approximate time-dependent continuum theory. This procedure allows us to examine approximations underlying popular embedding theories for excited states. Finally, we introduce a novel action functional for the solute-water system and compute solvato-chromic shifts for formaldehyde in aqueous solution, which are in good agreement with experimental findings.

4.1 Introduction

Electronic excited states are important in many areas of physics, chemistry and biology. They are probed in spectroscopic experiments, such as absorption, reflectivity or photoluminescence measurements. In addition, they are important in many technical applications, such as photovoltaics [1, 2], laser technology [3] or light-emitting diodes[4–6].

Various methods for the theoretical modelling of electronic excited states have been developed. While highly accurate quantum chemistry methods, such as configuration interaction [7] or coupled cluster theory [8], are only applicable to rela-

tively small systems comprising very few electrons, in recent years time-dependent density-functional theory (TDDFT)[9, 10], which scales much more favorably with system size, emerged as an accurate theory for larger molecules and clusters [11–13]. However, despite its good scaling properties, the full TDDFT description is typically only applicable to systems in vacuum, while many experiments are carried out on dissolved molecules. To capture solvent effects on electronic excited states, a plethora of embedding approaches have been developed [14, 15]. In these methods, the solvent is either treated atomistically, for example via classical molecular dynamics [15], or a continuum description of the solvent is used [14]. Due to its simplicity, the latter approach has enjoyed great popularity. In particular, many calculations employed time-dependent density-functional theory in conjunction with the "polarizable continuum model" [14], where the molecule is placed inside a cavity inside a linear dielectric. The solute-solvent interactions are then separated into equilibrium and non-equilibrium contributions accounting for the fact that the electronic excitations on the molecule are screened by the high-frequency dielectric constant, which in many systems is much smaller than the static dielectric constant.

Despite the success of these continuum models, it is important to recall that their construction is purely phenomenological. To improve upon these theories and understand their limitations, it is important to understand their origin *from first principles*. In this chapter, we derive different levels of continuum embedding theory starting from the *exact* quantum-mechanical action functional [16] for the full solute-solvent system. We also introduce a novel dielectric continuum model, which takes into account the deviation from bulk behavior of the solvent response in the interfacial region and also retains the full frequency-dependence of the dielectric response. We apply this approach to study excitations of formaldehyde in aqueous

solution.

4.2 Joint time-dependent density-functional theory

In this section, we consider a system composed of an explicit subsystem or solute in contact with an environment or solvent. A typical example of such a system is a molecule dissolved in water.

Both solute and solvent consist of electrons and nuclei of different species. To determine the behavior of such a system in a time-dependent external potential, we employ time-dependent density-functional theory [9]. Generalizing the standard expression for the action of a single-component system at zero temperature [16] to multi-component systems at finite temperature yields the action functional S for the full solute-solvent system,

$$\begin{aligned} S[n,\{N_\alpha\}] &= A[n,\{N_\alpha\}] - \int_\Omega d\boldsymbol{r} \int_C d\tau n(\boldsymbol{r},\tau) v(\boldsymbol{r},\tau) \\ &- \sum_\alpha \int_\Omega d\boldsymbol{r} \int_C d\tau N_\alpha(\boldsymbol{r},\tau) V_\alpha(\boldsymbol{r},\tau), \end{aligned} \tag{4.1}$$

where Ω denotes an open volume as required when working in the grand canonical ensemble and τ denotes the Keldysh time [17], which is defined on the contour C ranging from 0 to ∞ and back on the real time axis and then from 0 to $-i\beta$ on the imaginary time axis with $\beta = 1/(k_B T)$ being the inverse thermal energy. Also, $n(\boldsymbol{r},\tau)$ and $N_\alpha(\boldsymbol{r},\tau)$ denote the quantum-mechanically and thermally averaged densities of electrons and nuclei. We note that contrary to Butriy *et al.* [18], who describe the nuclei of a multicomponent system by a density matrix *for all species*, we employ separate densities for each environment nuclear species, while treating the solute nuclei as fixed. This approach gives meaningful results because the

external potential created by the solute nuclei brakes the translation invariance of the system, while Butriy *et al.* study truly isolated systems without an external potential.

We assume that the external potentials $v(\boldsymbol{r},\tau)$ and $V_\alpha(\boldsymbol{r},\tau)$, which act on the electrons and environment nuclei, respectively, are the sum of a static piece due to the fixed solute nuclei and a time-dependent piece which models the applied electromagnetic wave used to probe the system. Note that S is made stationary by the electron and nuclear densities corresponding to $v(\boldsymbol{r},\tau)$ and $V_\alpha(\boldsymbol{r},\tau)$. Finally, in (4.1), the intrinsic action A is the Legendre transform, with respect to the potentials v and V_α [16], of

$$\tilde{A}[v,\{V_\alpha\}] = i\log\mathrm{Tr}\left\{\exp\left(\beta\left[\mu_{\mathrm{el}}\hat{N}_{\mathrm{el}}+\sum_\alpha \mu_\alpha\hat{N}_\alpha\right]\right)\hat{U}(-i\beta;0)\right\}, \tag{4.2}$$

where μ_{el} and μ_α are the chemical potentials of the electrons and nuclei, while $\hat{N}_{\mathrm{el}}$ and $\hat{N}_\alpha$ denote the respective particle number operators. The proper choice of the species-specific chemical potentials in system with Coulombic interactions requires great care. In particular, when working in the grand canonical ensemble one must adjust the chemical potentials to maintain average charge neutrality in the thermodynamic limit. In the above, $\hat{U}$ denotes the quantum-mechanical evolution operator of the full system defined on the Keldysh contour.

Because of the many environment degrees of freedom, finding the time-dependent densities which make the action in (4.1) stationary is numerically challenging. Moreover, the explicit details of the time-dependent densities describing the environment are often irrelevant, because one is typically interested in properties of the solute. It is therefore acceptable to focus the modelling effort on the solute and describe the environment at a coarse-grained level of theory.

For equilibrium solute-solvent systems, Petrosyan and coworkers [19, 20] have

developed a rigorous joint density-functional theory, which applies the detailed *ab initio* description only to the solute while treating the solvent with a coarse-grained theory. In their approach, Petrosyan *et al.* obtain equilibrium properties of the solute-solvent system in two steps: first, by minimizing the full solute-solvent free energy over the environment electron degrees of freedom, they arrive at a coarse grained free energy functional in terms of the solute electron density and the environment nuclear densities, for which accurate and computationally tractable approximations exist [19, 20]. In a second step, a minimization of the coarse grained functional yields solute electron and environment nuclear equilibrium densities. Petrosyan *et al.* applied their approach to the study of surfaces and small molecules in solution and obtained encouraging results.

Following Petrosyan *et al.* [20], we split the total electron density in (4.1) into solute and environment contributions, $n(\boldsymbol{r},\tau) = n_{\mathrm{sol}}(\boldsymbol{r},\tau) + n_{\mathrm{env}}(\boldsymbol{r},\tau)$. Fundamentally, a rigorous separation of electrons into solute and environment electrons is, of course, impossible because of the quantum-mechanical indistinguishability of electrons. Nonetheless, making S stationary with respect to all physically allowed solvent electron densities and subsequently with respect to all physically allowed solute electron densities still is guaranteed to recover the correct total electron density. Of course, there are many ways to express the total density as a sum of two subsystem densities. As a result, instead of a unique solution there exists a vast degenerate set of solutions in joint time-dependent density-functional theory consisting of all solute and environment electron densities which sum up to the correct total electron density. In equilibrium joint density-functional theory [20], it turns out that practical approximations, such as the use of molecular pseudopotentials [21], break this degeneracy and pick out a particular solution. We expect something similar to occur here in our work as well.

Making the action stationary with respect to the environment electron density while holding the solute electron and environment nuclear densities fixed, we obtain a coarse-grained action functional S_{CG1},

$$\begin{aligned} S_{\mathrm{CG1}}[n_{\mathrm{sol}} \quad , \quad \{N_\alpha\}] &= \mathrm{stat}_{n_{\mathrm{env}}}\{A[n_{\mathrm{sol}}+n_{\mathrm{env}},\{N_\alpha\}] - \int_\Omega d\boldsymbol{r}\int_C d\tau n_{\mathrm{env}}(\boldsymbol{r},\tau)v(\boldsymbol{r},\tau) \\ &- \sum_\alpha \int_\Omega d\boldsymbol{r}\int_C d\tau N_\alpha(\boldsymbol{r},\tau)V_\alpha(\boldsymbol{r},\tau)\} - \int_\Omega d\boldsymbol{r}\int_C d\tau n_{\mathrm{sol}}(\boldsymbol{r},\tau)v(\boldsymbol{r},\tau) \\ &\equiv \mathcal{A}[n_{\mathrm{sol}},\{N_\alpha\},\{\boldsymbol{R}_I,Z_I\},\delta\phi] - \int_\Omega d\boldsymbol{r}\int_C d\tau n_{\mathrm{sol}}(\boldsymbol{r},\tau)v(\boldsymbol{r},\tau), \end{aligned} \tag{4.3}$$

where $\mathrm{stat}_{n_{\mathrm{env}}}$ indicates that $A - \int d\boldsymbol{r}\int d\tau n_{\mathrm{env}}v - \sum_\alpha \int d\boldsymbol{r}\int d\tau N_\alpha V_\alpha$ is made stationary with respect to variations of n_{env}. We include the coupling term for the environment nuclear densities in $\mathcal{A}$, though not formally necessary because it does not depend on n_{env}, to ensure that $\mathcal{A}$ describes a neutral system, thereby mitigating the need to capture long-range couplings within an approximate functional. Also, because n_{env} couples to the solute nuclei through $v(\boldsymbol{r},\tau)$ (ultimately through their locations and charges $\{\boldsymbol{R}_I,Z_I\}$) this introduces no additional essential dependencies into the functional $\mathcal{A}$ which must be approximated. Finally, in the above, $\delta\phi(\boldsymbol{r},\tau)$ denotes the potential which models electromagnetic wave used to probe the system.

To find practical approximations, we partition $\mathcal{A}$ into various known contributions and an unknown remainder $\Delta\mathcal{A}$ according to

$$\mathcal{A}[n_{\mathrm{sol}},\{N_\alpha\},\{\boldsymbol{R}_I,Z_I\},\delta\phi] = A_{\mathrm{sol}}[n_{\mathrm{sol}}]+A_{\mathrm{env}}[\{N_\alpha\}]+\Delta\mathcal{A}[n_{\mathrm{sol}},\{N_\alpha\},\{\boldsymbol{R}_I,Z_I\},\delta\phi], \tag{4.4}$$

where A_{sol} is the intrinsic action for the electrons of the *isolated solute*. This contribution is well-known and various reliable approximations, the simplest being the adiabatic local-density approximation, exist. Also, A_{env} denotes the intrinsic action of the isolated environment. Recently, much progress has been made in

constructing such action functionals for classical liquids [22, 23]. The remaining term $\Delta\mathcal{A}$ clearly requires more work. Optimistic that the first two terms above capture the largest contributions, one could proceed to expand $\Delta\mathcal{A}$ in a Taylor series respecting basic symmetries such as translational invariance and identifying integration kernels corresponding to basic interactions. The motivation for all of this, of course, is that if a reliable approximation to S_{CG1} is found, we can then compute the solute electron and solvent nuclear densities which make S_{CG1} stationary.

Rather than follow the above route of dealing explicitly with the solvent nuclei, for this initial work, we take a simpler tack that allows us to make contact with standard continuum solvent models. For this purpose, we eliminate the environment nuclei from S_{CG1} and introduce a new coarse-grained action functional S_{CG2} which is a functional of the solute electron density *only*,

$$\begin{aligned} S_{\mathrm{CG2}}[n_{\mathrm{sol}}] &= \mathrm{stat}_{\{N_\alpha\}}\mathcal{A}[n_{\mathrm{sol}},\{N_\alpha\},\{\boldsymbol{R}_I,Z_I\},\delta\phi] - \int_\Omega d\boldsymbol{r}\int_C d\tau n_{\mathrm{sol}}(\boldsymbol{r},\tau)v(\boldsymbol{r},\tau) \\ &\equiv \mathcal{G}[n_{\mathrm{sol}},\{\boldsymbol{R}_I,Z_I\},\delta\phi] - \int_\Omega d\boldsymbol{r}\int_C d\tau n_{\mathrm{sol}}(\boldsymbol{r},\tau)v(\boldsymbol{r},\tau). \end{aligned} \tag{4.5}$$

Again, we express the functional $\mathcal{G}$ as the sum of the intrinsic action of the isolated solute and a remainder $\Delta\mathcal{G}$, which describes the coupling to the environment,

$$\mathcal{G}[n_{\mathrm{sol}},\{Z_I,\boldsymbol{R}_I\},\delta\phi] = A_{\mathrm{sol}}[n_{\mathrm{sol}}] + \Delta\mathcal{G}[n_{\mathrm{sol}},\{\boldsymbol{R}_I,Z_I\},\delta\phi]. \tag{4.6}$$

Again, it is important to note that $\Delta\mathcal{G}$ is *non-universal* because it depends both on the static external potential created by the solute nuclei and on the time-dependent potential caused by the experimental probe. While the effect of the static piece is accounted for in most time-dependent solvation theories, such as the "polarizable continuum model" [14], the dependence of the coupling functional on

the time-dependent potential is typically *neglected*. The above result underscores the value of following the density-functional approach rigorously, so as to identify all potentially relevant dependencies.

4.3 A coarse-grained action functional for the water-solute system

To allow us to explore and test the potential of the above ideas in an actual application, in this section, we introduce a relatively simple, approximate joint time-dependent density-functional for the solute-water system which is based on the assumption that the coupling between solute and water is solely due to dielectric screening effects. To describe properly the interfacial region, where the dielectric response of water differs notably from the bulk response, we employ a model dielectric function which depends solely on the local *solute electron density*. Such an approach is a physically reasonable in that it interpolates smoothly between the dielectric response of vacuum and the bulk liquid and thus avoids the need to specify a cavity shape. Also, in contrast to various "polarizable continuum model" approaches [14], where a particular value for the high-frequency dielectric constant is chosen, we employ the full frequency-dependent dielectric function.

We approximate S_{CG2}, defined in (4.5), by

$$\begin{aligned} S_{\mathrm{CG2}} &= A_s - A_{xc} - \Delta V_{ps} - \frac{1}{2}\int_\Omega d\boldsymbol{r}\int_C d\tau\tilde{\phi}(\boldsymbol{r},\tau)\left[-n_{sol}(\boldsymbol{r},\tau)+\sum_I Z_I\delta(\boldsymbol{r}-\boldsymbol{R}_I)\right] \\ &+ \int_\Omega d\boldsymbol{r}\int_C d\tau n_{\mathrm{sol}}(\boldsymbol{r},\tau)\delta\phi(\boldsymbol{r},\tau), \end{aligned} \tag{4.7}$$

where A_s denotes the intrinsic action of non-interacting electrons, A_{xc} is the exchange-correlation contribution, and $\tilde{\phi}(\boldsymbol{r},\tau)$ denotes the screened electrostatic

potential obtained by solving

$$\nabla \cdot \epsilon(\boldsymbol{r},\omega)\nabla\tilde{\phi}(\boldsymbol{r},\omega) = -4\pi\left(-n_{sol}(\boldsymbol{r},\omega) + \sum_I Z_I\delta(\boldsymbol{r}-\boldsymbol{R}_I)\right). \tag{4.8}$$

Finally, in the above ΔV_{ps} reflects the fact that, in practical calculations, we employ the *pseudopotential approximation* [24], in which the nuclei are replaced with ionic cores of charge Z_I, whose potentials at large distances (when not screened by the environment) go as $Z_I/|\boldsymbol{r}-\boldsymbol{R}_I|$ but which differ from this by a localized function $\Delta V_{ps}(\boldsymbol{r}-\boldsymbol{R}_I)$ within a small "core radius" that represents a distance much smaller than where we would expect screening from the environment to occur. Within our framework, the long-range parts of $Z_I/|\boldsymbol{r}-\boldsymbol{R}_I|$ enter through the solution of (4.8) and thus are properly screened, and the short-range parts contained in ΔV_{ps} enter directly as they require no such screening.

In the above, all information about the environment is contained in the dielectric function $\epsilon(\boldsymbol{r},\omega)$. We next make the natural assumption that the system is in equilibrium before the excitation and that the environment nuclei, representing slow degrees of freedom, do not move significantly during the excitation so that the cavity shape remains constant. Within this model, the dielectric function depends only on the solute electron density $n_0(\boldsymbol{r})$ *before the excitation*

$$\epsilon(\boldsymbol{r},\omega) = \epsilon(n_0(\boldsymbol{r}),\omega). \tag{4.9}$$

If we further assume that the frequency dependence of $\epsilon(n_0(\boldsymbol{r}),\omega)$ enters only through the frequency dependence of the bulk dielectric function $\epsilon_b(\omega)$, we can generalize the form employed by Petrosyan and co-workers [19] to

$$\epsilon(\boldsymbol{r},\omega) = 1 + \frac{\epsilon_b(\omega)-1}{2}\mathrm{erfc}\left(\frac{\log(n_0(\boldsymbol{r})/n_c)}{\sqrt{2}\sigma}\right), \tag{4.10}$$

where the parameters n_c and σ determine the location and width, respectively, of the crossover from the vacuum to the bulk liquid dielectric response. Petrosyan

et al. [19] determined the numerical values $n_c = 4.73 \times 10^{-3} \mathring{A}^{-3}$ and $\sigma = 0.6$ for these parameters by fitting solvation energies of small molecules obtained by their equilibrium joint density-functional theory to experimental data. We choose to work with these values as well and note that the value of n_c sets a physically reasonable length scale for the dielectric response of about 6 $\mathring{A}$. The above functional form for $\epsilon(\boldsymbol{r}, \omega)$ allows for a simple description of the dielectric response of inhomogeneous water. We note that Fattebert and Gygi [25] employ a different functional form for the dielectric response and find similar results for solvation free energies as Petrosyan *et al.* [19].

To obtain excitation energies of the solute, we analyze the linear response of (4.7) to a weak perturbation due to an electromagnetic wave used to probe the system. In the resulting Dyson equation, the bare frequency-independent Coulomb interaction $K(\boldsymbol{r}, \boldsymbol{r}') = 1/|\boldsymbol{r} - \boldsymbol{r}'|$ is replaced by a screened *frequency-dependent* Coulomb interaction $\tilde{K}(\boldsymbol{r}, \boldsymbol{r}'|\omega)$, which maps solute electron densities onto screened potentials by solving (4.8). We note that $\tilde{K}$ is a linear operator because $\epsilon(\boldsymbol{r}, \omega)$ depends *only* on the solute electron density before the excitation. Employing the standard transition-space notation [26], where the fused index $\kappa = (k, j)$ denotes a transition between the two Kohn-Sham orbitals $\psi_j(\boldsymbol{r})$ and $\psi_k(\boldsymbol{r})$, we can express the Dyson equation as a self-consistent eigenvalue problem [10, 26],

$$\sum_{\nu} \left(\delta_{\kappa\nu} \Delta\epsilon_{\nu} + \tilde{M}_{\kappa\nu}(\Omega) \right) F_{\nu} = \Omega F_{\kappa}, \tag{4.11}$$

where Ω denotes the energy of the excited state and $\Delta\epsilon_{\kappa} = \epsilon_j - \epsilon_k$ with ϵ_k being the energy of a Kohn-Sham orbital. The coupling matrix

$$\tilde{M}_{\kappa\nu}(\Omega) = \alpha_{\nu} \int_{\Omega} d\boldsymbol{r} \int_{\Omega} d\boldsymbol{r}' \Phi^*_{\kappa}(\boldsymbol{r}) \left[\tilde{K}(\boldsymbol{r}, \boldsymbol{r}'|\Omega) + f_{xc}(\boldsymbol{r}, \boldsymbol{r}'|\Omega) \right] \Phi_{\nu}(\boldsymbol{r}') \tag{4.12}$$

is expressed in terms of $\Phi_{\kappa}(\boldsymbol{r}) = \psi^*_k(\boldsymbol{r})\psi_j(\boldsymbol{r})$, the exchange-correlation kernel $f_{xc} = \delta^2 A_{xc}/\delta n^2$ and $\alpha_{\nu} = f_k - f_j$ with $f_k = 0$ or 2 denoting the orbital occupancy.

We note that even if one employs a frequency-independent exchange-correlation kernel, the solvent response makes $\tilde{M}$ *frequency dependent*. Because we are dealing with electronic excitations in molecules the frequencies of interest are expected to be a few electron volts.

To solve (4.11), we start with single-particle orbitals from an equilibrium joint density-functional theory calculation and we approximate $\tilde{K}(\boldsymbol{r}, \boldsymbol{r}'|\Omega) \approx K(\boldsymbol{r}, \boldsymbol{r}')$. This gives a first estimate for the excitation energies Ω_1 of the solvated molecule. Next, we use $\tilde{K}(\boldsymbol{r}, \boldsymbol{r}'|\Omega) \approx \tilde{K}(\boldsymbol{r}, \boldsymbol{r}'|\Omega_1)$ and repeat solving (4.11) until self-consistency is achieved.

To complete the theory, a model is needed for the frequency-dependent bulk-dielectric constant $\epsilon_b(\omega)$. Equation (4.11) shows that we only need to evaluate $\epsilon_b(\omega)$ at the electronic excitation energies of the solute. We may therefore employ a model which ignores the complicated low-frequency dielectric response of water (including reorientations of the molecules) but which describes the high-frequency range reliably. We use the very simple form

$$\epsilon_b(\omega) = 1 + 4\pi n_b \bar{\alpha}(\omega), \tag{4.13}$$

where n_b denotes the bulk particle density of water and $\bar{\alpha}(\omega) = \sum_j f_j/(\omega_j^2 - \omega^2)$ denotes the mean polarizability of an isolated water molecule with f_j and ω_j being the oscillator strength and excitation frequencies of the j-th excitation, respectively. Below, we compute $\bar{\alpha}(\omega)$ using time-dependent density-functional theory and demonstrate that (4.13) indeed reliably describes the bulk screening response to low-lying electronic excitations. We note that at the frequencies of electronic excitations, which are on the order of a few eV, $\epsilon_b(\omega)$ is generally close to unity because the slow ionic degrees of freedom cannot follow the external field and the contribution to the dielectric response from the fast electronic degrees

of freedom is much smaller than the contribution from the reorientation of the permanent molecular dipoles. This justifies the use of the simple model for $\epsilon_b(\omega)$ described above which neglects the contribution to the dielectric response from the permanent molecular dipole moments. For a more realistic description of the dielectric response of water, one could employ the Clausius-Mossotti expression for the dielectric constant [27].

4.4 Application to formaldehyde in aqueous solution

As a test case, we study the excited states of a formaldehyde molecule, CH_2O, in an aqueous solution. A number of theoretical approaches have been applied to study solvato-chromic shifts of formaldehyde in water [14, 15]. However, the agreement with experimental findings is typically unsatisfactory.

First, we explore the excitations of formaldehyde in the gas phase. For this purpose, we first carry out density-functional calculations in the local density approximation [28, 29] to find the ground state structure of formaldehyde. We employ a plane-wave basis, Kleinman-Bylander pseudopotentials [30] with a cutoff energy of 40 hartree, use a cubic supercell with linear dimensions of 20 bohr, and fully relax the electronic and ionic structure.

We then solve the linear response equation of time-dependent density-functional theory [10, 26] using the ground state Kohn-Sham orbitals and energies as input. Working with the adiabatic local density approximation which is known to reliably describe low-lying excitations in molecules [10], we find the lowest singlet excitation energies to be converged to within 0.01 eV when the 4 lowest unoccupied and the 4 highest occupied Kohn-Sham orbitals are taken into account. Table 4.1 compares

our results for the lowest three singlet states with previous TDDFT calculations employing the adiabatic local density approximation by Bauernschmitt and Ahlrich [31] and also with experimental findings [14, 31]. We observe that our excitation energy for the lowest state is relatively close to the experimental value, while the higher states deviate more than 1 eV from experiment. The failure to describe high-energy excitations accurately is typical for TDDFT calculation in the adiabatic local density approximation and has been identified with an incorrect asymptotic behavior of the exchange-correlation potential at large distances [32].

To compute excitation energies of a formaldehyde molecule in aqueous solution, we need to determine the frequency-dependent dielectric response of water. According to (4.13), this requires the mean polarizability of an isolated water molecule, which involves a summation over all excited states. In our calculation, we employ the same approximations as in the above formaldehyde calculation and use all 5 occupied Kohn-Sham orbitals, plus an additional 175 unoccupied orbitals to compute $\bar{\alpha}(\omega)$. Table 4.2 shows our results for the three lowest singlet excitation energies of an isolated water molecule and compares them to previous theoretical work [33] and also to experiment [33]. Comparing Tables 4.1 and 4.2, we observe that the lowest singlet excitation energy of formaldehyde is much smaller than the corresponding value for water, justifying the use of a *frequency-independent* coupling matrix $\tilde{M}$ in (4.11) — a common approximation in "polarizable continuum model" approaches, which for the "non-equilibrium response," employ a frequency-independent dielectric function derived from the index of refraction of water [14]. However, it is important to note that the use of a *frequency-independent* coupling matrix can only be justified for the lowest lying singlet excited state of formaldehyde. Higher excited states of formaldehyde are much closer to the lowest excited states of water necessitating the full self-consistent solution of (4.11).

Table 4.1: Comparison of the three lowest singlet excitation energies of an isolated formaldehyde molecule with previous theoretical work by Bauernschmitt *et al.*[31] and experiment [14, 31]. All energies are given in eV.

present work	Bauernschmitt *et al.*	exp.
3.66	3.64	3.8-4.2
5.68	5.93	7.13
6.78	6.79	8.14

Table 4.2: Comparison of the three lowest singlet excitation energies of an isolated water molecule with previous theoretical work by Bernasconi [33], which also employs the adiabatic local density approximation, and experiment [33]. All results are given in eV.

our work	Bernasconi	experiment
6.47	6.39	7.4
7.74	7.78	9.1
8.01	8.05	9.7

Table 4.3 compares our result for the polarizability of an isolated water molecule and the resulting prediction for $\epsilon_{\text{“}\infty\text{”}} \equiv \epsilon_b(\omega = 1\ eV)$ of *liquid water* with previous calculations [34, 35] and also with experiment [34, 35]. We note that the relatively good agreement of our result for $\epsilon_{\text{“}\infty\text{”}}$ with the experimental value results from an interesting cancellation of errors: density-functional theory *overestimates* the polarizability of an isolated water molecule, but the neglect of intermolecular correlations in (4.13) leads to an *underestimation* of the bulk response [36].

Finally, we compute the excitation energies of a solvated formaldehyde molecule. Neglecting ionic relaxations induced by the aqueous environment, we first determine the equilibrium electronic structure of the formaldehyde molecule in aqueous solution using the joint density-functional theory of Petrosyan *et al.* [19]. We then solve (4.11) with the resulting equilibrium Kohn-Sham orbitals and energies using the *bare* Coulomb interaction and obtain a first approximation for the solvato-chromic shifts. We then recompute the lowest excitation energy with the screened interaction $\tilde{K}$ evaluated at the corresponding energy from the first iteration. Table 4.4 summarizes our results, which are in good agreement with the experimental values of the solvato-chromic shift of the lowest singlet excitation [15].

To understand the physical origin of the observed blue-shift of the lowest excitation energy upon solvation, we observe that the ground state of formaldehyde possesses a relatively large dipole moment, which leads to a reduction of the ground state energy upon solvation. In contrast, the dipole moment of the first excited state is much smaller, such that the energy of this state is much less affected by the aqueous environment. This results in an increase of the energy level spacing or, in other words, a blue-shift of the excitation frequency.

Table 4.5 compares our result for the solvato-chromic shift of the lowest singlet

Table 4.3: Comparison of our results for the static mean polarizability for an *isolated* water molecule and for $\epsilon_{\text{“}\infty\text{”}} \equiv \epsilon_b(\omega = 1\ eV)$ of *liquid water* with previous theoretical calculations carried out by Hu *et al.*[34] and experiment [34, 35].

	units	our work	Hu	experiment
$\bar{\alpha}(\omega = 0)$	$bohr^3$	10.4	10.5	9.6
$\epsilon_{\text{“}\infty\text{”}}$		1.65	—	1.78

Table 4.4: Solvato-chromic shifts obtained from joint time-dependent density-functional theory of formaldehyde in aqueous solution and comparison to experiment [15]. All results are in units of eV; the first column repeats data from Table 4.1 with higher precision.

vacuum	1^{st} iteration	2^{nd} iteration	shift	exp.
3.658	3.863	3.842	0.184	0.21
5.685	5.541	—	-0.144	—
6.776	6.646	—	-0.130	—

excitation with previous theoretical work [14, 15] and also with experiment [15]. In contrast to our calculation, which gives very good agreement with the experimental data, calculations employing the "polarizable continuum model" in combination with time-dependent density-functional theory underestimate the shift [14], while approaches, which describe the solute by coupled-cluster theory while treating the solvent atomistically [15], typically overestimate the shift. We point out that both methods suffer from weaknesses which are absent in our approach. In particular, it is well-known that the results of the "polarizable continuum model" approach depend sensitively on the cavity size and shape. This indicates that a more realistic description of the interfacial region, which is achieved by our approach, is of great importance. In contrast to implicit solvation models, atomistic treatments of the solvent offer a reliable description of the interfacial region, but to compute converged thermodynamic averages the sampling of many solvent configurations, at each of which the solute excitations have to be computed, is required. Our approach, in contrast, directly computes the *thermodynamically averaged* excitation energies.

We note that *in principle* in our approach we do *not* invoke the Born-Oppenheimer approximation for the nuclei of the solvent. Instead, we compute the poles of the *ensemble-averaged* response function. However, as an approximation for this first test application, we have in fact ignored the nuclear motions in our estimate of $\epsilon_b(\omega)$.

Table 4.5: Comparison of our joint time-dependent density-functional theory results, previous theoretical work by Cossi *et al.* [14] and Kongsted *et al.* [15] and experiment [15] for the solvato-chromic shift of the lowest singlet excited state of formaldehyde in aqueous solution. All results are given in eV.

	shift
our work	0.18
experiment	0.21
Cossi *et al.*	0.11
Kongsted *et al.*	0.32

4.5 Summary and conclusions

In sum, we have described the construction of a *joint* time-dependent density-functional theory for the modelling of the solute-solvent system. We have demonstrated how to systematically derive coarse-grained action functionals by eliminating environment degrees of freedom. This enabled us to examine the underlying assumptions and uncover previously ignored functional dependencies in poplar approaches such as the time-dependent "polarizable continuum model" and to explore their domains of validity. We also introduced an explicit, approximate joint time-dependent density functional for the modelling of electronic system in aqueous solution, and apply this functional to study excitations of solvated formaldehyde, and find very good agreement with experiment.

BIBLIOGRAPHY

[1] G. D. Scholes and G. Rumbles. *Nature Materials*, 5:683, 2006. 71

[2] M. Rohlfing and S. G. Louie. *Phys. Rev. Lett.*, 82:1959, 1999. 71

[3] F. Hide, M. A. Diaz-Garcia, B. J. Schwartz, M. R. Andersson, Q. Pei, and A. J. Heeger. *Science*, 273:1833, 1996. 71

[4] J. H. Burroughes, D. D. C. Bradley, A. R. Brown, R. N. Marks, K. Mackay, R. H. Friend, P. L. Burns, and A. B. Holmes. *Nature*, 347:539, 1990. 71

[5] D. Braun and A. J. Heeger. *Appl. Phys. Lett.*, 58:1982, 1991.

[6] R. H. Friend, R. W. Gymer, A. B. Holmes, J. H. Burroughes, R. N. Marks, C. Taliani, D. D. C. Bradley, D. A. Dos Santos, J. L. Brédas, M. Loegdlund, and W. R. Salanek. *Natures*, 397:121, 1999. 71

[7] C. J. Cramer. *Essentials of Computational Chemistry.* John Wiley and Sons, Chichester, 2002. 71

[8] R. J. Bartlett and M. Musial. *Phys. Rev. Mod.*, 79:291, 2007. 71

[9] E. Runge and E. K. U. Gross. *Phys. Rev. Lett.*, 52:997, 1984. 72, 73

[10] M. E. Casida. *Recent Developments and Applications of Modern Density Functional Theory, Theoretical and Computational Chemistry.* Elsevier Science, Amsterdam, 1996. 72, 80, 82

[11] A. Tsolakidis, D. Sánchez-Portal, and R. M. Martin. *Phys. Rev. B*, 66:235416, 2002. 72

[12] R. Bauernschmitt, R. Ahlrichs, F. H. Hennrich, and M. M. Kappes. *J. Am. Chem. Soc.*, 120:5052, 1998.

[13] S. Fantacci, F. De Angelis, and A. Selloni. *J. Am. Chem. Soc.*, 125:4381, 2003. 72

[14] M. Cossi and V. Barone. *J. Chem. Phys.*, 115:4708, 2001. 72, 77, 78, 82, 83, 84, 89, 90

[15] J. Kongsted, A. Osted, K. V. Mikkelsen, P.-O. Astrand, and O. Christiansen. *J. Chem. Phys.*, 121:8435, 2004. 72, 82, 86, 88, 89, 90

[16] R. van Leeuwen. *Phys. Rev. Lett.*, 80:1280, 1998. 72, 73, 74

[17] L. V. Keldysh. *Sov. Phys. JETP*, 20:1018, 1965. 73

[18] O. Butriy, H. Ebadi, P. L. de Boeij, R. van Leeuwen, and E. K. U. Gross. *Phys. Rev. A*, 76:052514, 2007. 73

[19] S. A. Petrosyan, A. A. Rigos, and T. A. Arias. *J. Chem. Phys. B*, 109:15436, 2005. 74, 75, 79, 80, 86

[20] S. A. Petrosyan, J.-F. Briere, D. Roundy, and T. A. Arias. *Phys. Rev. B*, 75: 205105, 2007. 74, 75

[21] I. Park, K. Cho, S. Lee, K. S. Kim, and J. D. Joannopoulos. *Comp. Mat. Sc.*, 21:291, 2001. 75

[22] G. K.-L. Chan and R. Finken. *Phys. Rev. Lett.*, 94:183001, 2005. 77

[23] A. J. Archer. *J. Phys.: Condens. Matter*, 18:5617, 2006. 77

[24] M. C. Payne, M. P. Teter, D. C. Allan, T. A. Arias, and J. D. Joannopoulos. *Pys. Rev. Mod.*, 64:1045, 1992. 79

[25] J.-L. Fattebert and F. Gygi. *J. Comput. Chem.*, 23:662, 2002. 80

[26] M. Petersilka, U. J. Grossmann, and E. K. U. Gross. *Phys. Rev. Lett.*, 76: 1212, 1995. 80, 82

[27] N. W. Ashcroft and N. D. Mermin. *Solid State Physics*. Saunders, Philadephia, 1976. 82

[28] P. Hohenberg and W. Kohn. *Pys. Rev.*, 136:B864, 1964. 82

[29] W. Kohn and L. J. Sham. *Phys. Rev.*, 140:A1133, 1965. 82

[30] L. Kleinman and D. M. Bylander. *Phys. Rev. Lett.*, 48:1425, 1982. 82

[31] R. Bauernschmitt and R. Ahlrichs. *Chem. Phys. Lett.*, 256:454, 1996. 83, 84

[32] M. E. Casida and D. R. Salahub. *J. Chem. Phys.*, 113:8918, 2000. 83

[33] L. Bernasconi. *J. Chem. Phys.*, 132:184513, 2010. 83, 85

[34] A. Hu, D. M. York, and T. K. Woo. *J. Mol. Struc. (Theochem)*, 591:255, 2002. 86, 87

[35] V. Garbuio, M. Cascella, and O. Pulci. *J. Phys.: Condens. Matter*, 21:033101, 2009. 86, 87

[36] M. Yang, P. Senet, and C. van Alsenoy. *Int. J. Quant. Chem.*, 101:535, 2005. 86

CHAPTER 5

PHONON-PHONON INTERACTIONS IN CARBON NANOTUBES

We present a theoretical study of the intrinsic quality factor of the fundamental flexural vibration in a carbon nanotube and its dependence on temperature, radius, length and tension. In particular, we examine three- and four-phonon decays of the fundamental flexural mode within quantized elasticity theory. This analysis reveals design principles for the construction of ultrasensitive nanotube mass sensors: under tensions close to the elastic limit, intrinsic losses allow for *single yoctogram* mass resolution at room temperature, while cooling opens the possibility of *sub-yoctogram* mass resolution.

5.1 Introduction

Recently, much experimental effort has gone into fabricating nano-electromechanical systems (NEMS) which employ carbon nanotubes as mechanical resonators [1–4]. The combination of small mass density and large mechanical stiffness makes carbon nanotube NEMS ideal candidates for ultrasensitive mass detectors which do not require disruptive ionization of the analyzed molecule: recent experiments achieved a mass resolution of ~ 100 yg (1 yg=10^{-24} g) corresponding to approximately 60 protons or 5 C^{12} atoms[5, 6]. However, for isotopic or chemical identification of molecules adsorbed on the nanotube or real-time monitoring of chemical reactions *yoctogram* mass resolution is necessary.

The mass resolution of nanotube NEMS depends strongly on the quality factor of the lowest flexural mode, which imposes a lower bound on the frequency differences which can be resolved. The quality factors found in most experiments have

been surprisingly low, not exceeding $Q \approx 2000$ [4, 5, 7]. Only very recently, Hüttel *et al.* [3] measured $Q \gtrsim 10^5$, but at *milikelvin* temperatures.

The *intrinsic* quality factor of a nanotube sets aside all extrinsic losses, such as defect or clamping losses, and sets an upper limit to the quality factor achievable in experiment. Both molecular dynamics simulations [8] and analytical approaches [9, 10] have been used to study the intrinsic quality factor theoretically, finding relatively low values similar to those in the experiments. However, simulations are typically limited to extremely short tubes, and the analytical approaches to date have either employed simplified phonon spectra [9] or focused solely on low-temperature four-phonon decays of the flexural mode using an analysis appropriate to extremely long tubes[10].

In this chapter, we present a theoretical analysis appropriate to the length of tubes and operating temperatures commonly found in experiments. We discover that application of tension drastically increases the intrinsic quality factor of nanotube oscillators and opens for the first time the theoretical possibility of *single yoctogram* mass resolution in such oscillators at room temperature, with further improvements possible with cooling. Indeed, the recent experiments of Wei *et al.* demonstrate a promising technique for controlling the tension in nanotubes[11].

5.2 Continuum elastic theory

In this section, we review briefly the continuum elastic theory of semiconducting carbon nanotubes.

The earliest work of which we are aware to consider continuum theories for

graphene sheet materials is that of Krumhansl and co-workers [13, 14] in the 1950s, who explained the low temperature behavior of the specific heat of graphite in terms of a linear elastic Hamiltonian for stacked graphene layers (similar to our (5.11)), which they found to exhibit quadratic dispersion relations from the bending of the sheets which then led to an unusually high specific heat. Below, we too find such quadradic dispersions for carbon nanotubes (Figure 5.6).

Our treatment follows closely De Martino *et al.* [10] both in content and notation. In particular, the expressions for the anharmonic parts of the Hamiltonian, (5.12) and (5.16) in this chapter, are identical to Equations (13) and (16) of reference [10] and are only reproduced here for the readers' convenience. Contrary to De Martino *et al.*, who discuss the effects of curvature in the appendix of their paper, we take curvature effects into account *from the outset*. These curvature contributions to the elastic energy are of crucial importance for describing optical modes in nanotubes: without them, the gaps of certain optical modes *vanish*. We also note that the harmonic part of our theory is equivalent to the one studied by Suzuura and Ando [12], but with different elastic constants.

5.2.1 Strain and curvature tensor

Following De Martino *et al.* [10], we describe a carbon nanotube as a rolled up isotropic elastic sheet. Due to the hexagonal symmetry of the graphene sheet, which at quadratic order forbids all anisotropic terms in the elastic free energy, this approach is well justified.

Let us consider a point with coordinates (x, y) on an undeformed graphene sheet of length $2\pi R$ in the x-direction and length L in the y-direction. When

rolled up into an undeformed nanotube, a perfect cylinder of radius R, this point will be located at

$$\boldsymbol{R}(x,y) = R\hat{\boldsymbol{e}}_z(x) + y\hat{\boldsymbol{e}}_y, \tag{5.1}$$

where $\hat{\boldsymbol{e}}_z(x)$ is a unit vector pointing in the radial direction and $\hat{\boldsymbol{e}}_y$ points along the tube axis. A third unit vector $\hat{\boldsymbol{e}}_x(x)$ is tangential to the tube surface. The position of the point on a deformed tube is

$$\boldsymbol{r}(x,y) = \boldsymbol{R}(x,y) + \sum_{n=x,y,z} u_n(x,y)\hat{\boldsymbol{e}}_n(x), \tag{5.2}$$

where u_x, u_y and u_z denote displacements from the undeformed configuration and are assumed to be small.

The strain tensor u corresponding to such a deformation is the sum of a part which is linear in the displacements and a nonlinear part,

$$u = u^{lin} + u^{nlin}, \tag{5.3}$$

with

$$2u_{ij}^{lin} = D_i u_j + D_j u_i, \tag{5.4}$$

$$2u_{ij}^{nlin} = \sum_{n=x,y,z} (D_i u_n)(D_j u_n), \tag{5.5}$$

where we introduced the covariant derivatives

$$D_x u_x = \frac{\partial u_x}{\partial x} + \frac{u_z}{R}, \qquad D_x u_z = \frac{\partial u_z}{\partial x} - \frac{u_x}{R}, \tag{5.6}$$

while $D_y u_n = \partial u_n/\partial y$ and $D_x u_y = \partial u_y/\partial x$.

The curvature tensor S of the deformed nanotube is

$$S = g^{-1}h, \tag{5.7}$$

where $g_{ij} = \delta_{ij} + 2u_{ij}$ is the metric tensor of the deformed tube and

$$h_{ij} = \hat{\boldsymbol{n}} \cdot \partial_i \partial_j \boldsymbol{r} \tag{5.8}$$

denotes the second fundamental form.

Expanding (5.7) in powers of the displacement up to linear order yields

$$S = \begin{bmatrix} -1/R + \partial_x^2 u_z + u_z/R^2 & \partial_x \partial_y u_z - \partial_y u_x/R \\ \partial_x \partial_y u_z + \partial_x u_y/R & \partial_y^2 u_z \end{bmatrix}. \tag{5.9}$$

5.2.2 Elastic energy

In this section, we derive an expression for the elastic energy in terms of the strain tensor and the curvature tensor. The standard locality assumption of elasticity theory allows us to express the total Hamiltonian as an integral of the elastic energy density

$$\mathcal{H} = \sum_n \frac{p_n^2}{2\rho_M} + \mathcal{U}(u, S), \tag{5.10}$$

where ρ_M denotes the mass density per unit area of graphene, p_n denotes the canonically conjugate momenta and $\mathcal{U}$ is the potential energy per unit area.

Next, we employ symmetry considerations to determine $\mathcal{U}(u, S)$. At quadratic order, the hexagonal graphene sheet is isotropic, which allows us to express the various contributions to the elastic energy in terms of traces of the matrix degrees of freedom u and S. Assuming isotropy also at higher orders and neglecting curvature terms, which are generally considered to be small, beyond the quadratic order, we find

$$\mathcal{U}_2 = \frac{\lambda}{2}(\mathrm{Tr}u)^2 + \mu \mathrm{Tr}u^2 + \frac{k_c}{2}\left(\mathrm{Tr}(S - S_0)\right)^2, \tag{5.11}$$

$$\mathcal{U}_3 = \zeta_1(\mathrm{Tr}u)^3 + \zeta_2 \mathrm{Tr}u^2 \mathrm{Tr}u, \tag{5.12}$$

$$\mathcal{U}_4 = \sigma_1(\mathrm{Tr}u)^4 + \sigma_2(\mathrm{Tr}u)^2 \mathrm{Tr}u^2 + \sigma_3(\mathrm{Tr}u^2)^2, \tag{5.13}$$

where $\mathcal{U}_2, \mathcal{U}_3$ and $\mathcal{U}_4$ denote contributions to the energy density including quadratic,

cubic and quartic powers of u_{ij} and S_{ij}. Also, λ and μ denote the effective two-dimensional Lamé moduli, k_c the bending stiffness and S_0 the curvature tensor of the undeformed tube. ζ_1, ζ_2, σ_1, σ_2 and σ_3 are anharmonic elastic constants. We note that at quadratic order a term proportional to $\mathrm{Tr}(S - S_0)^2$ need not be included [12], because the integral of the Gaussian curvature of the entire surface is a topological invariant.

Expanding the strain and curvature tensors in terms of their linear and nonlinear parts, we now express the Hamiltonian as a power series in terms of the *displacements* as

$$\mathcal{H} = \mathcal{H}_2 + \mathcal{H}_3 + \mathcal{H}_4, \tag{5.14}$$

with

$$\begin{aligned}
\mathcal{H}_2 &= \sum_n \frac{p_n^2}{2\rho_M} + \frac{\lambda}{2}(\mathrm{Tr}u^{lin})^2 + \mu \mathrm{Tr}\left[(u^{lin})\right]^2 + \frac{k_c}{2}(\mathrm{Tr}S^{lin})^2, && (5.15)\\
\mathcal{H}_3 &= \lambda \mathrm{Tr}u^{nlin}\mathrm{Tr}u^{lin} + 2\mu \mathrm{Tr}(u^{lin}u^{nlin}) + \zeta_1 \left(\mathrm{Tr}u^{lin}\right)^2 \\
&+ \zeta_2 \mathrm{Tr}u^{lin}\mathrm{Tr}\left[(u^{lin})^2\right], && (5.16)\\
\mathcal{H}_4 &= \frac{\lambda}{2}(\mathrm{Tr}u^{nlin})^2 + \mu \mathrm{Tr}[(u^{nlin})^2] + 3\zeta_1 \mathrm{Tr}u^{nlin}(\mathrm{Tr}u^{lin})^2 \\
&+ \zeta_2 \mathrm{Tr}u^{lin}[2\mathrm{Tr}(u^{lin}u^{nlin}) + \mathrm{Tr}u^{nlin}\mathrm{Tr}u^{lin}] && (5.17)\\
&+ \sigma_1(\mathrm{Tr}u^{lin})^4 + \sigma_2(\mathrm{Tru^{lin}})^2\mathrm{Tr}[(u^{lin})^2] + \sigma_3(\mathrm{Tr}[(u^{lin})^2])^2, && (5.18)
\end{aligned}$$

where $\mathcal{H}_2$, $\mathcal{H}_3$ and $\mathcal{H}_4$ now denote the second, third and fourth order contributions to the energy density in an expansion in terms of *displacements* and, again, we neglected curvature contributions beyond the quadratic order.

We note that the anharmonic terms fall into two classes: material nonlinearities, described by the explicitly higher-order terms in (5.12), and geometric nonlinearities, where the lower order terms, such as terms in (5.11), contribute at higher orders due to higher order terms in the expansion of u_{ij} in terms of the degrees of

freedom u_n due to the curvature of the tube. Material nonlinearities are often suppressed by a factor of kR (k being the phonon wavevector and R the tube radius) compared to geometric nonlinearities [10] and can therefore be neglected for long wavelength phonons. However, when evaluating the three-phonon contribution to the quality factor, high energy phonons, whose wavelength is no longer comparable to the length of the tube, play a crucial role. We, therefore, also consider in this work the contribution of material nonlinearities in the three-phonon decay channel.

5.3 *Ab initio* calculation of the elastic constants

We carry out *ab initio* density-functional theory calculations within the local density approximation [15, 16] to obtain accurate numerical values for the various elastic coefficients in the quadratic and cubic parts of the Hamiltonian.

First we determine λ and μ in $\mathcal{H}_2$ and ζ_1 and ζ_2 in $\mathcal{H}_3$. Inspection of (5.11) and (5.12) shows that the contributions to the elastic energy associated with these constants only involve *strain deformations* of the graphene sheet. We therefore compute the energy of a set of homogeneously strained graphene sheets and a set of uniaxially strained sheets, where in the latter case we relax the sheet in the direction transverse to the applied strain. In these calculations, we use a $14 \times 14 \times 1$ Monkhorst-Pack [17] k-point grid to sample the Brillouin zone and a Kleinman-Bylander [18] pseudopotential with an energy cut-off of 40 hartree. Finally, we adjust the elastic constants such that the elastic energy cost for the various deformations obtained from our continuum theory matches the *ab initio* results. Figures 5.1 and 5.2 show both the *ab initio* results and the results of our elastic continuum theory.

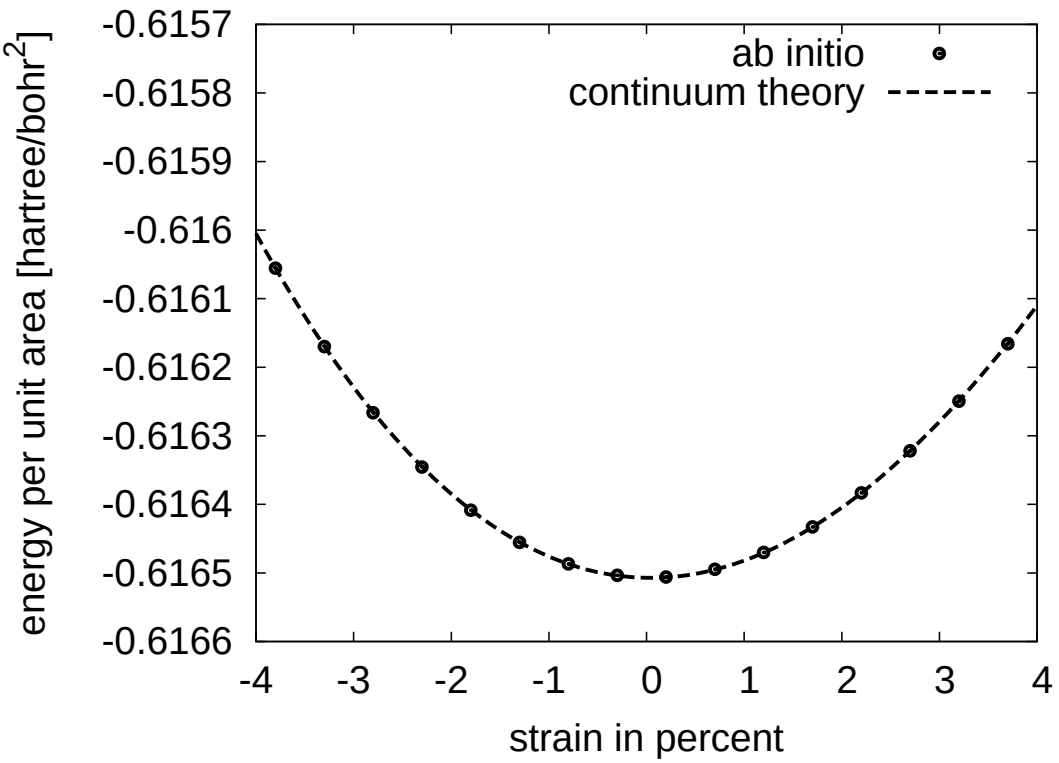

Figure 5.1: Energy per unit area for various amounts of homogeneous strain. Dots denote *ab initio results* and the dotted line denotes the prediction of the continuum approach.

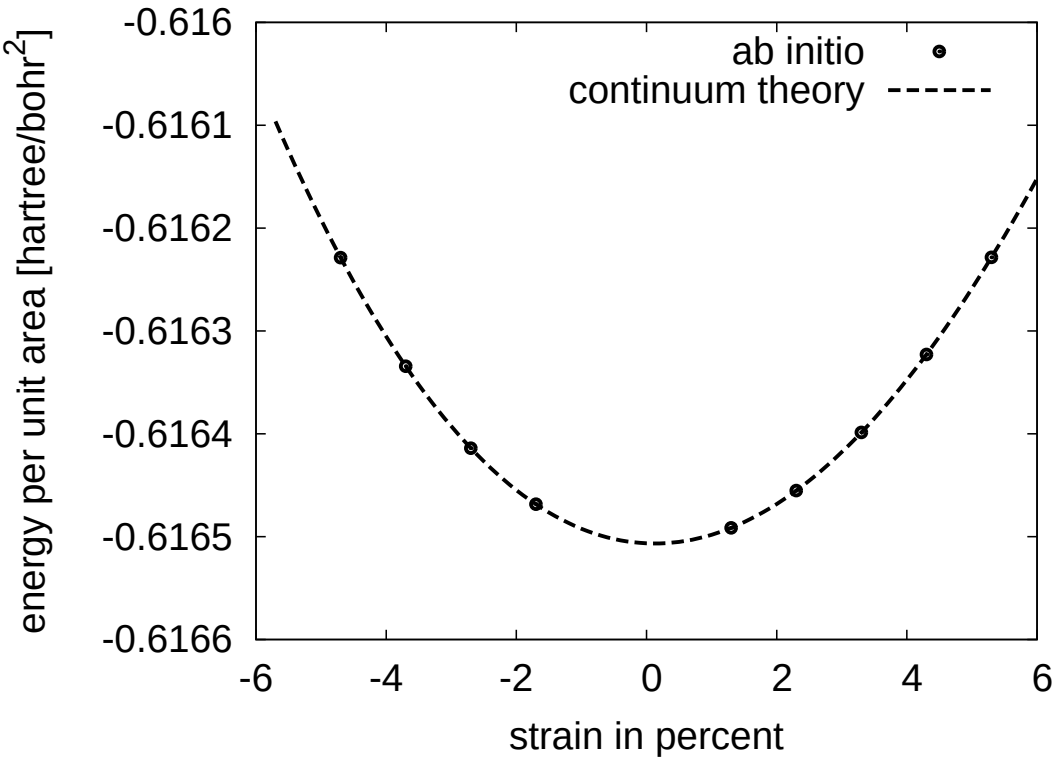

Figure 5.2: Energy per unit area for various amounts of uniaxial strain. Dots denote *ab initio results* and the dotted line denotes the prediction of the continuum approach.

Next, we compute the bending stiffness k_c by calculating the ground state energy of various $(n, 0)$ nanotubes and by subsequently fitting these energies to the prediction of elasticity theory,

$$\frac{E_{tot}(R)}{A} = C + \frac{k_c}{2R^2}, \tag{5.19}$$

where A denotes the area of the nanotube and the constant C is the energy density of an undeformed graphene sheet. In the nanotube calculations we use a $4 \times 1 \times 1$ k-point grid and the same pseudopotential as in the graphene calculations. Figure 5.3 shows good agreement between the *ab initio* results and the predictions of the continuum approach. Remarkably, continuum theory describes accurately the bending energy even for tubes with radii smaller than 0.4 nm. This surprising range of applicability of the continuum approach was also observed by Araujo *et al.* who studied the frequency of the radial breathing in very thin tubes[19].

Table 5.1 shows the resulting values for both the harmonic and the anharmonic elastic constants obtained from our *ab initio* calculations. Table 5.2 compares our results for the harmonic elastic constants of graphene to recent theoretical work and shows good agreement. We note that the Poisson ratio we compute is close to the experimental value of the basal plane of graphite, $\nu = 0.16$ [20, 21].

5.4 Quantization and phonon dispersions

The elastic theory is quantized by imposing canonical commutation relations for the momentum and displacement operator,

$$[p_n(\mathbf{r}), u_{n'}(\mathbf{r}')] = -i\hbar\delta_{nn'}\delta(\mathbf{r} - \mathbf{r}'). \tag{5.20}$$

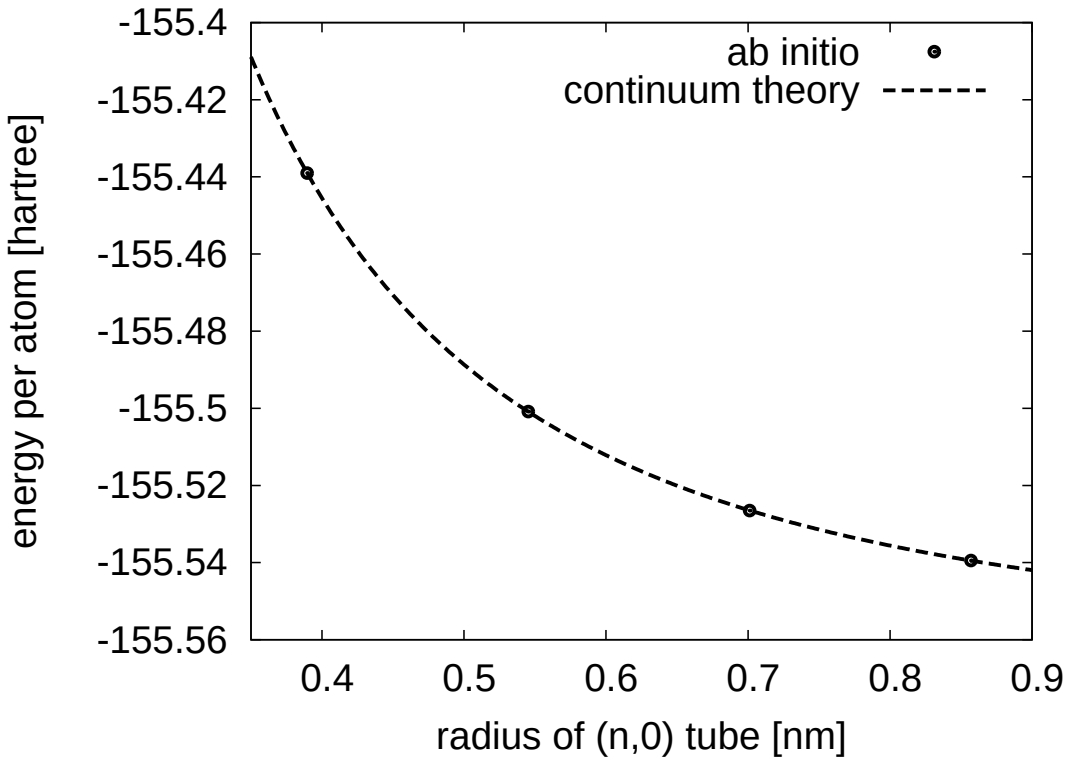

Figure 5.3: Energy per atom for various (n,0) carbon nanotubes. Dots denote *ab initio* results and the dotted line denotes the prediction of the continuum approach.

Table 5.1: Lamé moduli, anharmonic elastic constants of $\mathcal{U}_3$ and bending stiffness for semiconducting carbon nanotubes from *ab initio* density-functional calculations.

λ [J/m^2]	μ [J/m^2]	ζ_1 [J/m^2]	ζ_2 [J/m^2]	k_c [eV]
59.57	147.94	-145.17	-387.93	1.46

Table 5.2: Linear elastic constants of graphene computed by various authors. In the present work, the local density approximation and a plane wave basis set are employed. Kudin *et al.* [22] use the a generalized gradient approximation and a gaussian basis set, while Sánchez-Portal *et al.* [23] use the local density approximation and an atomic orbital basis. Zakharchenko *et al.* [24] employ an empirical bond order potential. Note that the Poisson ratio is given by $\nu = (K + \mu)/(K - \mu)$ and $Y = 4K\mu/(K + \mu)$ with $K = \lambda + \mu$.

Reported by	method	Y [J/m^2]	ν	k_c [eV]
present work	density-functional theory	345.48	0.168	1.46
Kudin *et al.*	density-functional theory	342.31	0.149	1.46
Zakharchenko *et al.*	classical Monte Carlo	346.44	0.147	—
Sánchez-Portal *et al.*	density-functional theory	358.44	—	1.49-1.61

Next, we express the displacement operator in terms of normal modes

$$\mathbf{u}(x,y) = \sum_{Jk\ell} e^{i\ell x/R + iky} \sqrt{\frac{\hbar}{2M\omega_J(k,\ell)}} \left(a_J(k,\ell) + a_J^\dagger(-k,-\ell) \right) \hat{\epsilon}_J(k,l), \qquad (5.21)$$

where J labels the normal mode, k is the wavevector along the tube axis, ℓ is the angular momentum quantum number, $M = 2\pi RL\rho_M$ is the total mass of the nanotube and $\omega_J(k,\ell)$ and $\hat{\epsilon}_J(k,\ell)$ are the phonon frequency and polarization unit vector, respectively. Also, in the above expression, $a_J(k,\ell)$ and $a_J^\dagger(k,\ell)$ are phonon destruction and creation operators, respectively, which obey the commutation relation

$$[a_J(k,\ell), a_{J'}^\dagger(k',\ell')] = \delta_{JJ'}\delta_{kk'}\delta_{\ell\ell'}. \qquad (5.22)$$

Figure 5.6 shows the resulting phonon dispersion curves for a carbon nanotube with radius $R = 0.5$ nm. We observe that the low-energy modes are in good agreement with force constant models[25] and *ab initio* calculations [23]. In particular, we find four acoustic branches: a twist and a longitudinal stretch mode, both having $\ell = 0$ and exhibiting a linear dispersion relation at long wavelengths, and two degenerate flexural modes with $\ell = \pm 1$ and quadratic dispersion relations

$$\omega_F(k) = \frac{\hbar k^2}{2m} + \mathcal{O}(k^4), \qquad m = \frac{\hbar}{R}\sqrt{\frac{\rho_M(\lambda+2\mu)}{8\mu(\lambda+\mu)}}, \qquad (5.23)$$

where ω_F denotes the angular frequency of the flexural phonon and $\rho_M = 7.68 \times 10^{-7}$ kg/m^2 is the areal mass density of graphene. We also find a variety of low-lying optical phonons. Note that inclusion of curvature terms into (5.11) is crucial to obtain the correct optical phonon spectrum. In particular, the gap of the lowest optical branch vanishes if curvature terms are neglected.

As expected of a continuum approach, we find that for high energies or large wavevectors the phonon dispersions in Figure 5.6 differ notably from the results of atomistic calculations. In particular, the continuum approach contains no notion

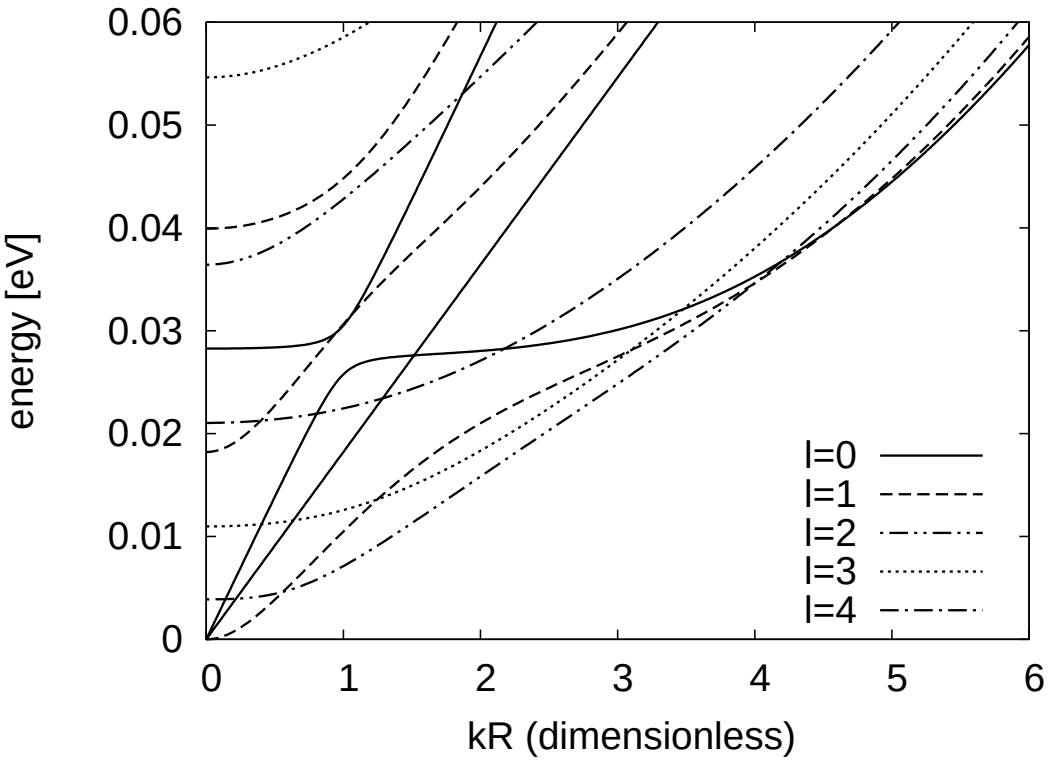

Figure 5.4: Phonon energy versus kR for a $R = 0.5$ nm tube. The four acoustic modes consist of two degenerate flexural modes with quadratic dispersion relations at long wavelengths, one longitudinal and one twist mode which have linear dispersions.

of a lattice spacing. Therefore, no Brillouin zone exists and the theory predicts phonons of arbitrarily short wavelengths. Also, the number of allowed angular momenta, infinite in a continuum theory, equals the number of unit cells along the circumference in a real tube. For the tubes we consider here, the radius R exceeds 0.4 nm so that there are at least ten such units, ensuring that $\ell = 0, \pm 1, \pm 2, \pm 3, \pm 4$ are all well defined. Phonons with high angular momenta have a high energy; Figure 5.6 shows that typically at room temperature only modes with angular momentum smaller than $\ell = 4$ are physically relevant.

5.5 Phonon-phonon interactions

In this section, we present the general framework for studying phonon-phonon interactions. Having so far analyzed the quadratic part of the Hamiltonian, we now focus on the anharmonic part, which describes phonon-phonon scattering processes. We assume that the anharmonic part of the Hamiltonian is small and analyze its effects via many-body perturbation theory.

In the following, we first analyze the cubic part of the Hamiltonian in detail and then outline the analogous steps for the quartic part. The latter part is important to ensure that the Hamiltonian is bounded below so that a perturbation analysis is properly justified.

5.5.1 Cubic Hamiltonian

We first express the cubic part of the Hamiltonian in terms of normal mode operators. Inserting (5.21) into the expressions for the linear and nonlinear contributions

of the strain tensor yields

$$u^{lin}(x,y) = \sum_{J,\kappa} e^{i\ell x/R+iky} u^{lin}_J(\kappa) q_J(\kappa), \tag{5.24}$$

$$u^{nlin}(x,y) = \sum_{J,J'} \sum_{\kappa,\kappa'} e^{i\ell x/R+iky} e^{i\ell' x/R+ik'y} \times \tag{5.25}$$

$$u^{nlin}_{JJ'}(\kappa,\kappa') q_J(\kappa) q_{J'}(\kappa'), \tag{5.26}$$

where we introduced the fused quantum number $\kappa = (k, \ell)$ and we defined

$$q_J(\kappa) = \sqrt{\frac{\hbar}{2M\omega_J(\kappa)}} \left(a_J(\kappa) + a^\dagger_J(-\kappa) \right). \tag{5.27}$$

In (5.24) and (5.26), $u^{lin}_J(\kappa)$ and $u^{nlin}_{JJ'}(\kappa,\kappa')$ are given by

$$u^{lin}_J(\kappa) = \frac{1}{2} \begin{bmatrix} 2(il\epsilon_x + \epsilon_z)/R & il\epsilon_y/R + ik\epsilon_x \\ il\epsilon_y/R + ik\epsilon_x & 2ik\epsilon_y \end{bmatrix}, \tag{5.28}$$

and

$$2u^{nlin}_{xx} = \frac{1}{R^2} \left\{ (il\epsilon_x + \epsilon_z)(il'\epsilon'_x + \epsilon'_z) - ll'\epsilon_y\epsilon'_y + (il\epsilon_z - \epsilon_x)(il'\epsilon'_z - \epsilon'_x) \right\}, \tag{5.29}$$

$$2u^{nlin}_{xy} = \frac{1}{R} \left\{ (il\epsilon_x + \epsilon_z) ik'\epsilon'_x - l\epsilon_y k'\epsilon'_y + (il\epsilon_z - \epsilon_x) ik'\epsilon'_z \right\}, \tag{5.30}$$

$$2u^{nlin}_{yy} = -kk'(\epsilon_x\epsilon'_x + \epsilon_y\epsilon'_y + \epsilon_z\epsilon'_z), \tag{5.31}$$

with $\hat{\epsilon}' \equiv \hat{\epsilon}_{J'}(\kappa')$.

Inserting the above expressions for u^{lin} and u^{nlin} into (5.16), we arrive at the desired expression for the cubic Hamiltonian

$$H_3 = \int dxdy\, \mathcal{H}_3 \tag{5.32}$$

$$= A \sum_{J_1J_2J_3} \sum_{\kappa_1\kappa_2\kappa_3} G_{J_1J_2J_3}(\kappa_1,\kappa_2,\kappa_3) \times \tag{5.33}$$

$$q_{J_1}(\kappa_1) q_{J_2}(\kappa_2) q_{J_3}(\kappa_3) \delta_{\kappa_1+\kappa_2+\kappa_3=0}, \tag{5.34}$$

where the coupling function $G_{J_1J_2J_3}(\kappa_1,\kappa_2,\kappa_3)$ is given by

$$\begin{aligned} G_{J_1J_2J_3}(\kappa_1,\kappa_2,\kappa_3) &= \lambda \mathrm{Tr} u^{nlin}_{J_1J_2}(\kappa_1,\kappa_2)\mathrm{Tr}u^{lin}_{J_3}(\kappa_3) + 2\mu\mathrm{Tr}(u^{lin}_{J_1}u^{nlin}_{J_2J_3}(\kappa_2,\kappa_3)) \\ &+ \zeta_1 \mathrm{Tr}u^{lin}(\kappa_1)\mathrm{Tr}u^{lin}_{J_2}(\kappa_2)\mathrm{Tr}u^{lin}_{J_3}(\kappa_3) \\ &+ \zeta_2 \mathrm{Tr}u^{lin}_{J_1}(\kappa_1)\mathrm{Tr}(u^{lin}_{J_2}(\kappa_2)u^{lin}_{J_3}(\kappa_3)). \end{aligned} \tag{5.35}$$

5.5.2 Quartic Hamiltonian

To express the quartic Hamiltonian in terms of creation and annihilation operators, we insert the expression for u^{lin} and u^{nlin} [Equations (5.24) and (5.26)] into (5.18). Following De Martino *et al.* [10] we only take into account quartic geometric nonlinearities resulting from replacing u_{ij} in (5.11) by its nonlinear part. This part of the quartic Hamiltonian gives the dominant contribution for long-wavelength phonons [10].

5.5.3 Phonon Green's function and quality factor

The Green's function describing the behavior of a phonon of polarization J in a non-interacting system is

$$d_J(\kappa,\kappa',\tau_1,\tau_2) = \frac{1}{\hbar}\langle T_\tau q_{J\kappa}(\tau_1)q_{J\kappa'}(\tau_2)\rangle_0 = \frac{\delta_{\kappa\kappa'}}{\beta\hbar}\sum_{\Omega_n} e^{-i\Omega_n(\tau_1-\tau_2)}\frac{1}{M}\frac{1}{\omega_J^2(\kappa)+\Omega_n^2}, \tag{5.36}$$

where τ_1 and τ_2 denote imaginary times and Ω_n is a Matsubara frequency. When interactions between phonons are introduced, the frequencies of the phonons are renormalized and the phonons acquire a finite linewidth $\Delta\omega$. To compute these quantities, we determine the Green's function in the interacting system by solving Dyson's equation. At lowest order, the irreducible polarization function $P_J(\kappa,\omega)$,

which is the analogue of the electron self-energy in the many-body theory of phonons, can be represented diagrammatically as the sum of a tadpole diagram, which does not contribute to the phonon lifetime, and a bubble diagram due cubic anharmonicities. The lowest order diagrams due to quartic anharmonicities are also included, see Figure 5.5. In principle, we would imagine a self-consistent calculation where all phonon lines in these diagrams are fully renormalized ("dressed") as we ultimately do in the low temperature analysis. At higher temperatures, we find that the effects of the self-consistency on the final result are not significant.

Using the standard Feynman rules of perturbation theory, we can evaluate the phonon polarization function. We first evaluate the contribution from the diagrams originating from the cubic part of the Hamiltonian which at higher temperatures yield the dominant contribution to the intrinsic phonon linewidth. Then, we evaluate the diagrams originated from the quartic anharmonicity which are important mostly for very low temperatures.

The imaginary part of the phonon polarization function due to the diagrams originating from the cubic anharmonicity is given by

$$\begin{aligned} \mathrm{Im}P_J(\kappa,\omega) &= \frac{9\pi}{2}\frac{\hbar}{\rho_M^2}\sum_{J_2J_3}\sum_{\kappa_2}\frac{|G_{JJ_2J_3}(-\kappa,\kappa_2,\kappa-\kappa_2)|^2}{\omega_2\omega_3} \\ &\times \sum_{\xi_2\xi_3=\pm}\xi_2\xi_3\left[n(-\xi_2\omega_2)-n(\xi_3\omega_3)\right]\delta(\omega+\xi_2\omega_2+\xi_3\omega_3), \quad (5.37) \end{aligned}$$

with $\omega_2=\omega_{J_2}(\kappa_2)$ and $\omega_3=\omega_{J_3}(\kappa-\kappa_2)$. Also, $n(\omega)=1/(\exp(\beta\hbar\omega)-1)$ denotes the Bose-Einstein occupation function with $\beta=1/(k_BT)$ being the inverse thermal energy. Finally, the inverse quality factor, which is related to the linewidth via $Q^{-1}=\Delta\omega/\omega$, is given by

$$Q_J^{-1}(\kappa)=-\frac{\mathrm{Im}P_J(\kappa,\omega_J(\kappa))}{M\omega_J^2(\kappa)}. \quad (5.38)$$

Evaluation of (5.37) and (5.38) for the specific case of the fundamental flexural

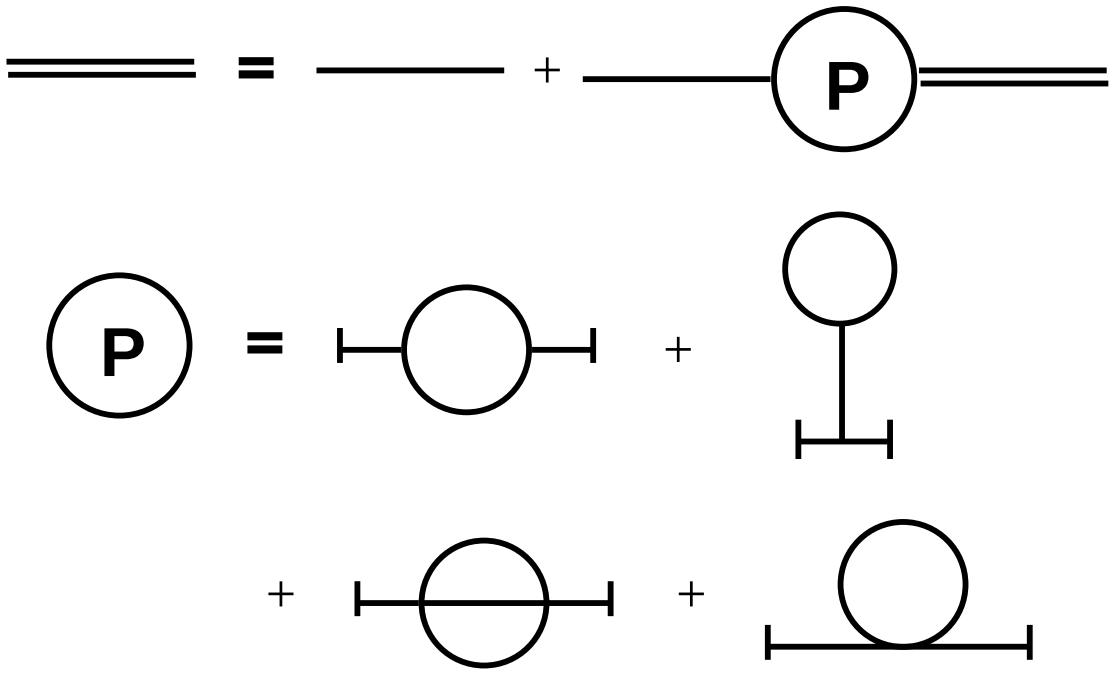

Figure 5.5: Diagrammatic representation of Dyson's equation in the phonon case: solid lines denote bare phonon Green's functions, double solid lines denote dressed Green's functions. The irreducible phonon polarization function P is approximated as the sum of a tadpole and a bubble diagram from cubic anharmonicities and two diagrams from quartic anharmonicities.

mode which is the lowest energy mode of the flexural branch allowed by the boundary conditions is greatly facilitated by the various conservation laws. In addition to energy conservation, translational invariance along the tube axis imposes conservation of k. Rotational invariance around the tube axis imposes conservation of ℓ. These conservation laws forbid the decay of the fundamental flexural mode in a three-phonon process which involves two other low-frequency modes [10]. If, however, the fundamental flexural mode, which has a wavelength comparable to the length of the tube, interacts with a high-energy phonon of momentum k_μ, energy and momentum conservation enforce that the third phonon also has a high energy and momentum $k_\nu \approx k_\mu$. Because the flexural mode carries $\ell = \pm 1$, the angular momenta of the two high-energy phonons must differ by one. In sum, three-phonon decays of the fundamental flexural mode are only possible at crossings of two phonon bands whose angular momentum quantum numbers differ by one. Inspection of Figure 5.6 reveals that very few such crossings for energies comparable and smaller than $k_B T \approx 24$ meV (at room temperature) exist.

Mathematically, we convert the sum over intermediate momenta in (5.37) into an integral. This is allowed, because the energy uncertainty resulting from the short lifetimes [26] of the relevant high energy modes is larger than the energy difference of phonons at neighboring allowed wavevectors of the finite-length tube. Then, we can justify using the energy-conserving δ-function to reduce the integral into a sum over allowed crossings. Our final expression for the inverse quality factor resulting from the decay of a long wavelength flexural mode of wavevector k in a three-phonon process involving two high-energy modes (labeled μ and ν) at a phonon crossing at wavevector $k_\times$ and angular frequency $\omega_\times$ is

$$Q_3^{-1} = \sum_\times g_{F\mu\nu}(k, k_\times, \ell_\mu) \frac{\beta \hbar^2 n(\omega_\times)[n(\omega_\times)+1]}{R \omega_F(k) \omega_\times^2 |v_\mu^\times - v_\nu^\times|}, \tag{5.39}$$

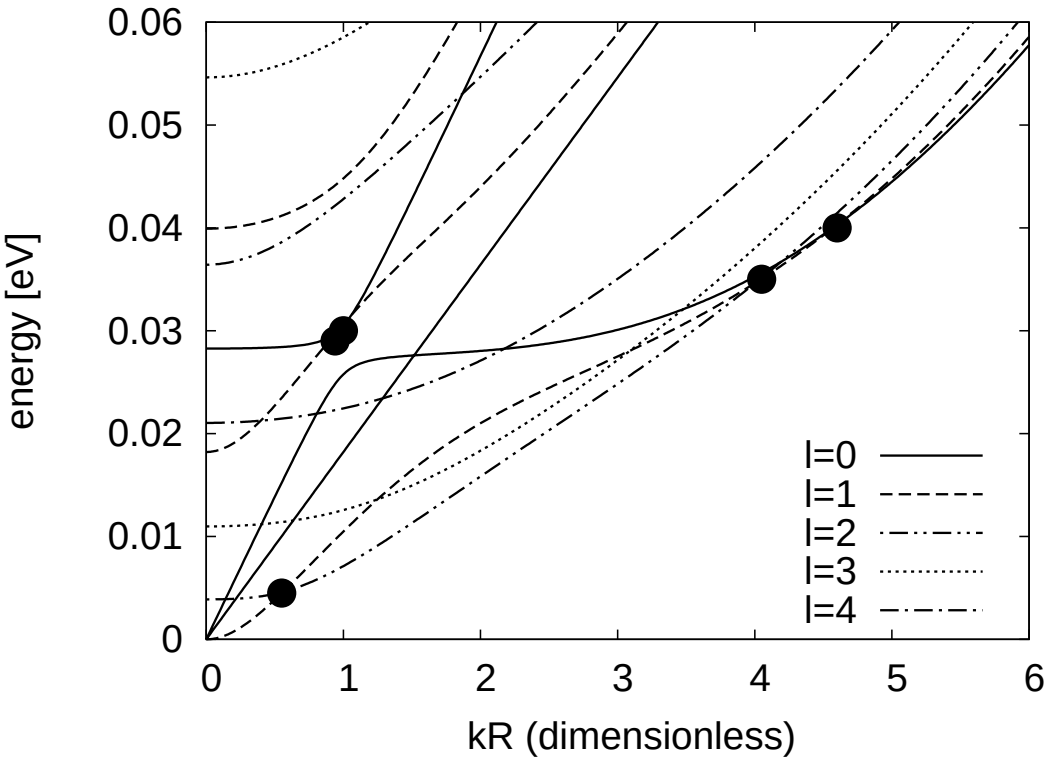

Figure 5.6: Phonon energy versus kR for a $R = 0.5$ nm tube. The black dots denote phonon crossings, where three-phonon decays of the fundamental flexural mode are allowed. The low-energy crossing between the flexural branch and the lowest $\ell = 2$ branch dominates the three-phonon losses at low temperatures.

where $g_{F\mu\nu} = |G_{JJ_\mu J_\nu}(-\kappa, \kappa_\mu, \kappa_\nu)|^2$ is a complicated coupling function that depends on the polarization vectors of all three phonons and gives a complete description of both material and geometric nonlinearities. Also, $\sum_\times$ denotes a sum over allowed crossings and $v^\times_{\mu/\nu}$ are the phonon group velocities.

Computationally, evaluation of (5.39) at each allowed crossing proceeds as follows. For a given radius R of the tube, we first compute the phonon band structure by diagonalizing $\mathcal{H}_2$, (5.15), and then determine $k_\times$ of the crossing numerically by searching for the zero of $\omega_{J_2}(k) - \omega_{J_3}(k)$ via a bisection algorithm. This also immediately gives $\omega_\times$, the unit polarization vectors and the phonon group velocities. Finally, we evaluate the coupling function $g_{F\mu\nu}$ and compute the contribution to the total inverse quality factor from the specific crossing under consideration.

To estimate the role of four-phonon processes, we compute the leading order contribution, the fishbone diagram, due to a quartic coupling between four low-energy flexural modes. Following De Martino *et al.* [10] and our findings for the three-phonon case, we only take into account quartic geometric nonlinearities resulting from replacing u_{ij} in (5.11) by its nonlinear part. The resulting expression for the four-phonon contribution to the quality factor contains a triple sum over intermediate phonon momenta and is given by [27]

$$\begin{aligned} Q_4^{-1} &= \sum_{q_1 q_2 q_3} \sum_{\xi_1,\xi_2,\xi_3=\pm} \frac{\xi_1\xi_2\xi_3 \mathcal{D}(q_1, q_2, q_3, k)\eta/\pi}{(\omega_F(k) + \xi_1\omega_1 + \xi_2\omega_2 + \xi_2\omega_3)^2 + \eta^2} \\ &\quad \times \frac{n(\xi_1\omega_1)n(\xi_2\omega_2)n(\xi_3\omega_3)}{n(\xi_1\omega_1 + \xi_2\omega_2 + \xi_3\omega_3)}, \end{aligned} \tag{5.40}$$

where q_i denote intermediate momenta, $\omega_i \equiv \omega_F(q_i)$ and $\mathcal{D}$ denotes the coupling function. Here, η is the inverse lifetime associated with the dressed phonon lines representing the actual phonons in the system with loss.

In evaluating (5.40), proper account of the finite length of the tube, which leads

to a finite spacing of the allowed wavevectors, is of crucial importance. For long wavelength flexural phonons in tubes of experimental lengths, the energy uncertainty ΔE_η associated with the observed lifetimes is actually much smaller than the energy difference $\Delta E_{\Delta k}$ of phonons at neighboring wavevectors: Expressing η in terms of the quality factor, $\eta = \omega_F/(2\pi Q)$, we find $\Delta E_\eta/\Delta E_{\Delta k} = 1/(4\pi Q)$, which is much smaller than unity at low temperatures [3]. Thus, the sums over intermediate momenta *cannot* be converted into integrals for the tubes in the experiments. Converting the sums into integrals, as De Martino *et al.*[10] do, is appropriate for much longer tubes, but leads to an underestimate of Q_4 due to inclusion of processes which are not present in the experiments, namely scattering into modes of wavelength longer than the actual tube.

We note that this issue did not arise in the three-phonon case because, there, momentum and energy conservation only allowed scattering with higher energy modes, which had much shorter lifetimes. At the low temperatures we consider here such higher modes are exponentially suppressed, and the remaining fourth-order processes only involve the long-wavelength acoustic modes, which, as discussed above, have very long lifetimes.

To describe four-phonon decays in experimentally relevant nanotubes, we carry out numerically the discrete triple sum over intermediate momenta in (5.40) using the discrete frequencies of a finite-length doubly clamped beam and experimentally observed inverse lifetimes η. The result then gives the *contribution* to the observed losses from four-phonon processes.

5.6 Nanotubes under strain

Experiments with doubly clamped tubes inevitably involve some amount of strain. Here we consider the case of positive strain, corresponding to some amount of tension in the tube. To study the quality factor of such a strained tube, we expand the displacement around the new equilibrium value, taking into account the relaxation in the equilibrium radius. Evaluation of (5.12) at the strained equilibrium configuration leads to two categories of additional contributions to the *quadratic* Hamiltonian: one set of terms is already present in $\mathcal{U}_2$ and can be absorbed into a redefinition of the linear elastic constants; the other set of terms gives the expected Hamiltonian for a string under tension, proportional to $(\partial_y u_x)^2 + (\partial_y u_z)^2$ with a prefactor proportional to the tension.

5.7 Results

Figure 5.7 shows our results for the three-phonon contribution to the inverse quality factors for tubes of typical experimental radii as a function of inverse temperature. At low temperatures [right side of Figure 5.7(a)], Q_3^{-1} approaches zero exponentially, because the first Bose-Einstein factor in (5.39) rapidly diminishes the occupation of the high-energy modes at the crossings, which are the modes responsible for the scattering. At higher temperatures, $T > 100$ K, the modes associated with the relevant crossings are classically occupied and we find that Q_3^{-1} is proportional to temperature. Here we define the temperature of the nanotube as the temperature of the thermal bath which is in contact with the tube.

Comparing the inverse quality factors of tubes of different radii in Figure 5.7,

we find that at low temperatures the tube with the smallest radius, $R = 0.3$ nm, exhibits the lowest dissipation, while at high temperatures its losses are largest [see Figure 5.7(b)].

To understand this nontrivial radius dependence of Q_3, we note that for $T <$ 40 K the largest contribution to the losses comes from the crossing which is lowest in energy. The energy of this crossing of the flexural mode and the lowest optical mode is approximately equal to the gap of the optical mode given by $E_{gap} = \sqrt{k_c/(5\rho_M)}6\hbar/R^2$, which depends sensitively on the radius of the tube. Therefore, at low temperatures, the occupation of the high-energy modes at this crossing is much more strongly suppressed for tubes with smaller radii (and therefore higher optical frequency), which leads to smaller losses according to (5.39). At higher temperatures, the contributions from other crossings become important (see Figure 5.6). We find that those contributions depend quite sensitively on R with a variety of scalings, which ultimately lead to the observed crossover behavior of the $R = 0.3$ nm tube.

Figure 5.8(a) shows the dependence of Q_3 on the length L of the nanotube. In a tensionless tube (solid line), we find a remarkable cancellation between the length dependence of the coupling function, $g_{F\mu\nu} \propto k^2$ for small k, and the length dependence of $\omega_F \propto k^2$ in (5.39), resulting in a quality factor which is insensitive to tube length beyond ~ 300 nm. Strained tubes do not exhibit this cancellation because $\omega_F(k)$ is shifted by a constant proportional to the tension τ if the tension is small (dashed line)[28]. If τ is large, $\omega_F(k) \propto \sqrt{\tau}k$ and Q_3 becomes linear in L for long tubes (dotted line)[28].

For tubes shorter than 300 nm, Figure 5.8(a) shows a significant length dependence of Q_3 even for tensionless tubes. In particular, in tubes with lengths of only

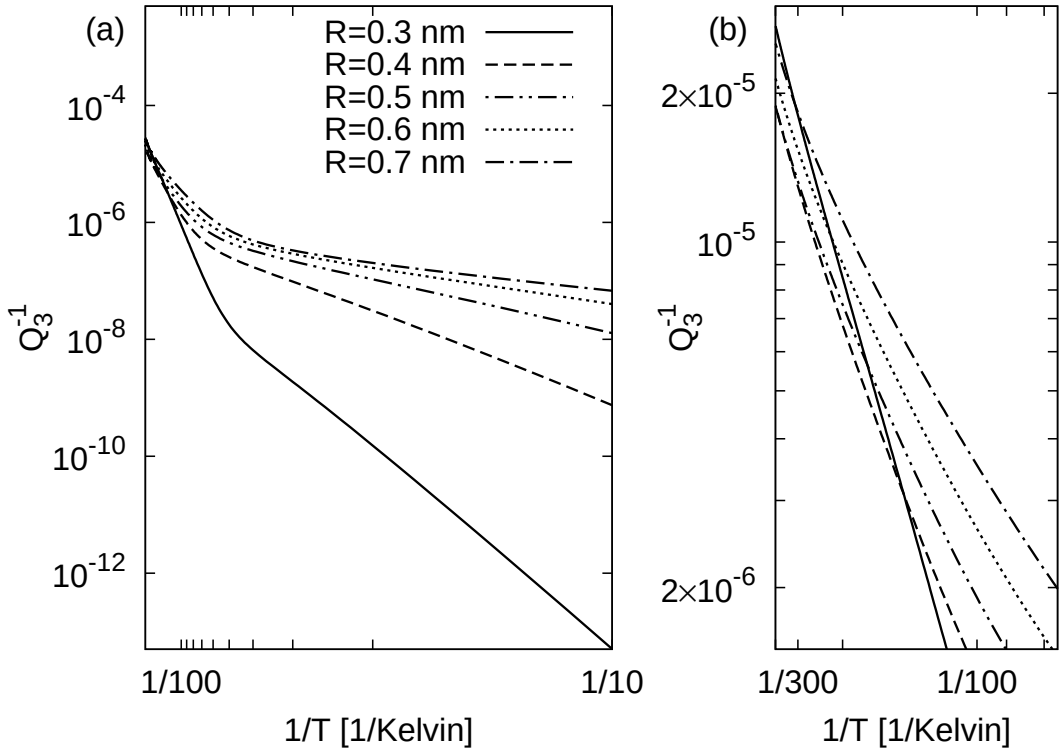

Figure 5.7: Log-log plots of temperature dependence of Q_3 for tubes of different radii and length $L = 500$ nm.

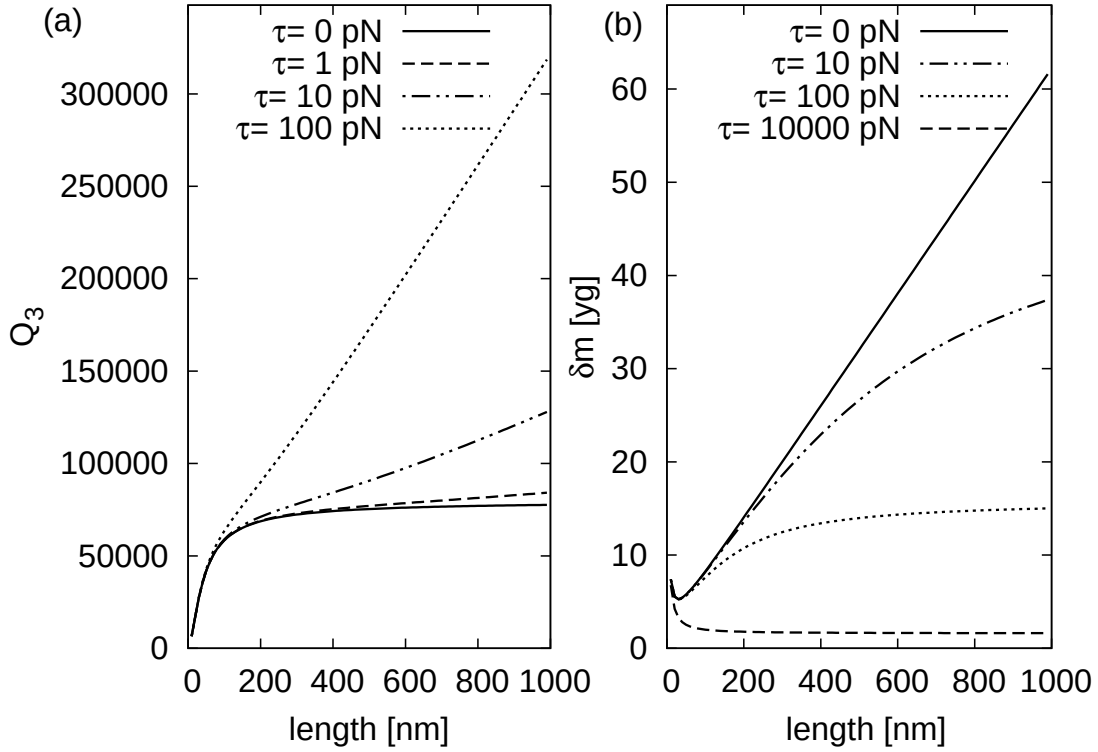

Figure 5.8: (a) Length dependence of Q_3 for tubes with $R = 0.5$ nm at $T = 300$ K. (b) Length dependence of mass resolution δm for tubes with $R = 0.5$ nm at $T = 300$ K.

a few nanometers Q_3 is reduced by more than an order of magnitude. This may be related to the small quality factors, $Q \approx 1500$, found by Jiang *et al.* [8], who model the decay of the fundamental flexural mode in a 3 nm long singly clamped tube via molecular dynamics simulations.

Next, we compare the magnitude of the computed intrinsic quality factor to experimental findings. At $T = 300$ K, we find for the intrinsic quality factor, $Q_3 \approx 5 \times 10^4$. Experiments, on the other hands, typically find $Q_{exp} \lesssim 2000$[4, 7] indicating that extrinsic sources, most likely associated with the clamping contacts, dominate the losses in current experiments.

We find that the resulting (intrinsic) mass resolution, $\delta m = 2M/Q$, of a *tensionless* nanotube mass sensor depends sensitively on the tube length L with a minimum of ~ 5 yg for very short tubes [Figure 5.8(b)]. On the other hand, (i) we find that application of tension can reduce the mass resolution δm to a *single yoctogram* if a tension close to the elastic limit, $\tau_c \approx 100$ nN [29], is applied, and (ii) we find that δm becomes independent of L for long tubes, simplifying the design and fabrication of actual devices.

5.8 Four-phonon processes

At lower temperatures, as discussed above, three-phonon processes are exponentially suppressed due to the energy gap of the optical modes, and the resulting dissipation becomes much smaller than the experimental findings in the milikelvin range [3]. We, therefore, now move on to consider losses from four-phonon decays.

We evaluate (5.40) and find that the *contributions* to the quality factor from

four-phonon processes are $Q_4 = 6.6 \times 10^8$ at $T = 1$ K and $Q_4 = 1.6 \times 10^{14}$ at $T = 0.01$ K for a tube of length $L = 800$ nm and $R = 1.5$ nm [3]. This indicates that, at low temperatures, four-phonon decays give only a small contribution to the observed losses, which are $Q \approx 10^4$ at $T = 1$ K and $Q \approx 10^5$ at $T = 0.01$ K [3]. Although small, these losses are still much greater than the three-phonon contributions: $Q_3 = 3.1 \times 10^{27}$ at 1 K and even greater at 0.01 K. Our analysis suggests that, contrary to other theoretical approaches, the losses observed by Hüttel *et al.*[3] are mostly extrinsic.

5.9 Linewidth of the radial breathing mode

In this section, we describe briefly the calculation of the linewidth of the radial breathing mode due to phonon-phonon interactions and analyze the contributions from the various decay channels.

The radial breathing mode plays an important role in the characterization of carbon nanotubes because its frequency is inversely proportional to the radius of the tube. Its linewidth was measured by several groups [30, 31] using Raman spectroscopy. Another experiment[32] employed scanning tunnelling microscopy and found lifetimes several orders of magnitude larger than those obtained in the Raman scattering experiments. The apparent discrepancy was subsequently explained by the theoretical demonstration that non-equilibrium phonon occupations, which are expected to occur in low-dimensional systems, can lead to slowly decaying tails of the breathing mode phonon population [30, 33]. These tails cannot be observed in Raman scattering experiments, but are accessible in the scanning tunnelling experiments. However, these calculations assumed without justification that the

breathing mode primarily decays into acoustic phonons and also employed phenomenological values for the scattering matrix elements [30, 33].

In the following, we analyze the contribution to the linewidth from all allowed decay channels using *ab initio* matrix elements and find that the breathing mode prefers to decay into a particular low-lying *optical* mode. We neglect the difficulties associated with non-equilibrium occupations. Our results for the phonon linewidth should then be comparable to experimental findings in Raman scattering experiments.

For the specific case of the radial breathing mode, which is an optical mode with $\ell = 0$ and $k = 0$, the linewidth $\Delta\omega_{RBM}$ is given by

$$\Delta\omega_{RBM} = \frac{9\pi}{2}\frac{\hbar A^2}{M^3\omega_{RBM}}\sum_{J_2J_3}\sum_{k_2\ell_2}\frac{|G_{J_2J_3}(0,0|k_2,\ell_2|-k_2,-\ell_2)|^2}{\omega_2\omega_3}\times$$
$$\{(n_2+n_3+1)\delta(\omega_{RBM}-\omega_2-\omega_3)+2(n_2-n_3)\delta(\omega_{RBM}+\omega_2-\omega_3)\}, \quad (5.41)$$

with $\omega_2 = \omega_{J_2}(k_2,\ell_2)$ and $\omega_3 = \omega_{J_3}(-k_2,-\ell_2)$ and $n_{2/3}$ are defined analogously.

To compute $\Delta\omega_{RBM}$ we evaluate all possible decay channels allowed by the various conservation laws. Figure 5.9 shows our results for the linewidth of the breathing mode at room temperature and experimental data from Rao *et al.* obtained in Raman scattering experiments [30]. We observe that the computed $\Delta\omega_{RBM}$ *diverges* at $R \approx 0.39$ nm.

To understand the origin of this divergence, we analyze the contributions to the total linewidth from the various allowed decay channels. We find that the dominant contribution comes from the first term in curly brackets in (5.41), which describes processes where the breathing mode phonon decays into two lower energy phonons. In particular, we find that for tubes with radius larger than ~ 0.39 nm over 90 percent of the total linewidth is contributed by the decay of the breathing

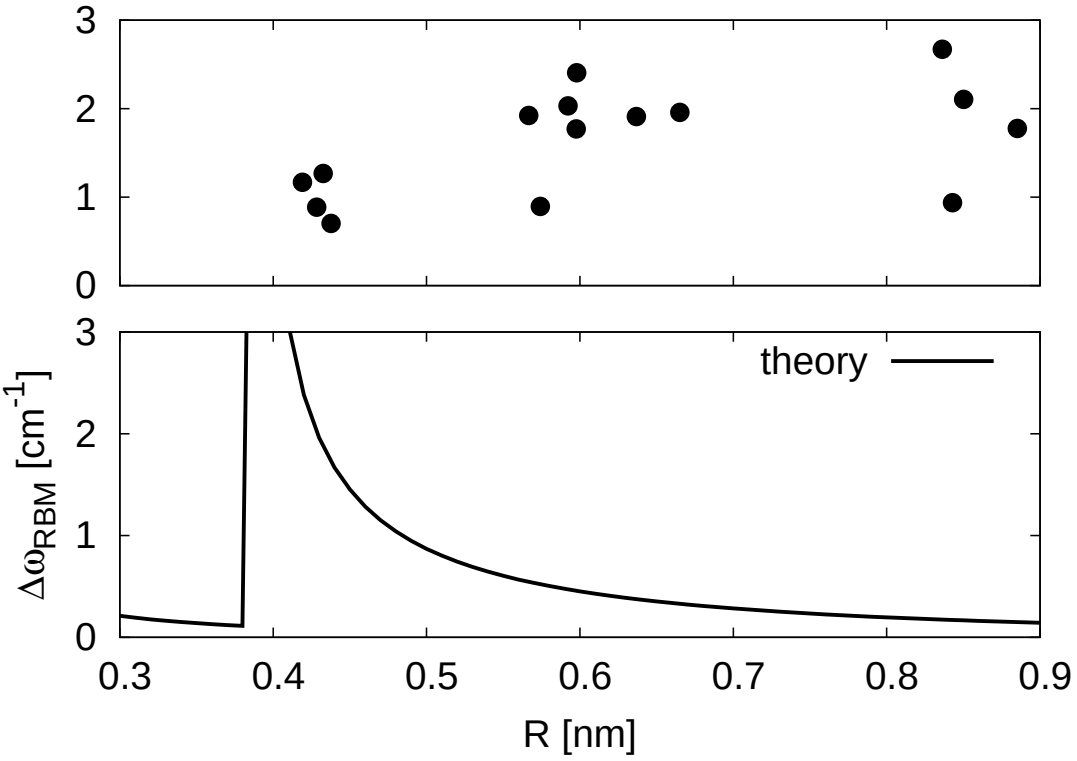

Figure 5.9: Radius dependence of the linewidth of the radial breathing mode at room temperature. The black dots in the upper panel denote experimental data obtained by Rao *et al.* using Raman spectroscopy [30]. The curve in the lower panel shows the computed intrinsic linewidth due to phonon-phonon interactions.

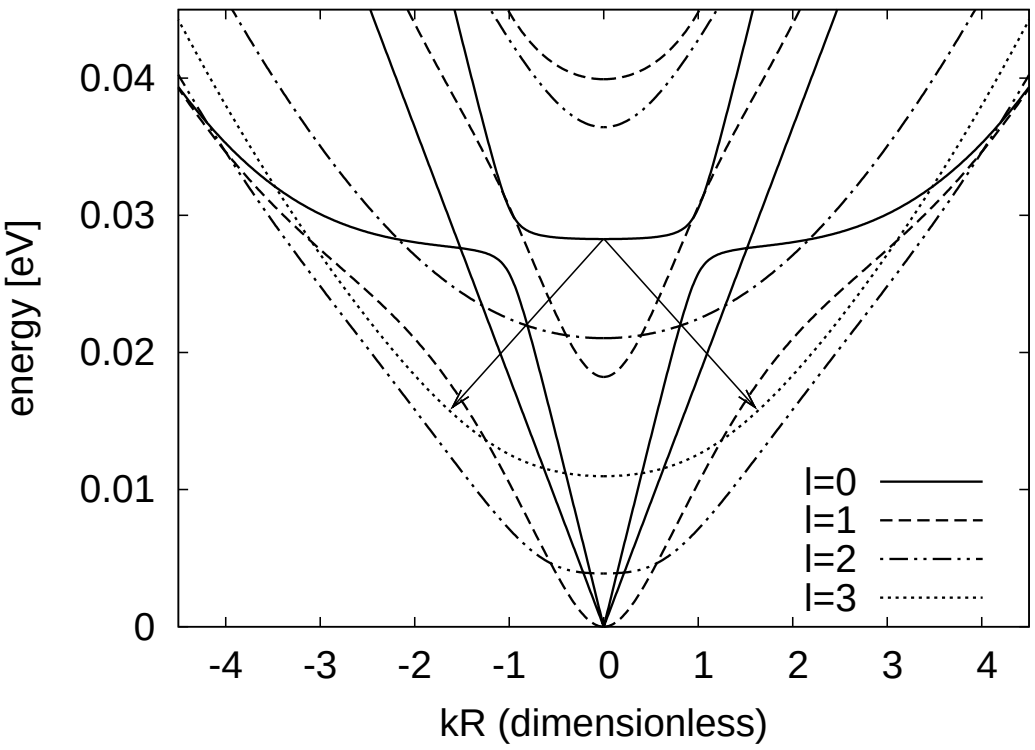

Figure 5.10: Arrows indicate the dominant (for tubes with $R > 0.39$ nm) decay channel of the radial breathing mode into two $\ell = 3$ phonons.

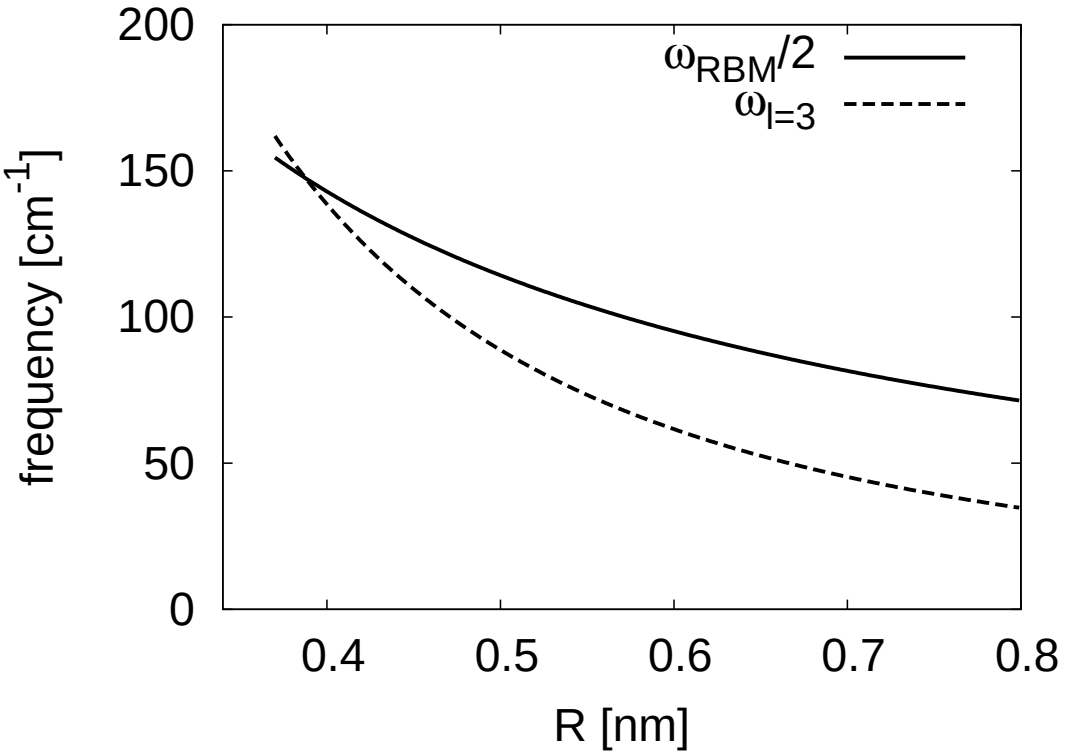

Figure 5.11: Radius dependence of the the breathing mode frequency and the frequency of the $\ell = 3$ mode. For radii smaller than $R \approx 0.39$ nm energy conservation forbids the decay of the breathing mode into two $\ell = 3$ phonons.

mode phonon into two $\ell = 3$ phonons. This process is shown in Figure 5.10.

As we approach from above the "critical" radius, where $\Delta\omega_{RBM}$ diverges, we observe that the difference of the breathing mode frequency and the frequency of the $\ell = 3$ mode becomes smaller (see Figure 5.11), such that eventually, at the "critical" radius, energy conservation forbids this particular decay channel. To conserve energy, the secondary $\ell = 3$ phonons end up closer and closer to the center of the Brillouin zone, as we approach the "critical radius" from above, and their group velocities, which are the slopes of the $\ell = 3$ phonon branch at $\omega_{RBM}/2$, approach zero. Converting the sum over k_2 in (5.41) into an integral, it is straightforward to show that $\Delta\omega_{RBM}$ is inversely proportional to the group velocity of the secondary phonons, which explains the observed divergence at $R \approx 0.39$ nm.

Comparing our results for $\Delta\omega_{RBM}$ with experimental data [30] in Figure 5.9, we find that the overall order of magnitude of the computed linewidth agrees with the experimental findings. In contrast, the details of the computed radius dependence and, in particular, the divergence of $\Delta\omega_{RBM}$ at $R \approx 0.39$ nm are not found in the experimental data. However, the significant scatter in the experimental data indicates that either another loss mechanism exists, which contributes to the linewidth and depends on the wrapping index of the nanotube, or that due to technical difficulties there are errors in the experimental data.

Also, we should note that the critical $\ell = 3$ branch begins to have a wavelength comparable to the interatomic spacing for such small tubes and so our determination of the "critical radius" for this process within a continuum theory suffers from errors as well. We hope that future experiments explore the linewidth of the radial breathing mode further and that future calculations with interatomic potentials or electronic density-functional theory study this loss channel, so that

the aforementioned issues can be clarified.

5.10 Summary and conclusions

We have examined phonon-phonon interactions in carbon nanotubes using an elastic continuum theory with harmonic and anharmonic elastic constants obtained from *ab initio* calculations. The resulting theory captures both acoustic and low-lying optical phonon dispersions and allows us to predict intrinsic quality factors of the fundamental flexural mode for tubes of different lengths and radii, but also for different temperatures and strains. We find that the intrinsic quality factor at room temperature is about one order of magnitude higher than current experimental findings, indicating that there remains room for improvement in current devices. We also explore the possibility of carbon nanotube mass sensors with single yoctogram precision.

BIBLIOGRAPHY

[1] B. Lassagne, Y. Tarakanov, J. Kinaret, D. Garcia-Sanchez, and A. Bachtold. *Science*, 325:1107, 2009. 95

[2] G.A. Steele, A.K. Huettel, B. Witkamp, M. Poot, H.B. Meerwaldt, L.P. Kouwenhoven, and H.S.J. van der Zant. *Science*, 325:1103, 2009.

[3] A. Huettel, G.A. Steele, B. Witkamp, M. Poot, L.P. Kouwenhoven, and H.S.J. van der Zant. *Nano Lett.*, 9(7):2547, 2009. 96, 118, 123, 124

[4] K. Jensen, K. Kim, and A. Zettl. *Nat. Nanotechnol.*, 3:533, 2008. 95, 96, 123

[5] B. Lassagne, D. Garcia-Sanchez, A. Aguasca, and A. Bachtold. *Nano Lett.*, 8 (11):3735, 2008. 95, 96

[6] H.-Y. Chiu, P. Hung, H.W.C. Postma, and M. Bockrath. *Nano Lett.*, 8(12): 4342, 2008. 95

[7] B. Witkamp, M. Poot, and H.S.J. van der Zant. *Nano Lett.*, 6(12):2904, 2006. 96, 123

[8] H. Jiang, M.-F. Yu, B. Liu, and Y. Huang. *Phys. Rev. Lett.*, 93(18):185501, 2004. 96, 123

[9] S. P. Hepplestone and G. P. Srivastava. *Phys. Rev. B*, 74(16):165420, 2006. 96

[10] A. De Martino, R. Egger, and A. O. Gogolin. *Phys. Rev. B*, 79:205408, 2009. 96, 97, 101, 112, 115, 117, 118

[11] X. Wei, Q. Chen, S. Xu, L. Peng, and J. Zuo. *Adv. Funct. Mater.*, 19:1753, 2009. 96

[12] H. Suzuura and T. Ando. *Phys. Rev. B*, 65:235412, 2002. 97, 100

[13] J. C. Bowman and J. A. Krumhansl. *J. Phys. Chem. Solids*, 6:367, 1958. 97

[14] J. A. Krumhansl and H. Brooks. *J. Chem. Phys.*, 21:1663, 1953. 97

[15] W. Kohn and L.J. Sham. *Phys. Rev.*, 140:A1133, 1965. 101

[16] P. Hohenberg and W. Kohn. *Phys. Rev.*, 136:B864, 1964. 101

[17] H.J. Monkhorst and J.D. Pack. *Phys. Rev. B*, 13:5188, 1976. 101

[18] L. Kleinman and D.M. Bylander. *Phys. Rev. Lett.*, 48:1425, 1982. 101

[19] P. T. Araujo, I. O. Maciel, P. B. C. Pesce, M. A. Pimenta, S.K. Doorn, H. Qian, A. Hartschuh, M. Steiner, L. Grigorian, K. Hata, and A. Jorio. *Phys. Stat. B*, 77:241403 (R), 2008. 104

[20] O.L. Blakslee, D.G. Proctor, E.J. Seldin, G.B. Spence, and T.Weng. *J. Appl. Phys.*, 41:3373, 1970. 104

[21] E.J. Seldin and C.W. Nezbeda. *J. Appl. Phys.*, 41:3389, 1970. 104

[22] K. N. Kudin, G. E. Scuseria, and B. I. Yakobson. *Phys. Rev. B*, 64:235406, 2001. 107

[23] D. Sánchez-Portal, E. Artacho, J. M. Soler, A. Rubio, and P. Ordejón. *Phys. Rev. B*, 59:12678, 1999. 107, 108

[24] K. V. Zakharchenko, M. I. Katsnelson, and A. Fasolino. *Phys. Rev. Lett.*, 102 (4):046808, 2009. 107

[25] T. Yamamoto, S. Watanabe, and K. Watanabe. *Phys. Rev. Lett.*, 92(7): 075502, 2004. 108

[26] D. Song, F. Wang, G. Dukovic, M. Zheng, E.D. Semke, L.E. Brus, and T.F. Heinz. *Phys. Rev. Lett.*, 100:225503, 2008. 115

[27] B. Perrin. *Phys. Rev. B*, 36:4706, 1987. 117

[28] S. Sapmaz, Y.M. Blanter, L. Gurevich, and H.S.J. van der Zant. *Phys. Rev. B*, 67:235414, 2003. 120

[29] P. Zhang, P.E. Lammert, and V.H. Crespi. *Phys. Rev. Lett.*, 81:5346, 1998. 123

[30] R. Rao, J. Menendez, C. D. Poweleit, and A. M. Rao. *Phys. Rev. Lett.*, 99: 047403, 2007. 124, 125, 126, 129

[31] Y.-S. Lim, K.-J. Yee, J.-H. Kim, E. H. Haroz, J. Shaver, J. Kono, S. K. Doom, R. H. Hauge, and R. E. Smalley. *Nano Lett.*, 6:2696, 2006. 124

[32] B. J. LeRoy, S. G. Lemay, J. Kong, and C. Dekker. *Nature*, 432:371, 2004. 124

[33] N. Bonini, R. Rao, A. M. Rao, N. Marzari, and J. Menendez. *Phys. Stat. Sol. (b)*, 245:2149, 2008. 124, 125

CHAPTER 6

OUTLOOK

In this final chapter, we summarize the work of the preceding chapters and discuss future directions.

The first chapter introduced a novel classical density-functional theory of molecular liquids. Starting from an exact free energy functional for the noninteracting molecular gas, we added terms which capture interactions between the molecules. Using the Ornstein-Zernike equation for the uniform liquid, we were able to identify important contributions to the free energy. For the remainder, which was denoted F^{ex}, we employed a relatively simple approximation using a weighted density-functional theory ansatz.

To our knowledge, this is the first work on a polar molecular fluid to include an exact analytic treatment of the non-interacting gas employing simple density fields for each atomic component. The work also introduced a new method to include exactly the leading order of long-wavelength correlations in the bulk fluid, which we showed to be characterized entirely by the static dielectric constant of the fluid.

Clearly, the excess part of the functional, F^{ex}, requires more work. A very promising approach, which was applied with great success to hard sphere liquids [1], is fundamental measure theory, which uses *several* simple weighting functions and reproduces nearly exactly results for the hard sphere fluid. Alternately, the ideas of the weighted-density approximation to the classical density-functional theory of liquids [2] could be pursued. Improvements to the excess part of the functional represent the primary area we foresee for future development of this work.

In the second chapter, we applied the theoretical framework developed in the first chapter to liquid water. We studied the behavior of water near solid interfaces and in applied fields and found results which agreed favorably with classical molecular dynamics simulations. Again, we anticipate that improvements to the framework can still be made by further improvements to the excess part of the functional. In terms of potential applications for this work, our ultimate goal is to couple this theory of water to an *ab initio* description of a solute, such as a dissolved biomolecule. There exists, of course, a huge range of interesting systems which can be explored with this approach, such as solvated proteins, molecular motors, corrosion phenomena and catalytic reactions in fuel cells.

In the third chapter, we introduced a novel joint time-dependent density-functional theory for the description of excited states of solvated molecules. We used this theory to compute the solvato-chromic shifts of the lowest excitations of a formaldehyde molecule in an aqueous environment and found good agreement with experimental observations which was, in fact, better than what was found by other groups using state-of-the-art methods. The primary area we see for improvement here is to improve upon the time-dependent coupling functional. Even in its current form, the theory is useful and appears to be accurate. We envision applying it, even in its current form, to systems of technological relevance, such as dyes in Graetzel cells or chromophores in biological cells.

Finally, in the fourth chapter, we investigated phonon lifetimes in carbon nanotubes. In particular, we examined the role of phonon-phonon interactions and computed the intrinsic quality factor of the fundamental flexural mode and the linewidth of the radial breathing mode. To our knowledge, these are the first such calculations of losses in carbon nanotubes to properly include the quantiza-

tion of the phonons (important because of the relatively high Debye temperature for graphene), realistic tube lengths and to consider elevated temperatures where third-order processes are important. For the flexural mode we find that the experimental losses are dominated by extrinsic sources, most likely associated with the clamping contacts. We believe we are also the first to consider the radial breathing mode. Here, we find order of magnitude agreement between the computed intrinsic linewidths and experimental findings. However, the predicted divergence in the radius dependence is not observable in the experimental data. Future work should explore the radius dependence using an *ab initio* approach and verify that elastic continuum theory is indeed applicable to nanotubes with radii smaller than 0.4 nm. Such *ab initio* calculations become feasible because the computational effort now can be focussed on the key, loss-determining phonon-phonon processes which we have identified. Finally, there remains much that can be studied with the present continuum description. Future work with this model could explore such issues as thermal conductivity of carbon nanotubes as well as nanomechanical modelling of the behavior of graphene sheets.

In conclusion, we have seen that, when constructed with care, microscopically informed continuum models indeed can be applied to a surprisingly wide range of problems in condensed matter physics, from the behavior of polar molecular fluids such as water, to excited electronic states in solvated systems, to losses in carbon nanotube resonators. A final, intriguing possibility, would be to develop a reliable continuum method to accurately describe environmental effects on high-level quantum-chemistry calculations.

BIBLIOGRAPHY

[1] Y. Rosenfeld. *Phys. Rev. Lett.*, 63:980, 1989. 134

[2] W.A. Curtin and N.W. Ashcroft. *Phys. Rev. A*, 32:2909, 1985. 134